# Spatio-temporal development of a joint network and its properties: a case study from Lilstock, UK

---

Master thesis in Structural Geology

**Fredrik August Wyller**


Department of Earth Science

University of Bergen

June 2019

# Abstract

The aim of this study is to investigate the spatial distribution and scaling properties of various joint sets, with particular focus on the temporal development of network properties and the influence of pre-existing structures. This is mainly done through analysis of UAV imagery of a limestone bed surface exposed in the hanging wall of a normal fault on wave-cut platforms along the Somerset Coast, UK.

Networks of bed-bound joints are known to develop extensively in layered sequences during exhumation. Joint formation can be controlled by remote stresses, local stresses and structural inheritance, but there is a lack of understanding about how these factors influence joint geometries and spatio-temporal development of network architecture. This study assesses orientation, length scaling and topological properties of joint traces in order to identify 11 joint sets. The relative chronology of these joint sets is inferred from abutting relationships, allowing for an analysis of the development of geometrical and topological network properties.

The studied network contains a set of fan-like curving joints, which pre-date all other joint sets. The curvature of these joints is interpreted to result from localized stress perturbations along the fault plane, attributed to intersecting faults in the footwall. Joint propagation is affected by structural inheritance, with joints preferentially reactivating older suitably oriented veins. Different joint sets exhibit different length scaling properties. Old joint sets tend to follow power-law length scaling distributions, whereas young sets tend to be described by log-normal or negative exponential scaling laws. Joint geometries and distribution of network properties is controlled by the spatial arrangement of earlier veins and joints. In particular, the fan-structure of curving joints controls spatial distribution of subsequent joint formation. Near isotropic horizontal tension is responsible for curving joints during later stages of network evolution, resulting in block break-up patterns controlled by stress perturbations around pre-existing joints. The topological analysis indicates that the network evolves from consisting predominantly of isolated I-nodes and becomes progressively interconnected with each new joint set due to the formation of abutting Y-nodes. Formation of crossing X-nodes is mainly associated with early joints that reactivate veins, causing different topological pathways for different areas of the fracture network.

The findings from this study contribute to the understanding of how joint networks development in exhumed basins and elucidate how older structures control joint formation and may cause strong heterogeneities in joint network properties.

# Acknowledgements

The road towards submitting a master's thesis is paved with both challenges and excitements. When I stand on the finishing line, there is a list of helpers who have earned my deepest gratitude.

Firstly, I would like to thank my main supervisor Casey Nixon (UiB), whose help has been indispensable. Thanks for fruitful discussions, valuable support and great patience. I will also express my gratitude to David Peacock (UiB) for the UAV imagery he collected during his 2017 field campaign, and for his feedback of geological and philosophical character. I will also thank Atle Rotevatn (UiB) personally, for valuable feedback and words of comfort. David Sanderson (University of Southampton) has kindly supervised me during two visits to Bergen.

I owe a big thanks to Björn Nyberg, whose door I have knocked whenever I have encountered problems in ArcGIS or with NetworkGT (which has happened rather frequently). Kristian Agasøster Haaga and Tor Einar Møller both deserve my gratitude for supporting my feeble attempts to code in Python. Hans J. Skaug and John Wyller have kindly helped me with statistics and probability calculations. Leo Zijervelds name should also be mentioned, for his patience whenever I have suffered from software breakdowns. Izzy Edmundson has given me valuable tips before my field session, and kindly let me use her pictures. I would also like to thank my fellow students Erlend Gjøsund and Erlend Risnes for good discussion about deformational structures in the study area.

In addition, I want to thank my fellow graduate students, with who I have developed a deeper bond during the last days, not to mention the last nights at the university. Five years, multiple field excursions and countless days and nights in the Natural Science Building have resulted in priceless experiences and life-long friendships.

My family is thanked for their words of encouragement and support, and for whole-hearted attempts to read, understand and comment my drafts. Finally, I would like to direct a whole-hearted thanks to my life companion Hanna Brække, who has been carrying me through every step of this journey.

Fredrik August Wyller

Bergen, June 2nd, 2019

# Table of content

# 1. Introduction

## 1.1 Rationale and background

Joint networks are known to form extensively in later stages of basin evolution, and the development of joint networks has been studied in outcrops (Gillespie *et al.*, 1993; Watkins *et al.*, 2015), through analogue experiments (Rives *et al.*, 1994; Wu & Pollard, 1995; de Jossineau, 2003) and numerical modelling (Bourne *et al.*, 2001; Bai *et al.*, 2002; Welch *et al.*, 2015). There is a general agreement that several factors control joint formation in layered sequences, e.g. remote stress (Wheeler & Dixon, 1980; Whitaker & Engelder, 2005; Ghosh & Mitra, 2009), stress perturbations around faults (Rawnsley *et al.*, 1992, Kattenhorn *et al.*, 2000; Bourne & Willemse, 2001), folding (Ramsay, 1962; DeGraff & Aydin, 1987; Fischer & Wilkerson, 2000), lithology (Davy *et al.*, 2013; Rustichelli *et al.*, 2013), bed thickness (Ladeira & Price, 1981; Wu & Pollard, 1995; Bai & Pollard, 2000), fluid pressure (Secor *et al.*, 1965; Engelder & Ortel, 1985; Cosgrove, 2001) and structural inheritance (Cortés *et al.*, 2003; Peacock & Mann, 2005). These factors account for spatial variability in network properties like joint intensity and connectivity (Procter & Sanderson, 2018). There is, however, a lack of literature quantifying such spatial variability and there is a need to improve our understanding of how heterogeneities in joint network properties develop and are controlled.

The most important network properties which will be discussed in this study, are intensity and connectivity. Connectivity will largely be quantified using topological measures, which has been awarded great attention from the scientific community in later years. Manzocchi (2002), Sanderson & Nixon (2015), Morley & Nixon (2016), Peacock *et al.* (2016) and Sanderson *et al*. (2018) do all recognize the advantages of topology in fracture network characterization. This study implements the topological methodology to quantify network properties, speculates how the topological properties have evolved, and discusses the implications for network connectivity.

An increased understanding of the development of joint networks, as well as the spatio-temporal evolution of network properties, has several applications. The presence of fractures controls strength and stability of a rock mass and must be considered when planning infrastructure like roads or tunnels (Barton *et al.*, 1985; Palmström & Singh, 2001). Furthermore, the presence of fractures has great implications for the fluid-flow properties of a rock; they can either act as conduits or baffles to fluid flow and increase the surface area for fluid-rock interactions

(Berkowitz, 2002; Leckenby *et al.*, 2005). In particular, the open-mode and tensile nature of joints can provide a permeability that is several orders of magnitude larger than that of the surrounding rock (Taylor *et al.*, 1999; Mourzenko *et al.*, 1999). Fluid flow through fractures may result in mineral precipitation, and fracture planes may consequently host ore mineral veins (Bons *et al.*, 2012). Finally, fracture networks give indications about past and/or present stress conditions, and fracture network analysis is key in the reconstruction of the geological history of any area (Dyer, 1988; Olsson & Pollard, 1989).

As joints are sub-seismic structures, our understanding of joint distribution relies heavily on insights from outcrop (Sanderson, 2016). Results from this and other studies of joint networks exposed at the Earth's surface can be applied to deduce important properties of subsurface rocks.

## 1.2 Project aims and objectives

This study investigates the temporal development of joint networks and the control on spatial distribution of network properties asserted by remote stresses, local stresses and pre-existing structures. The project combines field observations and state-of-the-art digital imaging techniques (high-resolution unmanned aerial vehicle [UAV] imagery) to analyze the geometry, chronology and topology of a joint network that deforms excellent exposures of limestone bedding along the Somerset coast in the U.K. Specifically, the project will address the following objectives:

1) To **determine** the number of joint sets and their relative chronology
2) To **illustrate** the spatial and temporal variability in joint development
3) To **examine** how progressive jointing contributes to increased connectivity and block break-up
4) To **identify** the controls of earlier structures
5) To **discuss** how such spatio-temporal variations in joint networks relates changing stress patterns

Advancing UAV technology, combined with novel tools in the description of fracture networks by means of topological measures, allows for a quantification of spatial variability in network properties which is absent in previous studies. This may increase our understanding of deformational style and stress history during the later stages of basin development.

## 1.3 Study area and data

The study area is located at Lilstock, along the Somerset coast on the southern margin of the Bristol Channel (Fig. 1.1). The main data source for the project is UAV imagery, but the study also comprises data collected during a brief field session in April 2019. The high tidal difference in this part of the UK, combined with shallow topography in the inter-tidal zone, has created a high abundance of world-class exposures. Sedimentary beds of Mesozoic age crop out in large wave-cut platforms, as well as in vertical cliff sections, allowing the sedimentary and deformational structures to be studied in three dimensions. Consequently, the stratigraphy and deformational style along the Somerset coast has been offered considerable interest by geologists, and many publications from the area has resulted in good constraints on the ages of stratigraphic units (Palmer, 1972; Whittaker & Green, 1983) and major deformational events (Nemčok *et al.*, 1995; Peacock & Sanderson, 1999).

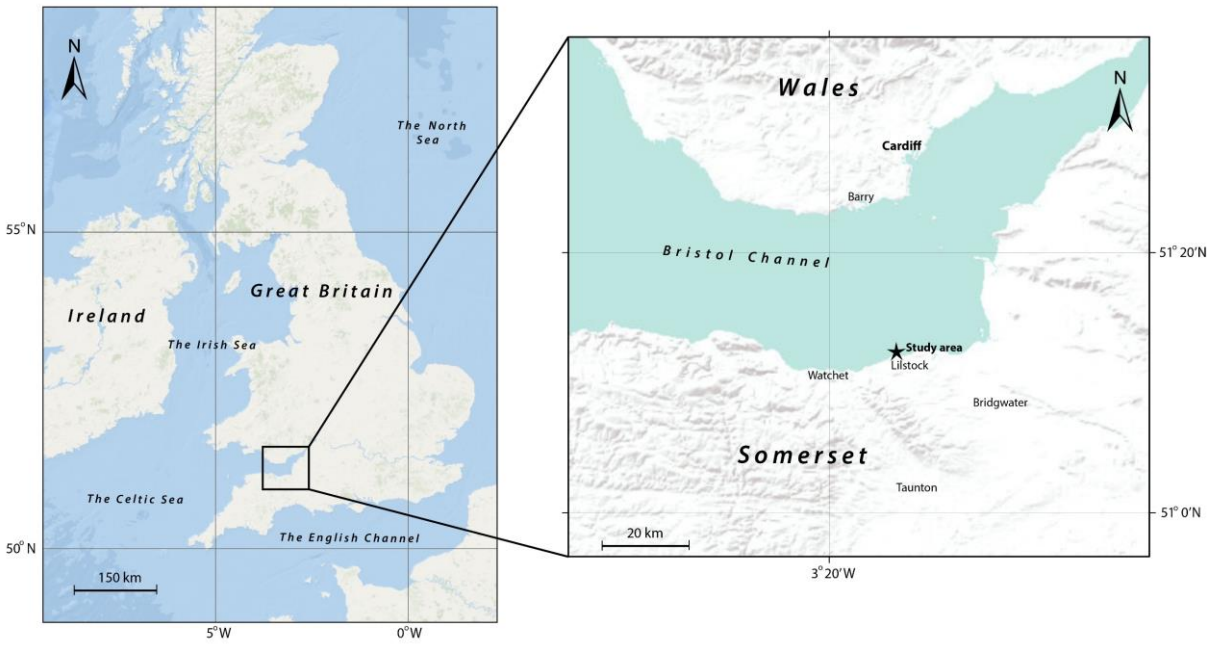


**Figure 1.1**: The location of the field area, along the Somerset coast on the southern margin of the Bristol Channel.

Previous studies have investigated the joints in and near the study area of this project (e.g. Loosveld & Franssen, 1992; Rawnsley *et al.*, 1998; Engelder & Peacock, 2001, Procter & Sanderson, 2018). All of the above conclude that joint formation displays high spatial variability between and within limestone beds. This study focuses on a smaller area (on the $m^2$-scale) than the above-mentioned papers, and a more thorough fracture mapping allows for the

application of refined statistical methods in the detection of joint sets, and in quantifying heterogeneities in network properties.

## 1.4 Thesis outline

Following this introductory chapter, there will be an overview of key concepts in joint network characterization in chapter 2, which focuses on topological terminology in particular. Chapter 3 briefly summarizes major events in the geological history of the Bristol Channel Basin.

Chapter 4 describes the way different criteria have been assessed in the identification of joint populations and their relative chronology. It also describes how networkGT, a newly developed suite of functions developed for the analysis of networks within the framework of ArcGIS, has been used to quantify and map geometrical and topological network properties.

The results, which will be presented in chapter 5, include a description of the identified joint sets, their length scaling properties and their spatial distribution. Furthermore, chapter 5 comprises a quantification of geometrical and topological network properties at different stages of network development, and a documentation of characteristic joint geometries.

Chapter 6 comprises a discussion regarding how joint geometries and distributions reflect stress field and structural inheritance. An important point in this context is the interplay between remote and local stresses, and the resulting joint patterns. This aids the development of a general model for evolution of joint networks in structurally complex settings during later stages of basin evolution.

# 2. Theoretical background

The purpose of this chapter is to build a framework of terminology describing joint morphology and joint formation, and on recognized tools in the characterization of fracture networks, especially topology.

## 2.1 Joints and joint formation

### 2.1.1 Introduction to joints

A joint is a tensile geological fracture that shows extension perpendicular to the fracture plane but has no considerable shear displacement (Peacock *et al.*, 2016a). Joints form when the stress state in a body of rock exceeds its tensile strength, in the opening mode (mode I) of fracture mechanics (Fig. 2.1; Pollard & Aydin, 1988; Engelder, 1987, pp. 29). This typically happens as a response to high pore pressure or thermal-elastic contraction resulting from erosion and uplift (Engelder, 1985).

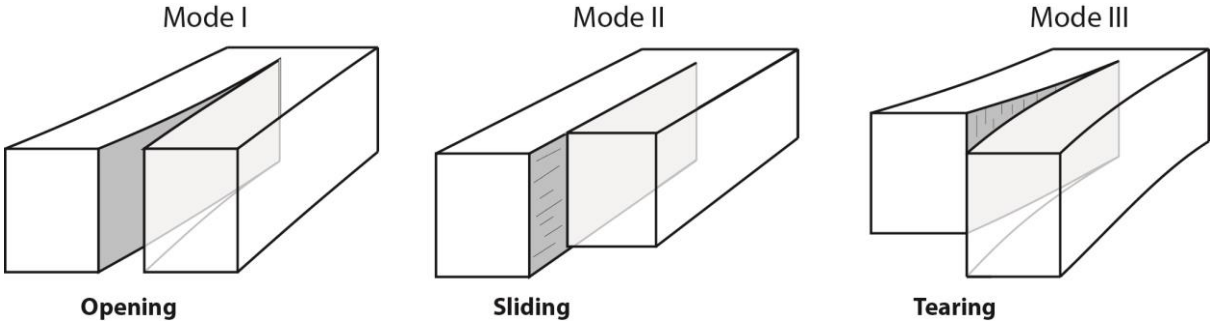


**Figure 2.1**: End member modes of fracture formation. Joint formation is associated with mode I, or the opening mode of deformation (modified from Fossen, 2010, pp. 124).

Joints typically propagate perpendicular to $\sigma_3$, containing both $\sigma_1$ and $\sigma_2$ in the plane (if $\sigma_3 \leq \sigma_2 \leq \sigma_1$ are the principal stresses, and compressive stresses are denoted with positive numbers; Bucher, 1921). In general, joints follow stress trajectories, but may deviate from these as a result of structural inheritance and reactivate pre-existing structures that constitute mechanical anisotropies (Peacock, 2004). When joints are subject to fluid percolation, minerals may crystalize in the joint plane, producing veins (Peacock *et al.*, 2016a). Hence, both joints and veins with the same orientation can form simultaneously, as a response to the same stress regime (Fig. 2.2; Bons *et al.*, 2012).

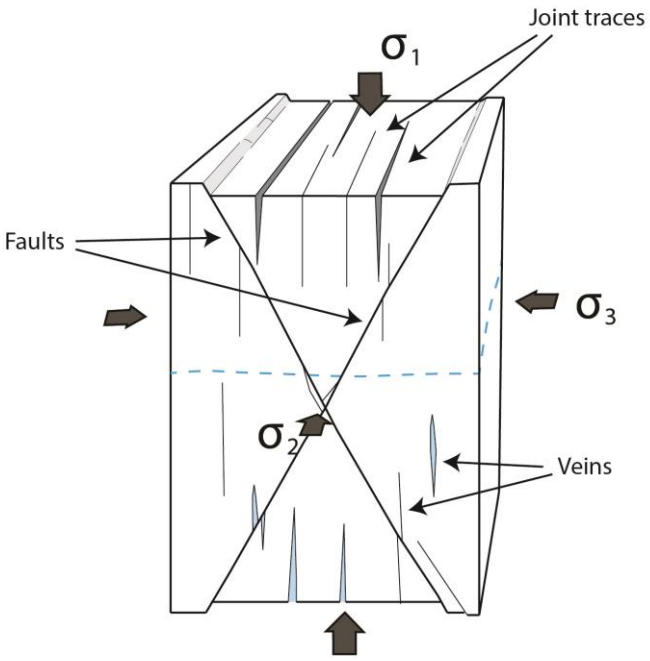


**Figure 2.2:** The orientation of joint propagation in relation to the principal stress axis. When subject to fluid percolation the joints may host mineral precipitation, resulting in veins (modified from Fossen, 2010, pp. 122).

### 2.1.2 Joint morphology

A joint consists of two surfaces (walls) that oscillate around an average plane (Mourzenko *et al.*, 1999). The walls of the joint may display characteristic textures, e.g. rib marks, which may be indicative of joint initiation and propagation (Hodgson, 1961; DeGraff & Aydin, 1987; Pollard & Aydin, 1988). The distance between the walls constitutes the joint aperture, a property which has great importance for e.g. hydraulic properties (Mourzenko *et al.*, 1999). Opening-mode fractures with large apertures are occasionally referred to as fissures, though this term is not precisely defined within scientific literature (Peacock *et al.*, 2016a). In most settings, it is sufficient to think of a joint as a single planar or curved surface in space (spanned by $\mathbb{R}^3$), where the termination constitutes a line (DeGraff & Aydin, 1987).

Mapping geological structures in three dimensions is notoriously difficult, as rocks are usually not transparent, and consequently, the study of joints is often limited to two dimensions ($\mathbb{R}^2$). The 2D projections of joints correspond to joint traces, which represent the lines of intersection between joint planes and the surface of an outcrop. Joint traces are frequently mapped in two dimensions, along bedding surfaces, cliff sections etc. (Sanderson *et al.*, 2018). When near-vertical joints are studied along sub-horizontal bedding surfaces, the strike of each joint trace represents the local orientation of $\sigma_H$ at the time of joint propagation (Rawnsley *et al.*, 1992). The intersections between joints, which constitute lines in $\mathbb{R}^3$, are represented as points when

projected onto a surface, $\mathbb{R}^2$ (Sanderson *et al.*, 2018). Joints can also be studied in one dimension, e.g. along scan lines. In this case, joints are represented as points, spanned by $\mathbb{R}^0$ (Gillespie *et al.*, 1993).

### 2.1.3 Stratabound and non-stratabound joints

In layered sequences of sedimentary rocks, joints are commonly classified as stratabound or non-stratabound (Helgeson & Aydin, 1991; Odling *et al.*, 1999; Rustichelli *et al.*, 2013). Stratabound joints, which terminate against bedding surfaces (Fig. 2.3), are characteristic for shallow deformation in the upper crust, where the length-/height ratio of joint planes may exceed 200 (Loosveld & Franssen, 1992). Large mechanical differences between interbedded sedimentary layers or weak adhesion between adjacent beds may cause joint arrest at layer interfaces (Ladeira & Price, 1981; Odling *et al.*, 1999).

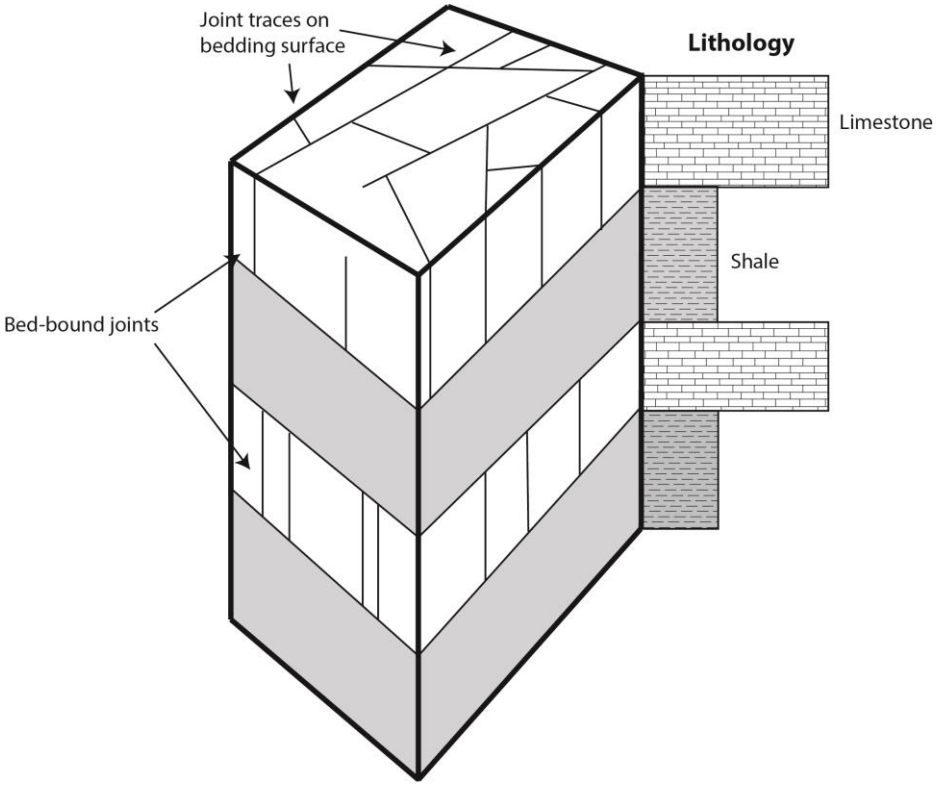


**Figure 2.3**: Layered sequence consisting of interbedded shale and limestone. The limestone beds host layer-bound, layer-perpendicular joints. Joint trace mapping on the bedding surfaces, provides little information about the vertical persistence of the joints.

## 2.2 Joint sets

### 2.2.1 Regional and local joint sets

The term “joint set” is commonly used to refer to a population of systematic parallel joints, though in certain contexts, other attributes are used in the definition of sets (Wheeler & Dixon, 1980; Segall & Pollard, 1983). Bourne & Willemse (2001) use the term “regional joints” about sets of joints which have the same orientation in a large area. Regional tectonic stress caused by e.g. lithospheric flexure or burial and uplift cycles may cause joints with similar trend directions to persist over hundreds of kilometers (Engelder, 1987, pp. 33; Billi & Salvini, 2003).

Existing structures affect the magnitude and orientation of effective stresses in their proximity (Engelder & Gross, 1993; Bai *et al.*, 2002). Sets of “local joints” may therefore not reflect large scale tectonic stresses, but rather stress perturbations (alternatively: stress shadows) induced by existing structures (Simon *et al.*, 1988; Engelder & Gross, 1993). Folding may result in localized extension in the fold hinge as a result of orthogonal flexure, which may lead to joint formation parallel to the fold axial plane (Currie, 1962; DeGraff & Aydin, 1987). Flexural flow may, on the other hand, imply localized extension and fold-parallel jointing in fold limbs (Ramsay, 1962; Engelder & Peacock, 2001). These are examples on local joint sets propagating perpendicular to the regional $\sigma_1$, due to the control asserted by “local stresses”.

Stress field perturbations around faults can be measured directly (Zoback & Pollard, 1978), shown with numerical and analogue experiments (Kattenhorn *et al.*, 2000; Maerten *et al.*, 2002) or be inferred from joint patterns (Fig. 2.4; Olson & Pollard, 1989; Peacock & Mann, 2005). Rawnsley *et al*. (1992) and Bourne & Willemse (2001) conclude that the stress field is more strongly perturbed along certain segments of fault planes, which are associated with stress concentrations. Engelder & Peacock (2001) point out that such stress concentrations to a certain extent can be related to the mechanical properties of the beds in a layered sequence. Such complex stress perturbations result in local sets of curving joints, which are indicative of interplay between local and regional stresses (Bourne & Willemse, 2001). Deviations from the regional stress field may also be caused by joints, and can be responsible for secondary joint populations (Simon *et al.*, 1988; Olson & Pollard, 1989; Caputo, 1995).

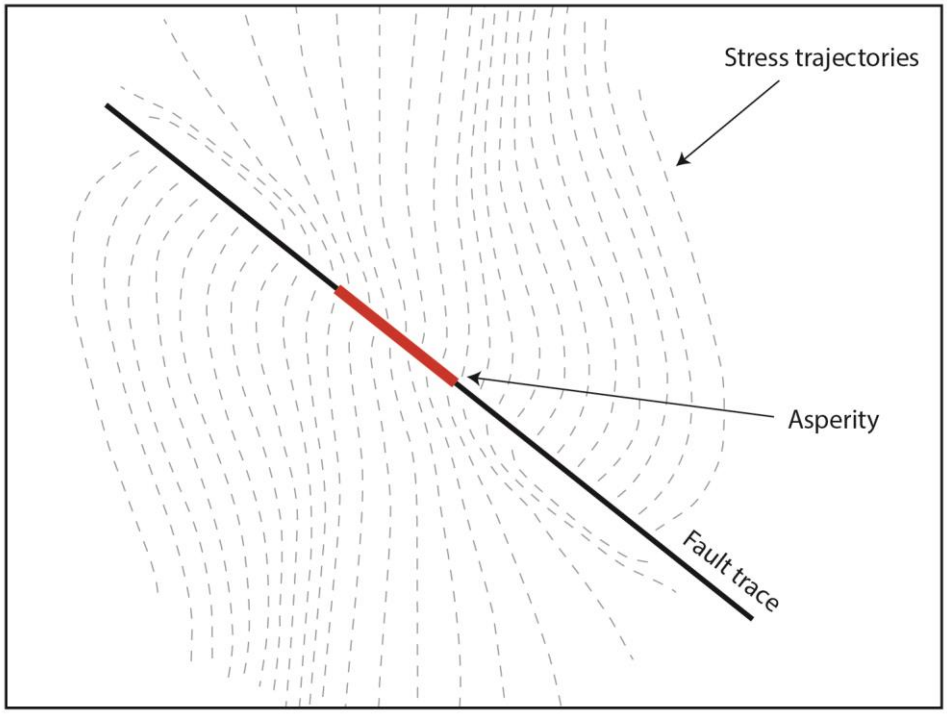


**Figure 2.4**: Tensile stress trajectories (perpendicular to $\sigma_3$) around a fault trace, estimated from numerical modelling based on a linear elastic model of stress. The asperity, which represents a fault segment with no slip, affects the stress distribution locally and reproduces observed joint geometries. Modified from Bourne & Willemse (2001).

### 2.2.2 Length scaling of joint sets

Much work has been done to characterize joint sets in terms of their scaling distribution properties, and length is one of the physical attributes of geological fractures which is shown to follow scaling laws (Segall & Pollard, 1983; Gillespie *et al.*, 2001). Different distributions, most notably log-normal, negative exponential and power-law have been found to describe the length scaling of natural joint sets (Odling, 1997; Odling *et al.*, 1999; Bonnet *et al*., 2001). In this discussion about length scaling properties, $n(l)$ refers to the cumulative frequency of the fractures with a trace length longer than the length $l$.

For a log-normal distribution, which has been found to represent various natural fracture networks (Mourzenko *et al.*, 2005; Davy *et al.*, 2013), $n(l)$ can be expressed:

$$n(l) = \frac{e^{-\frac{(\log(l)-\mu)^2}{2\sigma^2}}}{l\sigma\sqrt{2\pi}} \qquad \textbf{Equation 2.1}$$

where $\mu$ is the mean length, and $\sigma$ is the variance (Bonnet *et al.*, 2001). A log-normal distribution will appear as a straight line when $\log(l)$ is plotted against the number of standard deviations (Fig. 2.5 a; Nyberg *et al.*, 2018).

For negative exponential distributions, $n(l)$ can be expressed:

$$n(l) = ce^{-\frac{l}{l_0}} \qquad \textbf{Equation 2.2}$$

where $c$ is a constant and $l_0$ is a characteristic scale resulting from physical properties of the rock or feedback mechanisms during fracture propagation (Bonnet *et al.*, 2001). A negative exponential distribution will appear as a straight line when the length is plotted against the log of the cumulative percentage (Fig. 2.5 b; Nyberg *et al.*, 2018).

Power law distributions are described by the equation

$$n(l) = cl^{-a} \qquad \textbf{Equation 2.3}$$

where $c$ and $a$ are constants (Bonnet *et al.*, 2001). For a fracture population which follows a power law distribution, $n(l)$ will form a straight line between certain upper- and lower bound values when the log of the length is plotted against the log of the cumulative percentage (Fig. 2.5 c; Nyberg *et al.*, 2018).

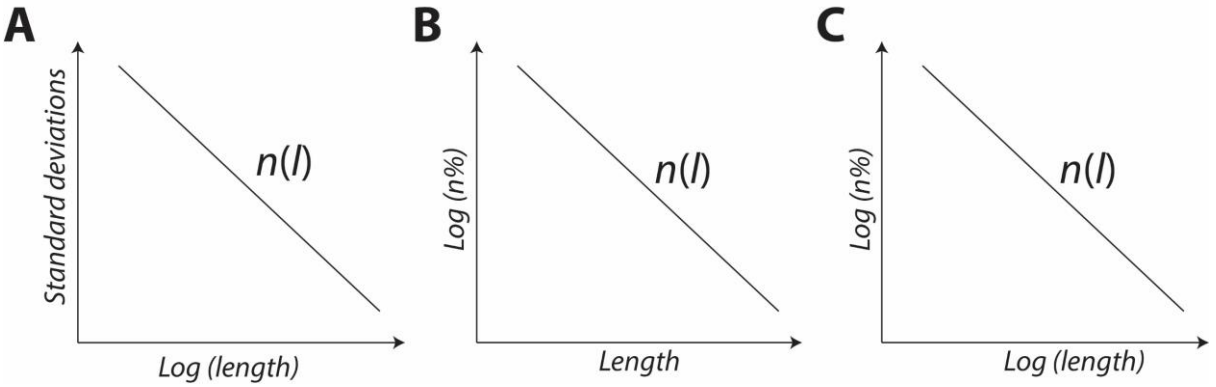


**Figure 2.5**: Plots of $n(l)$ when the length scaling data follows log-normal length distribution (**a**), negative exponential distribution (**b**) and power-law distribution (**c**).

It is in many cases difficult to determine the scaling properties of a population of joints (Bonnet *et al.*, 2001). Einstein & Baecher (1983) show, for instance, that a population with power-law length scaling distribution may appear as log-normal as an attribute of under-sampling of low values due to insufficient data resolution. The controls on length scaling properties of geological fractures is a subject of debate within the scientific community, though it is widely accepted that layer thickness, elasticity and feedback mechanisms during fracture formation play important roles for the scaling properties and spacing attributed to joint sets (Narr & Suppe, 1991; Bai & Pollard, 2000).

## 2.3 Joint networks

### 2.3.1 Joint interaction

Different styles characterize the interaction when new joint sets propagate in the proximity of pre-existing ones. Peacock *et al.* (2018) describe different geometries that characterize relationships between interacting fractures (Fig. 2.6), including;

- *Abutting relationships*. New joints are prone to arrest along the edges of old ones, creating Y-shaped or T-shaped intersections. Perpendicular intersections of curving joints indicate that the older joint induce a local stress field reorientation (Engelder & Gross, 1993), and allows for a determination of the relative chronology between the joints (Hancock, 1985).
- *Reactivation*. New joints may link with tips of older joints, creating long joint traces with straight segments connected by one or more curves. This geometry may be ascribed to stress field perturbations associated with crack-tip mechanisms (Olson & Pollard, 1989), and does not in itself allow for determination of the chronological relationship between the joint sets.
- *Cross-cutting*. New joints may cross-cut older joints, creating an intersection geometry that does not indicate the relative age relationship between them. This type of intersection is found to be rear in many natural joint networks, and Peacock *et al.* (2018) postulate that joint traces which appear to mutually cross-cut are often the result of two joint traces abutting a third joint at the same location by coincidence.

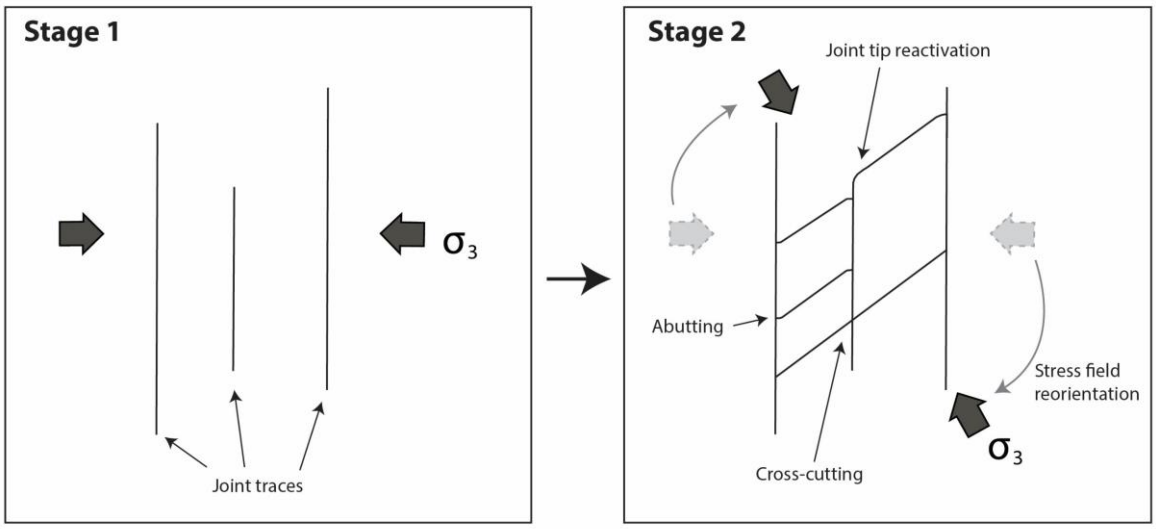


**Figure 2.6**: Development of a fracture network consisting of two joint sets. Interaction geometries include abutting, tip reactivation and cross-cutting.

### 2.3.2 Joint network patterns

A joint network can be characterized by different patterns which are indicative of the stress field and the physical properties of the material in which the joints have propagated (Lamarche *et al.*, 2012). Joint networks can be characterized as monodisperse if all the joint traces are about the same length, or polydisperse if different joint populations have different length characteristics (Mourzenko *et al.*, 2005).

Long joints that are parallel in a region are indicative of tectonic stress (Pollard & Aydin, 1988). When one or more sets of "primary" joints exist in a body of rock, the traces are often linked by secondary cross-joints (Caputo, 1995). Cross joints tend to be shorter than the primary joints, and their formation may result in an orthogonal or oblique ladder pattern, depending on the angle between the primary and secondary joint sets (Fig. 2.7 a; Gross, 1993; Bai *et al.*, 2002). Formation of cross joints is controlled by remote stress and/or stress perturbations related to the set(s) of primary joints (Engelder & Gross, 1993).

Horizontally isotropic tension, i.e. a stress field where $\sigma_1 \approx \sigma_v$ and $\sigma_2 \approx \sigma_3$, may lead to the formation of a network consisting of polygonal joints (Fig. 2.7 b). This pattern may for instance result from exhumation of sedimentary rocks, when a decrease in confining pressure can result in pervasive jointing in a stress field with little or no differential stress in the horizontal plane (Weinberger, 1999).

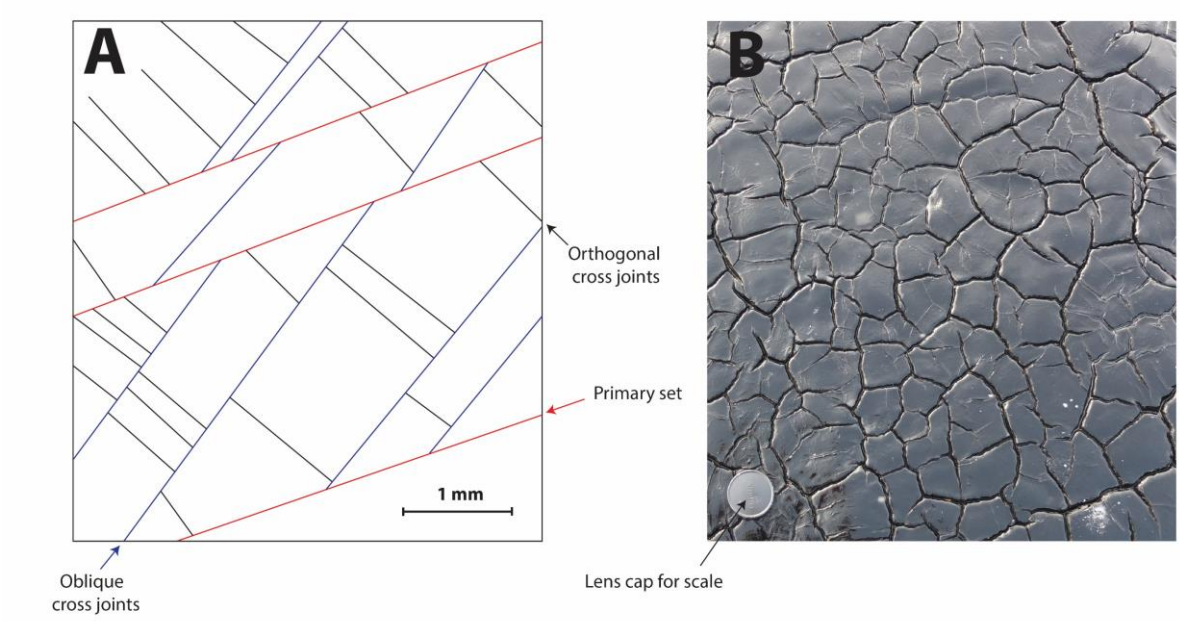


**Figure 2.7**: Different joint network styles resulting from different stress fields and material properties. **a**) Trace map of joints formed in an analogue experiment deforming brittle varnish. Oblique cross joints and orthogonal cross joints constitute ladder patterns. Modified from Rives *et al.*, 1994. **b**) Pattern of polygonal jointing in tar, formed under horizontally isotropic tension.

### 2.3.3 Network intensity

Joint intensity is a geometric network property that is of great importance for physical properties of the rock in which a network exists. The intensity can be assessed to quantify damage in a fault zone (Billi *et al.*, 2003) and may have major implications for rock porosity (Welch *et al.*, 2015). In three dimensions, the intensity corresponds to the area of joint surface per unit volume of rock. Joint intensity in two dimensions corresponds to the total trace length per unit area of exposure, whereas in one dimension joint intensity corresponds to the number of crossings per unit length (Sagy & Reches, 2006). All of the above-mentioned ways to measure joint intensity do, however, yield a value with the unit length to the power of minus one.

## 2.4 Topological concepts and terminology

### 2.4.1 Node/branch model

It is usual to differentiate between geometrical (e.g. length and orientation) and topological attributes of a fracture network (Sanderson & Nixon, 2015). Topological network properties are the ones that describe the relationships between the elements constituting (Sanderson & Nixon, 2015). Quantifying topological properties of fracture networks has proven to be particularly useful to assess network connectivity, a network property that has great implications for e.g. the potential for percolation within rocks (Sanderson & Nixon, 2018). Unlike the geometrical aspects of a joint network, topological properties are generally expressed through dimensionless parameters (Sanderson & Nixon, 2015). Topological characterization of geological fracture networks has been proven to be efficient and applicable at any scale (Jing & Stephansson, 1997; Duffy *et al.*, 2017).

Topologial characterization of joint networks can be done with a two-dimensional map of joint traces. Sanderson *et al.* (2018) discuss the similarities between an outcrop surface and the domain of a graph. From the point of view of discrete mathematics, the elements of a fracture network constitute a graph which is built up by branches and nodes, not trace lines, as the most basic entities (Sanderson *et al.*, 2018). In this context, a node is either an intersection with another joint trace, or the end of a joint trace if it terminates as a free tip (Fig. 2.9). Branches are the joint trace segments that connect the nodes, such that every joint intersection or termination constitutes a node that is connected by at least one branch. The network components that are fully connected by a network of branches, is commonly referred to as a cluster or tree (Fig. 2.9; Sanderson & Nixon, 2015). If a joint network is sparsely exposed, topological analysis

is preferential because branch analysis is less likely to be affected by censoring effects than joint traces are (Sanderson & Nixon, 2015).

### 2.4.2 Node classification

From a topological point of view, a trace map of a natural joint network primarily consists of three node types (Fig. 2.9), as defined by e.g. Sanderson & Nixon (2015);

- *I-nodes*, where joints terminate as a free tips on the trace map. This is defined as an isolated node which has degree one, because each I-node connects to only one branch.
- *Y-nodes*, where joints abut each other. This is defined as a connecting node type, since it connects more than one branch. Because three branches intersect at each Y-node, Y-nodes have degree three.
- *X*-nodes, where joints cross-cut each other. This is also a connecting node type, where each X-node connects four branches and has degree four.

One could theoretically think of geometries that produce other "apparent node types", for instance if the tips of two sub-parallel joint traces intersect to produce a V-shape. However, the probability of obtaining these node types from natural data is negligible (Sanderson & Nixon, 2015). For practical reasons the E-node (alternatively: edge-node) can be defined as an intersection between a fracture trace and the boundary of the interpreted area (Sanderson *et al.*, 2018). If we look away from the E-nodes, a natural fracture network can be regarded as an IYX-system, allowing node proportions to be plotted in a ternary diagram where I, Y and X are end members (Fig. 2.8). These proportions can reveal important differences between fracture networks which have similar geometrical properties. The evolution of node type proportions can be referred to as the topological pathway of a fracture network (Sanderson *et al.*, 2018).

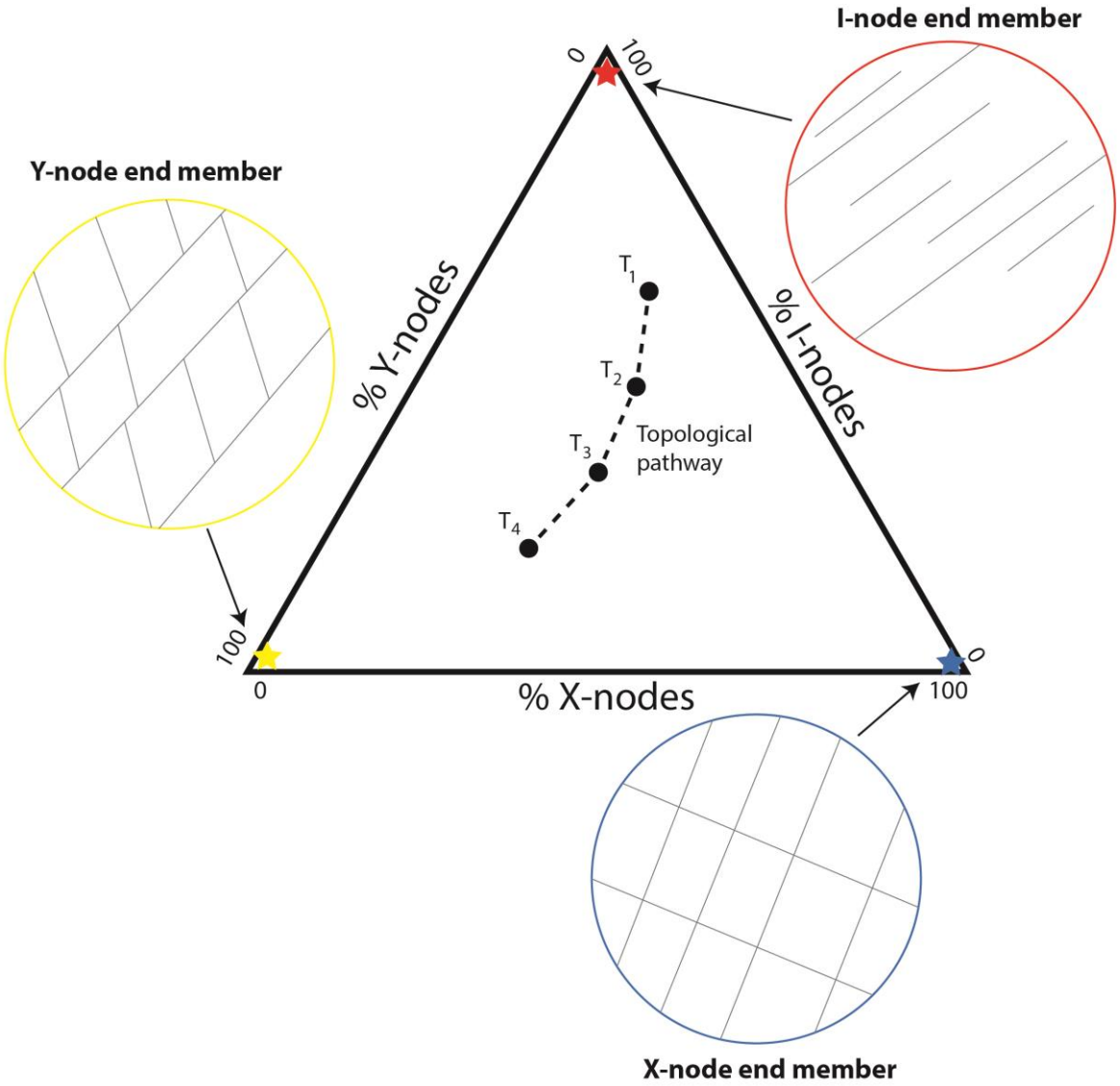


**Figure 2.8**: Ternary node diagram and sketches of associated fracture networks which constitute end members in the IYX-system. Each of the window sampling areas have the same intensity but the topological properties are different.

### 2.4.3 Branch classification

Branches are the line segments that connect the nodes in a network. Considering the three different naturally occurring node types (I, Y and X), six different branch types exist; II, IY, YY, YX and XX. E.g. Manzocchi (2002) categorizes branches based on the connecting properties of the nodes they connect. Since I-nodes are isolated whereas Y-nodes and X-nodes are connecting, the branches can be categorized in three classes;

- *II-branches*, which connect two isolated nodes.
- *IC-branches*, which connect one isolated and one connecting node.
- *CC-branches*, which connect two connecting nodes.

In addition to these, one class of branches connect E-nodes. If we look away from these, the proportions of II, IC and CC can be plotted in a ternary diagram and is an additional measure of network connectivity (Duffy *et al.*, 2017).

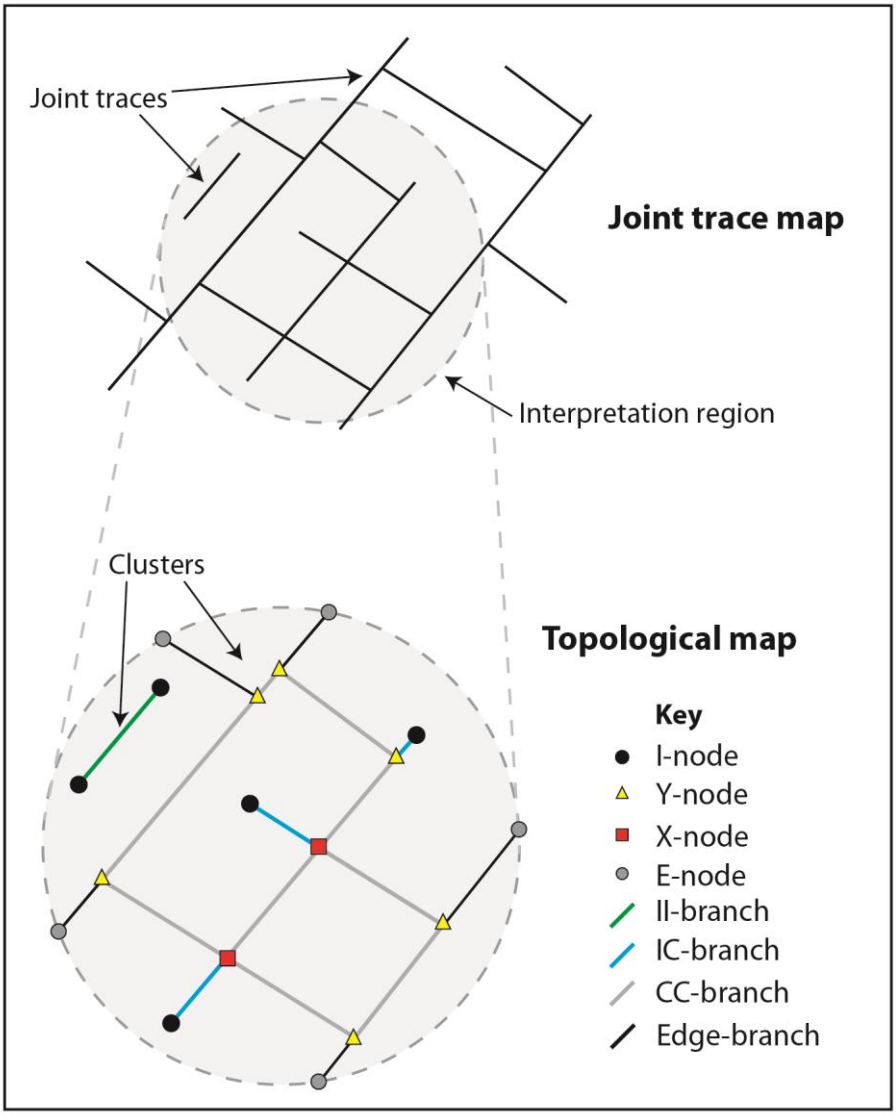


**Figure 2.9**: Trace map sketch and the resulting components identified in a topological analysis.

### 2.4.4 Topological measures

Another topological entity that is important for the study of fracture networks, is the block. On trace maps, blocks correspond to areas that are confined by joint traces (i.e. inside joint clusters). Nyberg *et al.* (2018) use the terms "whole blocks" about the blocks that are confined by joint traces on all sides, and "half blocks" about the areas that are confined by joint traces and the boundary of the interpretation region (Fig. 2.10). The number and average size of blocks within an area can be calculated based on the number of nodes, branches and clusters.

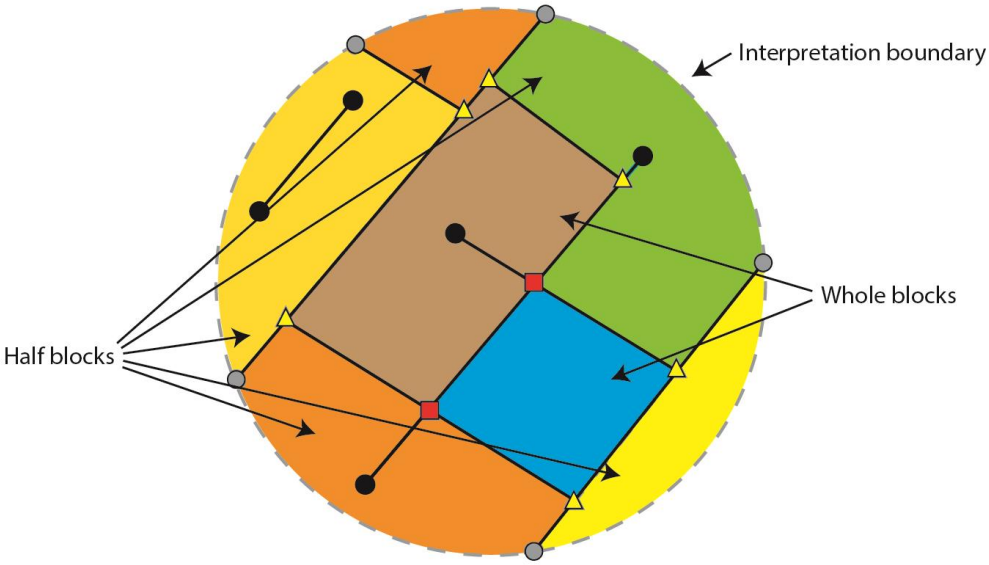


**Figure 2.10**: Blocks in the interpreted area of the joint trace map in Fig. 2.9. This region contains two whole and five half blocks.

Based on counting of topological objects (i.e. nodes and branches) different topological network properties can be calculated. The connecting node frequency, i.e. the frequency of Y-nodes and X-nodes, and the average node degree are two network properties which are important for the connectivity and potential for percolation within joint networks in layered sequences (Sanderson & Nixon, 2018).

# 3. Geological background

The study area, which is located near the settlement of Lilstock, lies on the Somerset coast. To the north lies the E-W trending Bristol Channel, a part of the Celtic sea, which comprises the Bristol Channel Basin (BCB). This chapter focuses on the formation of the BCB and introduces the processes behind each main episode of deformation that has affected the region.

## 3.1 Formation of the Bristol Channel Basin

### 3.1.1 Extensional phase

The BCB developed in the early Mesozoic, with the onset of rifting occurring in the late Permian to early Triassic, as suggested by wedge thickening geometries and the creation of depocenters during this time period (Dart *et al.*, 1995). At this point, $\sigma_3$ was oriented approximately N-S (Fig. 3.1 c), producing normal faults and other extensional structures striking E-W (Fig. 3.1 a; Peacock *et al.*, 2016b). The basin formation may partly have exploited the E-W structural grain, e.g. pre-existing thrusts, originating from the Variscan Orogeny of late Paleozoic age (Brooks *et al.*, 1988). Dart *et al*. (1995) argue that the extension happened in three distinct phases – the first occurring during Late Permian to Early Triassic, the second during Early Jurassic and the last during Late Jurassic.

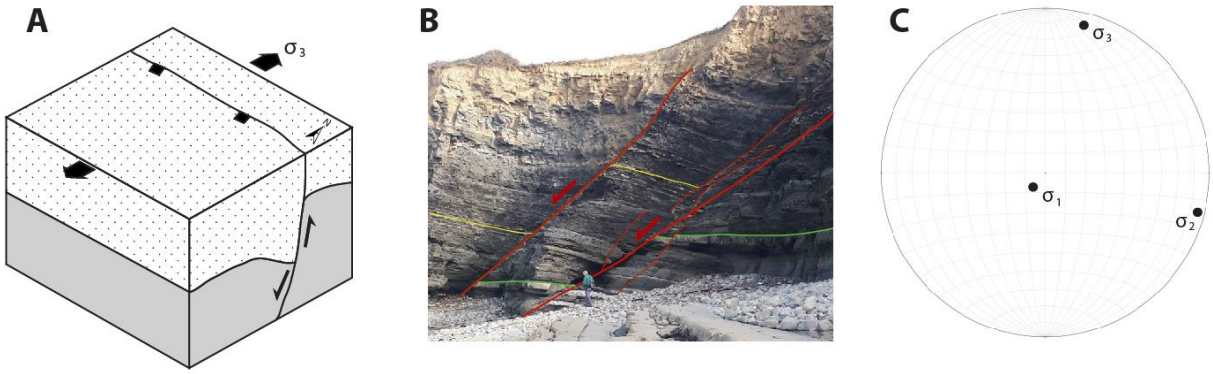


**Figure 3.1: a)** Schematic illustration of the stress field and the resulting structures originating from the rift phase (modified from Dart *et al.*, 1995). **b)** Field photograph (looking east) of Mesozoic normal faults at Kilve on the Somerset coast. The major slip surfaces and marker layers are highlighted. Courtesy to Isabel Edmundson. **c)** Paleostress analysis performed by Peacock & Sanderson (1999), based on the measurement of 146 normal faults originating from the Mesozoic rifting event in the Somerset area.

The Central Bristol Channel Fault Zone (CBCFZ), an en echelon array of S-dipping faults, accommodated most of the stretching, giving most of the BCB an asymmetric half graben geometry (Brooks, *et al.* 1988). Based on structural trends, the BCB can be divided into two

sub-basins: the East Bristol Channel Basin (EBCB) and the Central Bristol Channel Basin (CBCB) trending E-W and ENE-WSW, respectively (Kameling, 1979). The easternmost part of the EBCB can be classified as a symmetric graben-structure, whereas the western part classifies as a half-graben (Peacock & Sanderson, 1999). Extensional structures were formed in both uncompacted and completely lithified sediments as the basin developed (Nemčok *et al.* 1995). The study area is situated on the southern margin of ECBC, which has a structural trend with Mesozoic extensional fractures striking approximately N095E (Fig. 3.2; Peacock & Sanderson, 1999).

Peacock & Sanderson (1999) show that the North Exmoor Fault (NEF) and the North Quantocks Fault (NQF), situated close to the field area on the Somerset coast, are basin-bounding normal faults with offsets up to 1000 m. They juxtapose pre-rift sediments of Devonian and Carboniferous age with Mesozoic syn-rift sediments and are important for understanding the deformational style throughout the study area (Fig. 3.3). Numerous evidence for the Mesozoic rifting event can be found in outcrops throughout the Somerset coast, e.g. outcrop-scale normal faults (Fig. 3.1 b) and fault-parallel calcite veins (Dart *et al.*, 1995), and in seismic sections (Van Hoorn, 1987). At certain localities, arrays of high-density veins (HDVs) trend E-W and are interpreted to derive from the Mesozoic rifting event (Hancock & Caputo, 1998).

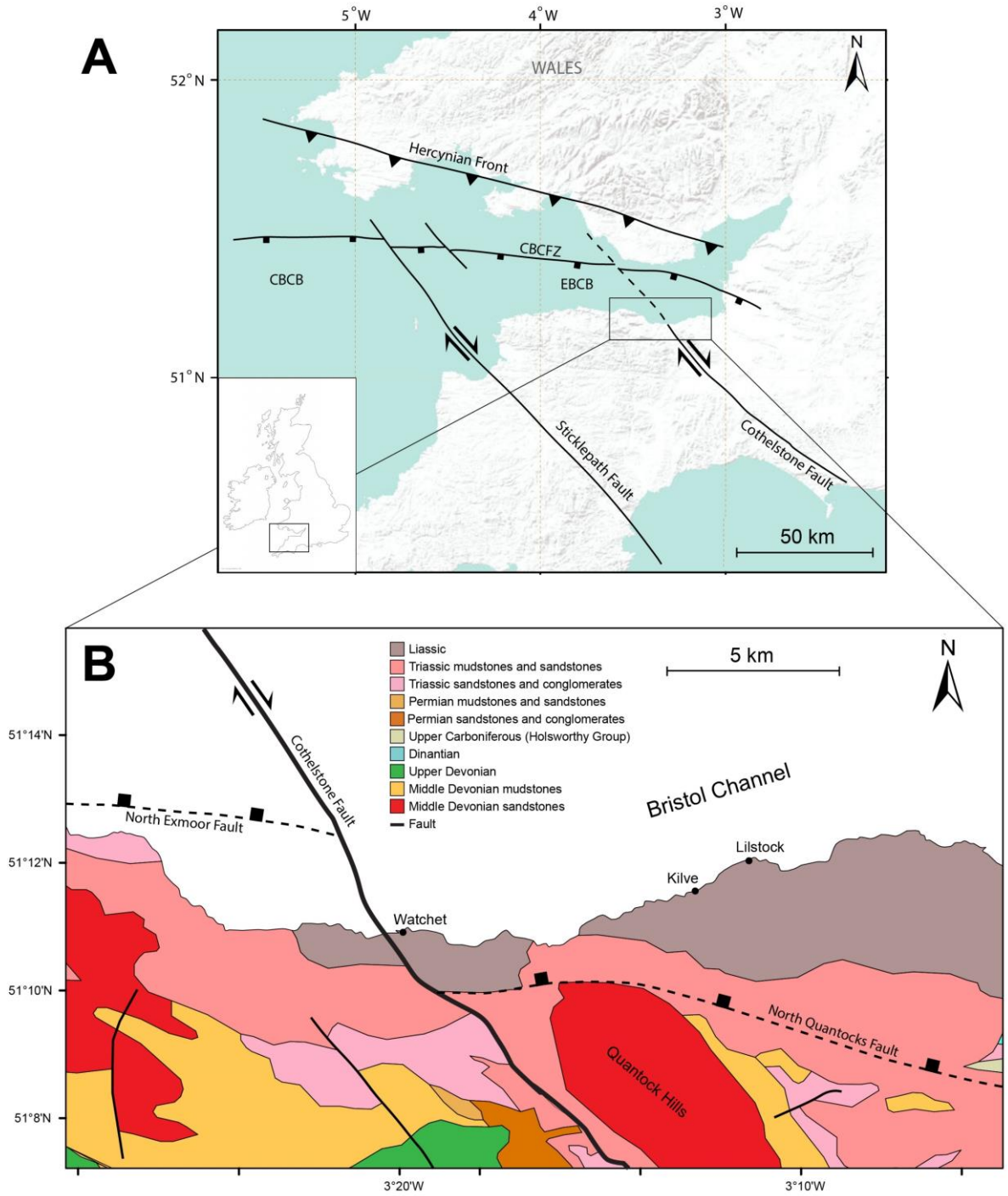


**Figure 3.2**: **a**) The Bristol Channel Basin and its main structural features (modified from Kamerling, 1979 and Dart *et al.*, 1995). **b**) Simplified geological map of the Somerset coast, reproduced from Peacock *et al.* (2017) who based it on maps from the British National Survey. Modifications are based on Dart *et al.* (1995) and Peacock & Sanderson (1999).

### 3.1.2 Deposition in the BCB

As extension and subsidence went on through most of Triassic and Jurassic, a package up to 2250 m of syn-rift sediments was deposited (Van Hoorn, 1987). The basin infill sediments were

deposited on top of Carboniferous limestone and Devonian sandstone and slate, which had been deformed during the Variscan Orogeny, and hence formed a slight angular unconformity (Dart *et al.*, 1995). The syn-rift package comprises Permian and Triassic layers, as well as a Jurassic section that is completely preserved in parts of the basins (Dart *et al.*, 1995). The Blue Lias formation of early Jurassic age crops out on the intertidal platform in the study area, and on numerous other localities along the Somerset coast. It consists of interlayered solid carbonate and shale, corresponding to a shallow marine environment (Kamerling, 1979). The micritic carbonate layers are ranging in thickness from about 0.05 to 0.75 m (Fig. 3.3; McGrath & Davison, 1995). Despite the domination of shale in the stratigraphy, limestone beds dominate the exposures along the Somerset coast. Limestone beds are generally found to have a high lateral continuity and can be used as marker beds over large areas. (McGrath & Davison, 1995). The Liassic carbonates have low porosity but is unlikely to have been buried to a depth exceeding 2000 m (Peacock *et al.* 2016).

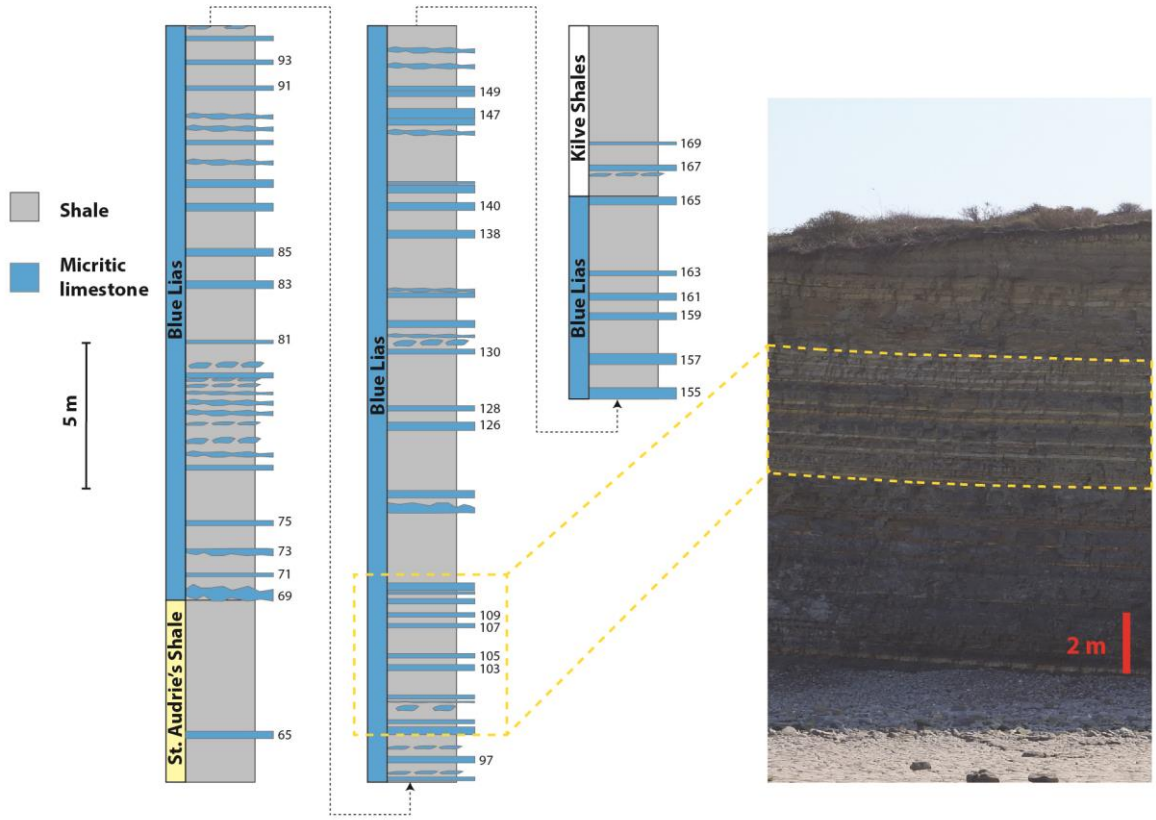


**Figure 3.3**: Part of the lithostratigraphy from the Somerset Coast, modified from Palmer (1972) and Whittaker & Green (1983). The main limestone layers are numbered and can be used as marker beds throughout the region. The field photograph shows beds in the Blue Lias formation that crops out in the cliff section on Lilstock Beach.

Although the extensional phase was over by late Cretaceous, subsidence and deposition still occurred into the Paleogene (Van Hoorn, 1987), resulting in a relatively thin (<500 m) post-rift package of Cretaceous/Paleogene age (Kamerling, 1979).

## 3.2 Post-basinal deformation

### 3.2.1 First phase of strike-slip reactivation

Van Hoorn (1987) presents evidence for a period during late Jurassic to early Cretaceous with dextral strike slip reactivation along some of the N095E trending normal faults. At Lilstock, this phase of deformation is indicated by conjugate arrays of veins and pull-aparts (Peacock & Sanderson, 1995; Peacock & Sanderson, 1999), fault striations and steepened relay ramps (Rotevatn & Peacock, 2018). Peacock & Sanderson (1999) conclude that $\sigma_1$ was probably oriented NW-SE during this interval after the Mesozoic rifting event.

### 3.2.2 Contractional stage

Towards the end of the Cretaceous period, the combined effects of Alpine Orogeny in Southern/Central Europe and the opening of the North Atlantic induced a far field contractional regime on southern England (Nemčok *et al.*, 1995; Underhill & Stoneley, 1998). The strain resulting from Alpine contraction was not evenly distributed, but concentrated in the BCB- and the Wessex Basin areas (Fig. 3.4; Glen *et al.*, 2005; Peacock *et al.*, 2016b).

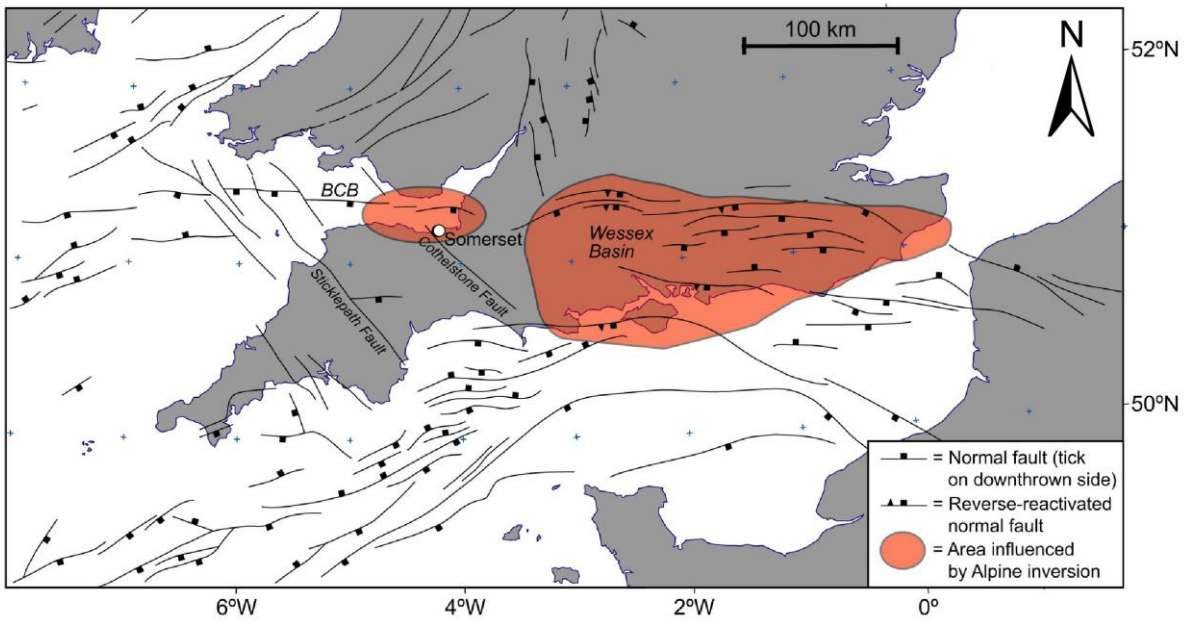


**Figure 3.4**: Area affected by Alpine contraction, modified from Peacock *et al.* (2016) who reproduced it from the Petroleum Exploration Society of Great Britain. The location of the field area is indicated by the white circle.

In southern England, $\sigma_1$ was oriented approximately NNE-SSW during the contractional stage (Fig. 3.5 c), causing mild basin inversion in parts of the BCB, but without considerably increasing the overburden by thrust stacking (Peacock *et al.*, 2016b). This positive inversion led to reverse reactivation of the N095E striking normal faults, and production of other compressive structures that can be studied on the Somerset coast (Fig. 3.5 a; Peacock & Sanderson, 1992). These include N-S striking calcite veins, gentle E-W-striking folds and crenulation cleavage (Dart *et al.*, 1995). Hanging wall buttresses can be seen both in seismic sections and in outcrops (Fig. 3.5 b; Dart 1995).

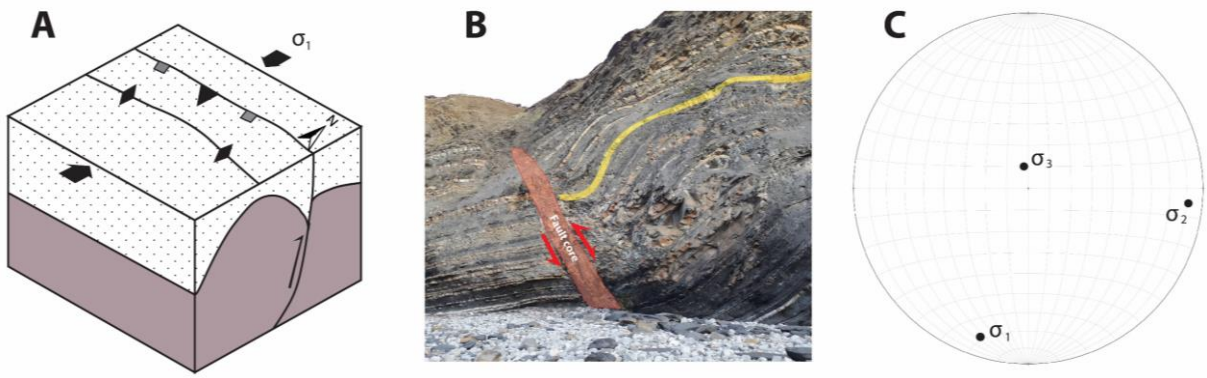


**Figure 3.5**: **a)** Sketch of the deformational style during the basin inversion; reverse reactivation of normal faults and folding (modified from Dart *et al.*, 1995). **b)** Field photograph of the reversely reactivated East Quantoxhead Fault at Kilve on the Somerset coast. The hanging wall was folded, creating a hanging-wall buttress during the contractional stage. Courtesy to Isabel Edmundson. **c)** Paleostress reconstruction based on 40 contractional structures (modified from Peacock & Sanderson, 1999).

### 3.2.3 Second phase of strike-slip faulting

Towards the end of the phase of Alpine contraction, the regional stress field changed, resulting in a strike-slip regime (Fig. 3.6 a; Dart *et al.*, 1995). This may be a result of the Paleogene opening of the Atlantic Ocean, meaning that $\sigma_1$ was still oriented N-S but $\sigma_3$ changed its orientation from vertical to horizontal (Fig. 3.6 c; Peacock *et al.*, 2016b).

Dextral strike-slip fault zones, most notably the Cothelstone and the Sticklepath faults, both striking NW-SE, intersect and offset the CBCFZ and the smaller reactivated normal faults either side of the basin (Fig. 3.6 b; Dart *et al.*, 1995). These fault zones, which appear to be deep-rooted, may stem from the Variscan Orogeny, as suggested by Van Hoorn (1987). The main NW-SE fault population also has a conjugate set of faults striking NE-SW (Peacock *et al.*, 2016b).

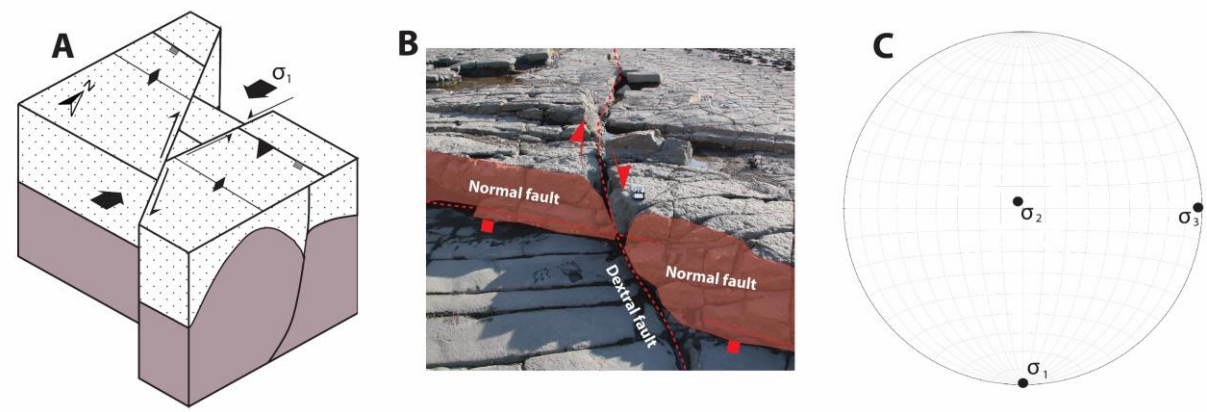


**Figure 3.6**: **a)** Sketch of the deformational style during the strike-slip phase; strike-slip faults cross-cut older structures (modified from Dart *et al.*, 1995). **b)** Field photograph of a normal fault cross-cut by a dextral strike-slip fault in East Quantoxhead on the Somerset coast. The figure is modified from Peacock *et al.* (2017). **c)** Paleostress measurement based on 42 strike-slip fault orientations. Modified from Peacock & Sanderson (1999).

## 3.3 Joint development

Uplift and erosion resulted in exhumation of the Mesozoic sequence during later stages of basin development. This resulted in decrease in confining pressure, which together with post-alpine relaxation enhanced joint formation, primarily in the limestone beds (Fig. 3.7; Peacock, 2004). Abutting relationships indicate that all the joints in the Liassic sequence post-date fault nucleation (Rotevatn & Peacock, 2018). Rawnsley *et al.* (1998) propose that very subtle changes in the stress system is responsible for stress patterns that can be observed throughout the BCB. Most of the bed-bound joint networks in the Mesozoic limestone strata are poly-phase and are believed to result from various episodes of differential stress, combined with a progressive decrease in confining pressure. Rawnsley *et al.* (1998) describe an anticlockwise rotation of the joint sets, suggesting a similar rotation of $\sigma_H$, and divide the joint formation into five phases based on the orientation of remote stress and local controls on joint geometries.

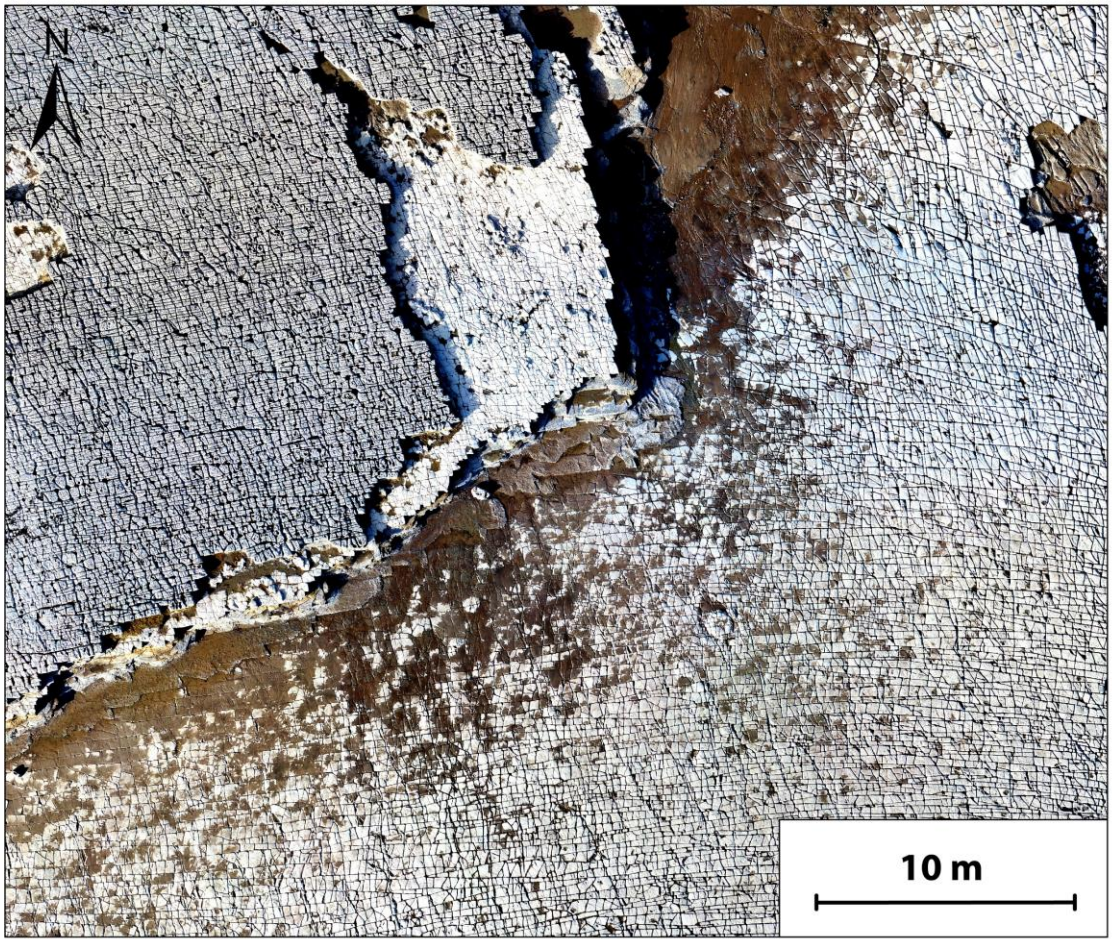


**Figure 3.7**: Jointed limestone bed surfaces in the Blue Lias formation, exposed along the Somerset coast. The jointing patterns and network properties are variable within and between the limestone layers, and some joint traces are curved.

On both sides of the BCB, joints are characterized by curvature in the proximity of faults. Fan structures are created where joint traces radiate from certain segments of a fault trace (Bourne & Willemse, 2001; Rawnsley *et al.*, 1992). This phenomenon results in complex patterns of joint network development. Joints are in some cases proved to reactivate vein arrays associated with the earlier episodes of deformation of the Mesozoic sediments (Peacock, 2004). Rawnsley *et al.*, 1998 speculate that HDVs are responsible for the jointing style in certain beds. Procter & Sanderson (2018) demonstrate that there are major differences in jointing styles and joint network properties within and between layers, indicating a complex stress field and distribution of jointing.

# 4. Methodology

This study combines digital imaging techniques (UAV imagery) with field observations. This chapter explains the steps leading up to and constituting the spatio-temporal development analysis. The methodological workflow is shown in Fig. 4.1.

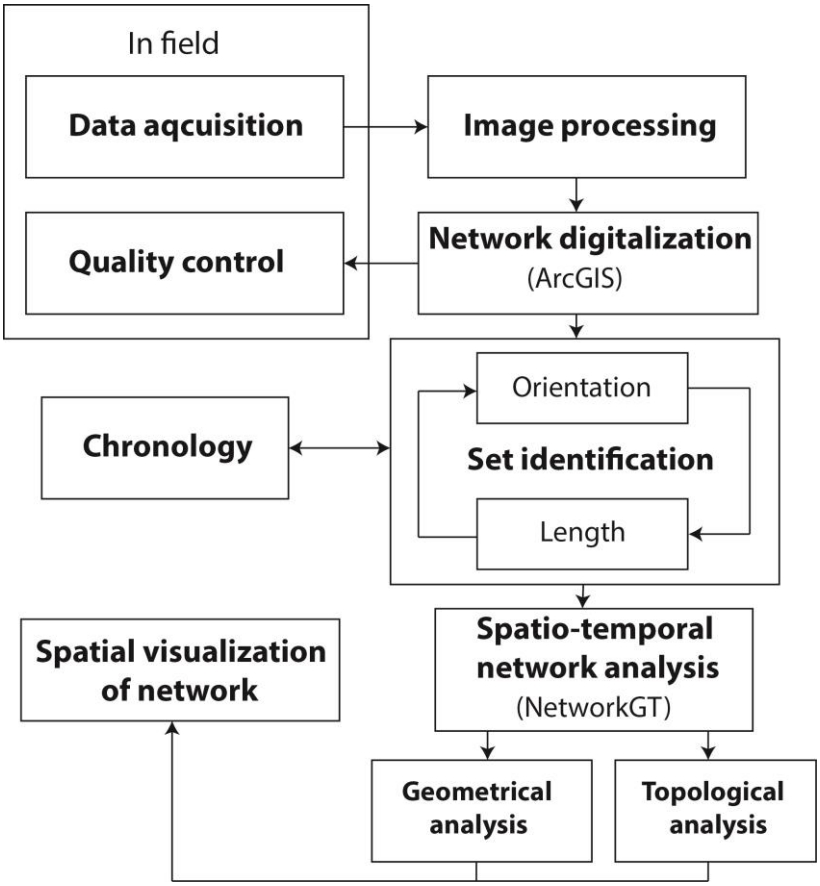


**Figure 4.1**: Simplified flow chart for the workflow in this study.

## 4.1 Data acquisition and processing

### 4.1.1 Data

The study uses state of the art digital imagery, collected by an UAV in 2017 at low-tide when the wave-cut platform was most exposed. The imagery was collected at an altitude of 30 m, providing a pixel resolution of <1 cm, which is more than adequate for identification and digitization of joints and faults on the wave-cut platform (Salvini *et al.*, 2017). Images were processed, merged and georeferenced using Agisoft, an image rendering software, resulting in a photo orthomosaic covering ~53 900 $m^2$ of the inter-tidal platform (Fig. 4.2).

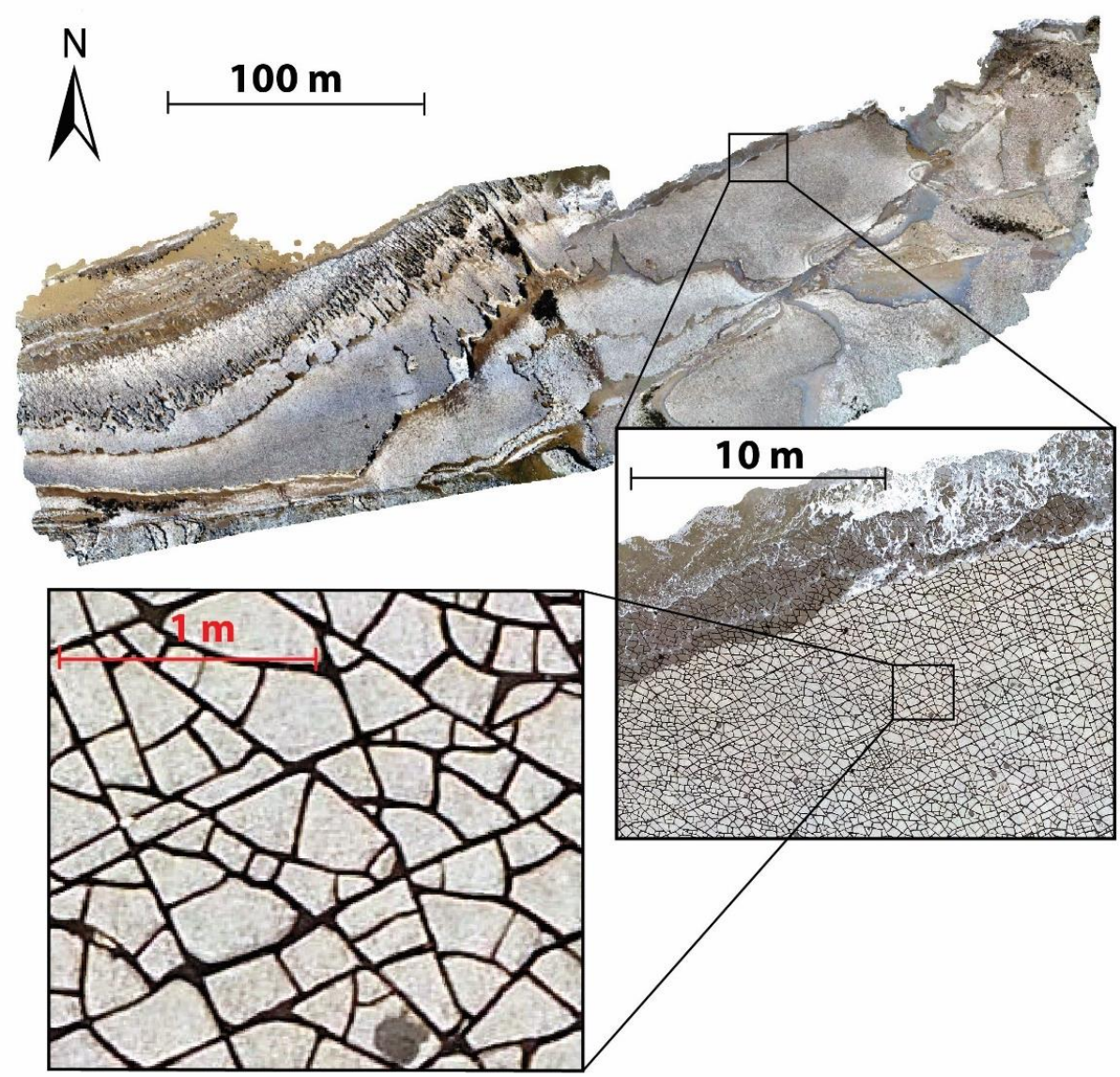


**Figure 4.2**: The UAV imagery, which is the main data source for this project. The high resolution allows for a precise interpretation of fracture traces along the bedding surface and has <1 cm pixel resolution.

The photomosaic from Agisoft was imported and georeferenced in ArcGIS for interpretation and analysis. ArcGIS has been used to map fracture networks, and provides an efficient means to visualize network properties (Bhattacharyya & Czeck, 2008). Further steps in the joint network analysis were performed in ArcGIS and aided by NetworkGT, a newly developed GIS toolbox developed to sample, analyze and map different geometrical and topological attributes of two-dimensional fracture maps within the mapping environment of ArcGIS (Nyberg *et al*., 2018).

### 4.1.2 Interpretation and digitization

The UAV imagery, combined with field observations, allowed for a precise mapping on the cm scale along the limestone bedding surfaces. A suitable area of 3 244 $m^2$ in the immediate

hanging wall of a normal fault was chosen for joint digitization (Fig. 4.3). This area contains only one exposed limestone bed, which eliminates the effect on spatial variability of jointing due to layering and bed thickness (Procter & Sanderson, 2018), and is ideal to evaluate spatial variations within the layer. The size of the interpretable region is constrained by the size of the outcrop, as well as the time available for manual digitization of the joints as joint digitization is a demanding and time-consuming process (Wu & Pollard, 1995).

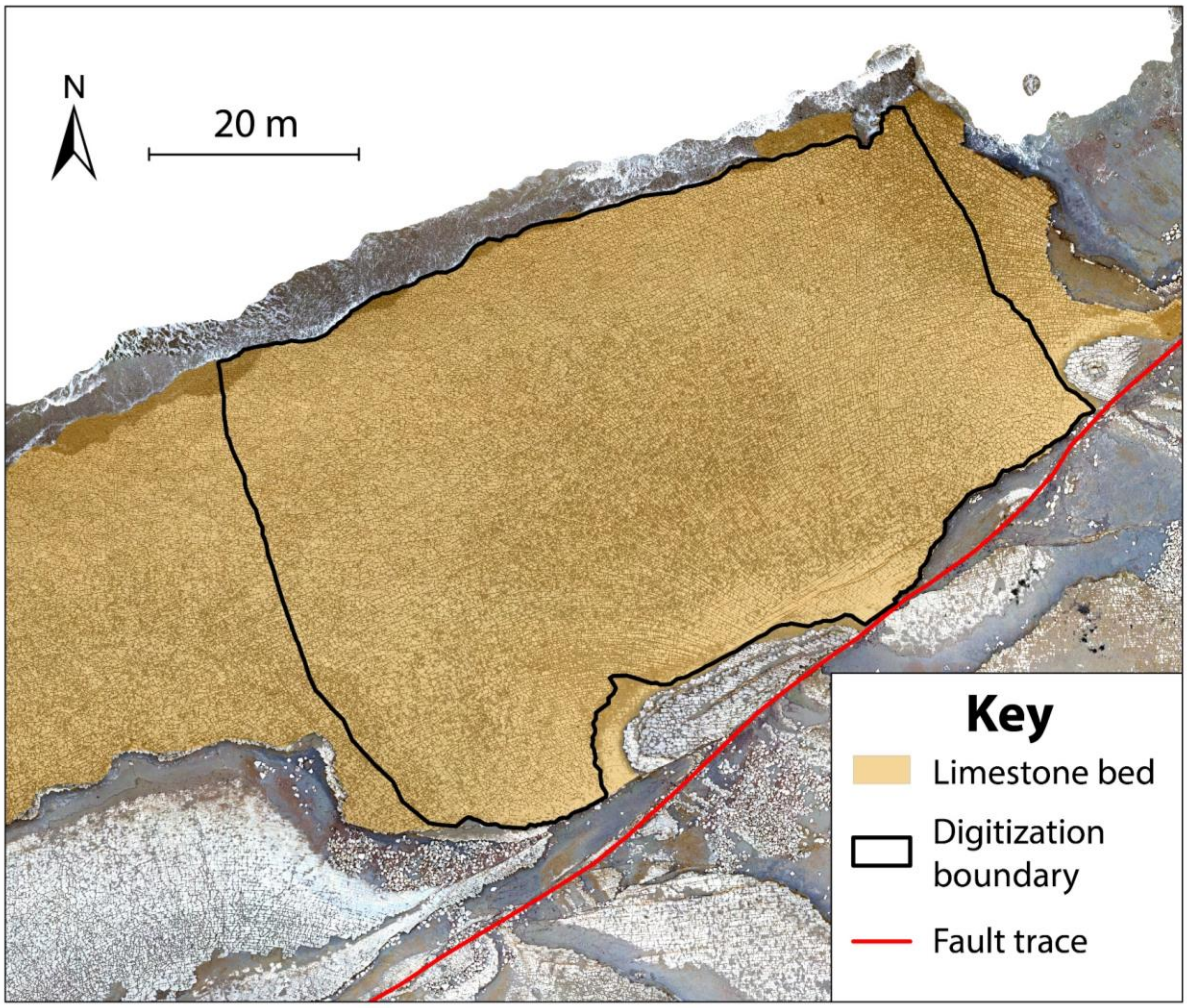


**Figure 4.3:** Extent of the studied limestone bed and the chosen interpretation region.

All the joint traces were interpreted and digitized manually inside the digitization boundary, resulting in a 2D map of joints along the bedding surface (Fig. 4.4). This interpretation was based solely on the drone images, as it was performed before the field session.

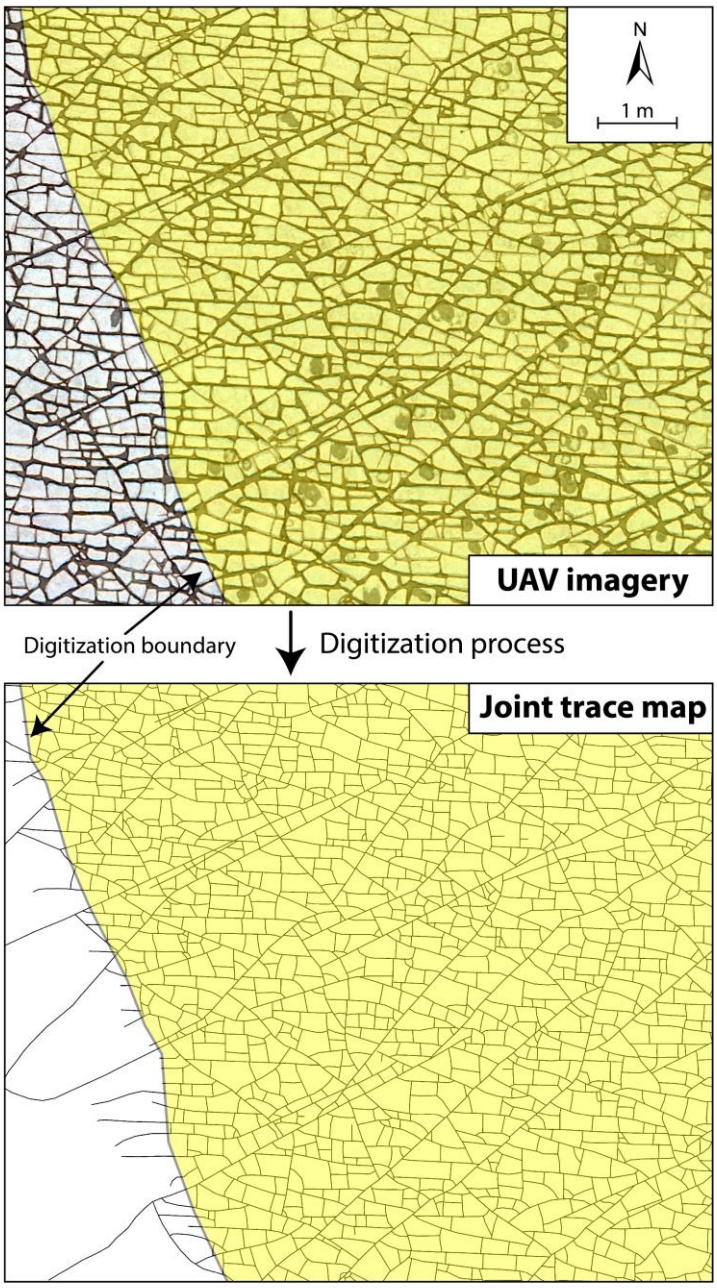


**Figure 4.4:** 2D joint trace map within the interpretation region. Some joints extend outside the area of digitization.

It is important to "snap" the digitized joint polylines, such that each digitized joint exactly abuts another joint, where appropriate. This allows for analysis of topological network properties. The result of the interpretation was a network of polylines with associated geospatial information (i.e. x,y coordinates), which enabled geometrical and topological analysis of the network (Procter & Sanderson, 2018). Because each polyline represents a single fracture trace, the attributes of the polylines (i.e. length, strike etc.) can be used directly to interpret joint characteristics (Nyberg *et al*., 2018).

### 4.1.3 Field observations

Interpretations of the UAV imagery were ground-truthed in the field and were supplemented by field observations and data collection. The beds were correlated to the ones numbered by Whittaker & Palmer (1983), to compare with previous studies and to estimate throw across the fault. The thickness of the studied limestone bed was measured at various places, both on the wave-cut platform and in the cliff section, in order to investigate the lateral persistence of the layer. The orientation of the most prominent faults within the study area were measured, and the vein arrays in the limestone layer were documented.

## 4.2 Identification of joint sets

### 4.2.1 Identification of fanning joints

In order to group joint traces into sets based on their orientations and lengths, it was necessary to manually extract the fan-joints from the trace map, as their strike is too variable to yield meaningful results in a strike-length analysis. This was done visually, based on length (>1.5 m), curvature and splaying characteristics (i.e. curving away from the fault trace, fitting with the regional fan array). The result of this step of the analysis was two separate joint trace maps, one for the fanning joints and one for the non-fanning ones (Fig. 4.5). Based on the relation to the fan, four circular window sampling areas with diameter of 10 m were chosen to document spatial differences in network development within the study area.

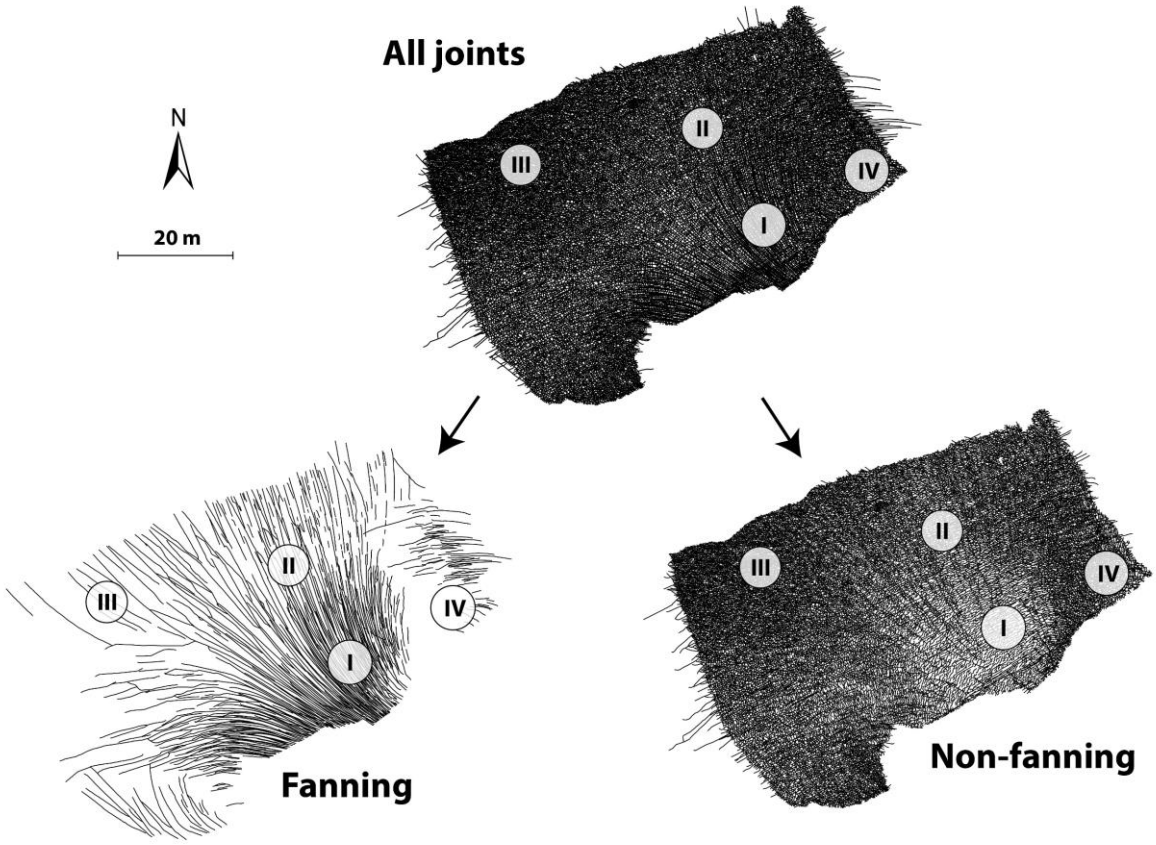


**Figure 4.5:** Trace map of all the joints, and the division of the two main groups, fanning and non-fanning joint traces. The circular window sampling regions are chosen based on their location relative to the set of fanning joints.

### 4.2.2 Identifying other joint sets

The non-fanning joints were divided into sets defined as specific intervals of orientation and length. In order to identify length and strike cut-offs to separate different populations of joint traces, an iterative process based on strike trends, length characteristics and topological properties (i.e. abutting relationships) was used. These criteria were assessed in four ways:

***1) Rose diagrams and cumulative frequency plots***

The strike of the joint traces is one of the main features that can be used to assign set boundaries (Derschowitz & Einstein, 1988). Rose diagrams with and without weighting based on trace length prove to be useful in the detection of joint sets (Welch *et al.*, 2015). Because the number of joints in the data set is high, the bin size in the rose diagrams can be narrow, and still contain enough samples to identify well-defined peaks (Fig. 4.6 a and b). Cumulative frequency plots (Fig. 4.6 c), where the cumulative frequency is plotted against the strike, show the same trends as the rose diagrams.

Rose diagrams and cumulative frequency plots were made for different length ranges of the joints. Each set is then visible over a certain scale range, and constitutes a peak sector in the rose diagram, and a change of slope in the cumulative frequency plot. This aids the identification of both strike- and length cut-off values for the joint sets.

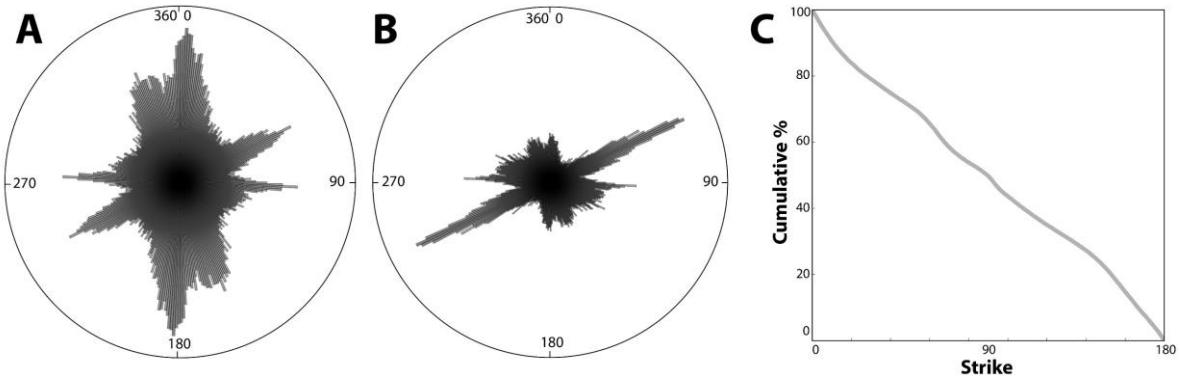


**Figure 4.6**: Rose diagrams for the non-fanning joints, with 1º bin size. **a**) Not weighted for trace length. **b**) Weighted for trace length. **c**) Cumulative frequency plot of the non-fanning joints, where change in slope represents the strike trends which appear as peak sector in the rose diagrams.

### *2) Orientation vs length scatter plots*

When the strike of each joint is plotted against the length in a scatter plot, each joint set represents a cluster of data points. In order to visualize the clustering of data points in the plot, the point density is contoured, highlighting the areas with a high density of data points.

### *3) Length-frequency distribution plots*

As joint sets can be characterized by different, systematic scaling distributions (Odling, 1997), scaling properties are used to identify set boundaries. Joint traces from the whole network and for restricted length-strike regions were plotted as data points in cumulative diagrams, in order to identify length intervals with consistent distributions. Notably, three plot types were used to identify length intervals with consistent length distributions; negative exponential plots (length vs log of cumulative percentage, Fig. 4.7 a), power-law plots (log of length vs log of cumulative percentage, Fig. 4.7 b) and log-normal plots (log of length vs standard deviations, Fig. 4.7 c). On these plots, the straight line segments correspond to joint sets and their length scaling distribution, whereas the kinks correspond to likely break values between different sets (Gillespie *et al.*, 1993; Bonnet *et al.*, 2001).

Identifying the lengths where the slope of a scaling plot changes, aids the identification of joint sets. In addition, the straight lines on each of the plots provide information about the length distribution of the final joint sets.

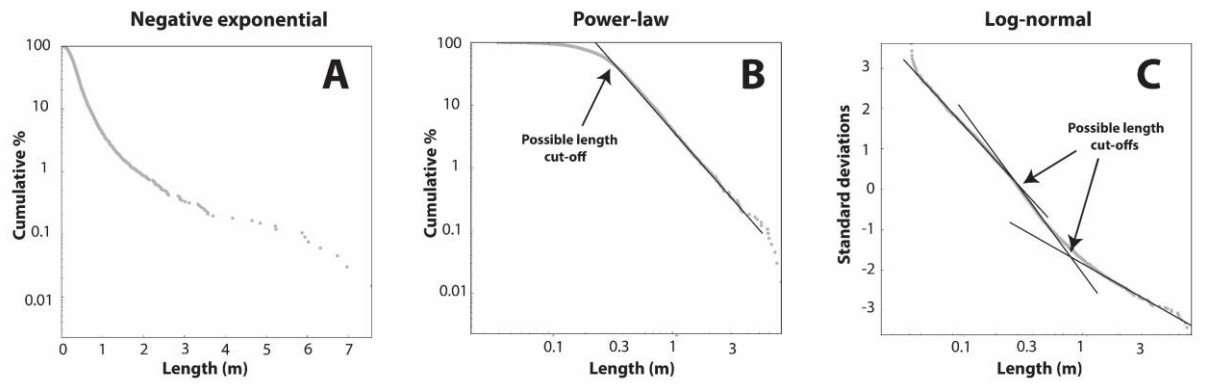


**Figure 4.7**: Cumulative length distribution for an arbitrary strike interval. **a**) Negative exponential. **b**) Power-law. **c**) Log-normal distributions.

#### *4) Visual inspection of abutting relationships*

The final criterion used in the identification of joint sets is visual interpretation of abutting relationships. Abutting relationships provide information about the chronology of structure formation (Hancock, 1985; Peacock, 2001; Peacock *et al.*, 2018) and may therefore aid the assignment of length cut-offs and strike cut-offs between the joint sets. Joints that abut the same structures show genetic similarities (Engelder & Gross, 1993), and are therefore likely to belong to the same set. Though no thorough node counting was performed at this stage of the analysis, a visual interpretation was considered for the final set division.

Assigning the boundaries between the sets was an iterative process (Fig. 4.8). Each iteration included the identification of a proposed set based on a peak from the rose diagram plot, and areas with high densities of data points in the length-orientation scatter plot. The length scaling analysis for the selected strike interval would then suggest length cut-off values, implied by changes in slope in the length distribution plot. A visual inspection of the network would then be performed, analyzing topological similarities, i.e. abutting relations, of the selected joint traces.

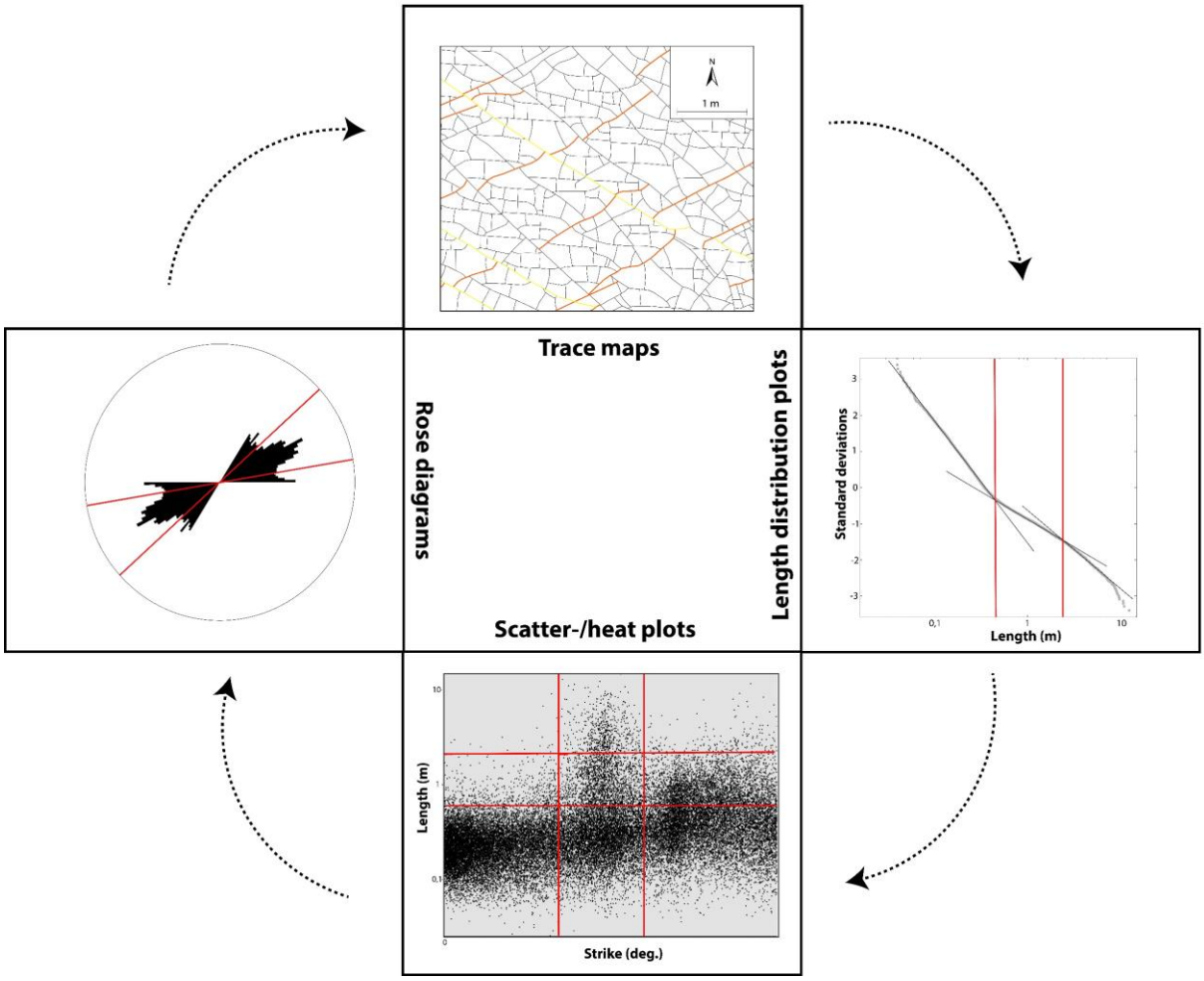


**Figure 4.8:** The process of assigning the final set boundaries consisted of multiple iterations of assessing methods to detect similar orientation, length and topological properties.

After several iterations through the above-mentioned steps, the final set boundaries (i.e. length- and strike cut-offs) were assigned, and the group of non-fanning joints were categorized into sets.

## 4.3 Joint set chronology

### 4.3.1 Node counting and chronology

All the abutting nodes (Y-nodes) between each two joint sets were identified, and the number of abutting relationships were counted in each of the window sampling regions (Fig. 4.5), in order to assess the relative chronology of joint set formation (Peacock *et al.*, 2018). Fig. 4.9 exemplifies the identification of the abutting nodes between two generic joint sets, α and β, within an interpretation region.

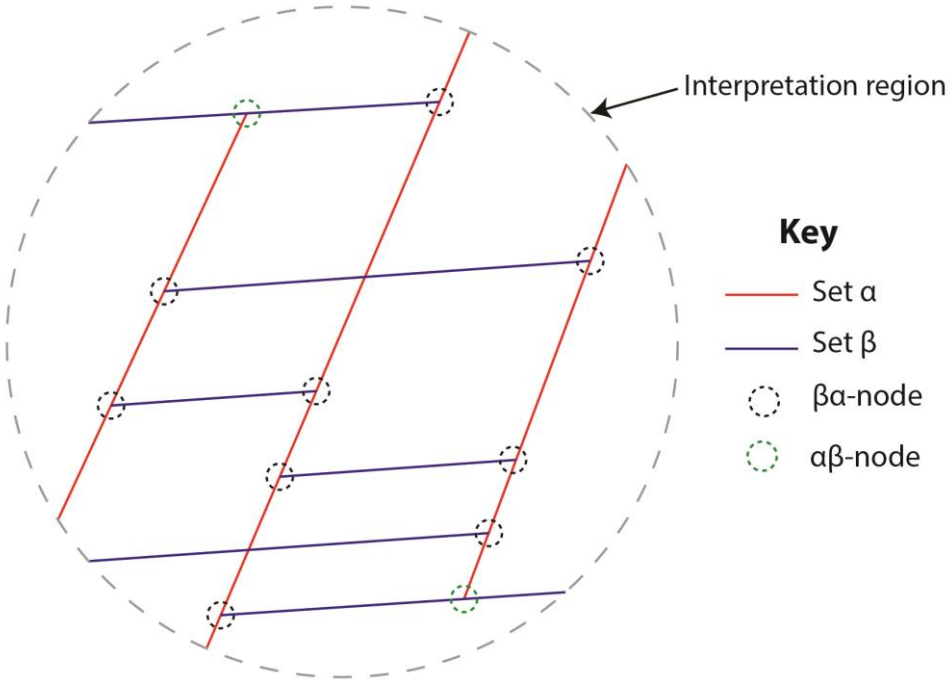


**Figure 4.9**: Example of node counting between two joint sets, α and β. The abutting nodes are referred to as αβ-nodes or βα-nodes.

Table 4.1 shows the result of a node counting between two generic joint sets, α and β, where $x_{\beta\alpha}$ denotes the number of nodes where β-joints abut α-joints and $x_{\alpha\beta}$ denotes the number of nodes where α -joints abut β-joints.

**Table 4.1**: Schematic node table, showing how many times *n* joint sets abut each other. Each entry denotes how many times the set of the row abuts the set of the column (i.e. $x_{\alpha\beta}$ denotes the number of times set α abuts set β, whereas $x_{\beta\alpha}$ denotes the number of times set β abuts set α).

| | **Set α** | **Set β** | **…** | ***n*** |
|---|---|---|---|---|
| **Set α** | | $x_{\alpha\beta}$ | | $x_{\alpha n}$ |
| **Set β** | $x_{\beta\alpha}$ | | | $x_{\beta n}$ |
| **…** | | | | |
| ***n*** | $x_{n\alpha}$ | $x_{n\beta}$ | | |

Node counting in each of the areas results in square tables with the number of columns and rows corresponding to the number of joint sets identified. The window sampling regions that yield consistent node counting tables are used to determine the age relationships between the joint sets, based on the principle that younger joints have the tendency to abut older joints (Peacock *et al.*, 2018). The node tables from the chosen areas are stacked, combining the number of relationships in each area, to interpret the chronology.

The rows and columns of the table with stacked node counting values were reorganized using standard matrix operations, such that for any two corresponding entries $x_{\beta\alpha} > x_{\alpha\beta}$. Accordingly, α, β … *n*, is the expected relative chronology of the joint sets. The ratio between each ordered pair of corresponding entries (e.g. $x_{\beta\alpha}$ and $x_{\alpha\beta}$) represents the degree of "backcycling", as discussed by Procter & Sanderson (2018).

### 4.3.2 Quantification of chronological uncertainty

The uncertainty (i.e. the probability that two joint sets developed at the same time or in the other order than the one suggested by the set of node values) depends on both the value of $(x_{\alpha\beta} + x_{\beta\alpha})$ and the value of $(\frac{x_{\beta\alpha}}{x_{\alpha\beta}+x_{\beta\alpha}})$. Based on e.g. Peacock *et al.* (2018), I assume that;

$$\lim_{\substack{(x_{\alpha\beta}+x_{\beta\alpha})\to\infty \\ x_{\beta\alpha}/(x_{\beta\alpha}+x_{\alpha\beta})\to 1}} P(\alpha \; is \; older \; than \; \beta) = 1 \qquad \textbf{Equation 4.1}$$

i.e. there is increasing certainty about the chronology, the more data are available. The uncertainty of a chronological assumption can be quantified given a set of values (e.g. $x_{\beta\alpha}$ and $x_{\alpha\beta}$) and expressed with statistical *p*-value testing.

I assign a null hypothesis ($H_0$) that the sets have the same age, and an alternative hypothesis ($H_a$) that set α is older than set β. If $H_0$ is true, I expect the probability that any given node is one where α abuts β, to be 0.5. If $H_0$ is true, the probability of obtaining the result at least as skew as $(x_{\alpha\beta}, x_{\beta\alpha})$ corresponds to the *p*-value, which can be expressed;

$$p\text{-value} = \sum_{n=0}^{x_{\alpha\beta}} \binom{(x_{\alpha\beta}+x_{\beta\alpha})}{n} 0.5^{(x_{\alpha\beta}+x_{\beta\alpha})} \qquad \textbf{Equation 4.2}$$

## 4.4 Analysis of spatio-temporal development

### 4.4.1 Development analysis

Trace maps for each time "step" (i.e. the whole network after the formation of each new joint set) were produced, in order to quantify and illustrate the development of the joint network (Fig. 4.10). The development of network properties can then, based on the inferred chronology from abutting relationships, be plotted in diagrams as time series. Such temporal analyses were performed for the entire study area, as well as for the window regions (Fig. 4.5), illustrating spatial heterogeneity in the development of various network properties. The spatial distribution of each of the joint set (i.e. not including the older ones) was also analyzed.

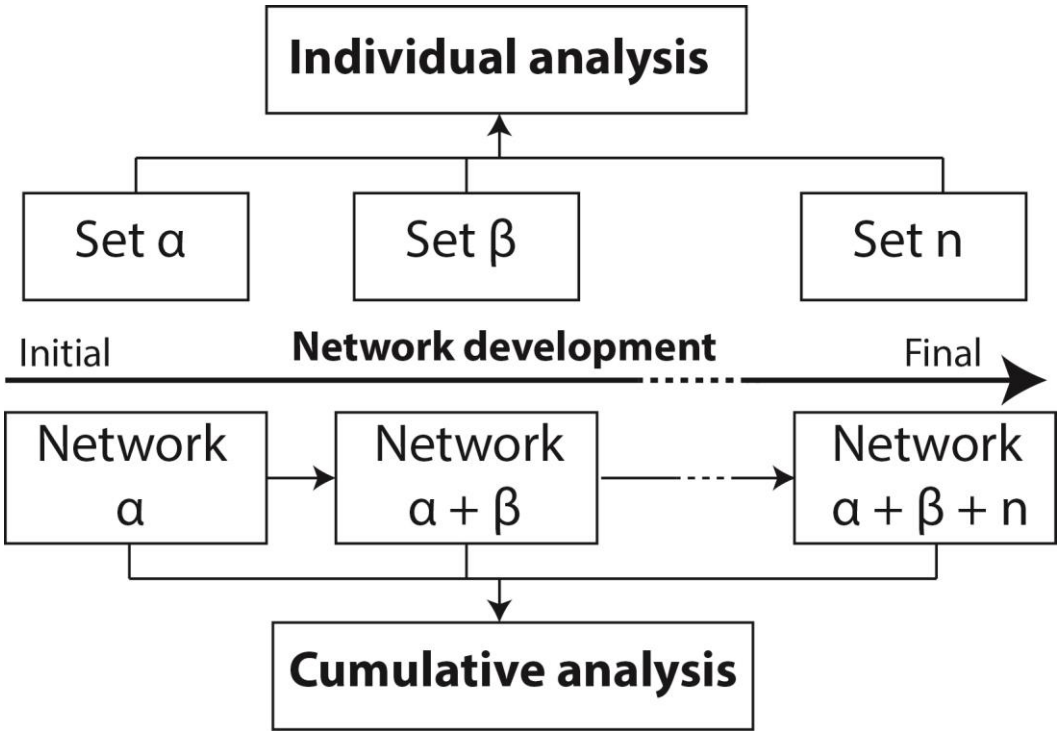


**Figure 4.10**: Workflow for the spatio-temporal analysis, given *n* sets with a known relative chronology.

### 4.4.2 Analysis regions

In order to illustrate the spatial variability in the evolution of network properties, areas with different sizes were analyzed:

1) ***Whole digitalization area***. In order to quantify the development of network properties for the entire network, analyses were performed on the whole of the digitization area. For the different steps of the analysis, the area at 3 244 $m^2$ was used for normalization.
2) ***Window areas***. To quantify the variation in network properties as a result of location within the fan structure, the circular window sampling areas (Fig. 4.5) were analyzed with respect to development of network properties. The radii of these window regions are 5 m, so the area of 78.5 $m^2$ is used as normalization area in the analysis.
3) ***Network grid***. A network grid with cell size 1 $m^2$ was used to map spatial variations of network properties. Each grid cell displays the properties of the area around it, and a search radius of 2.5 m was assigned. Each grid cell is normalized for the area inside the circular search radius (19.6 $m^2$; Fig. 4.11).

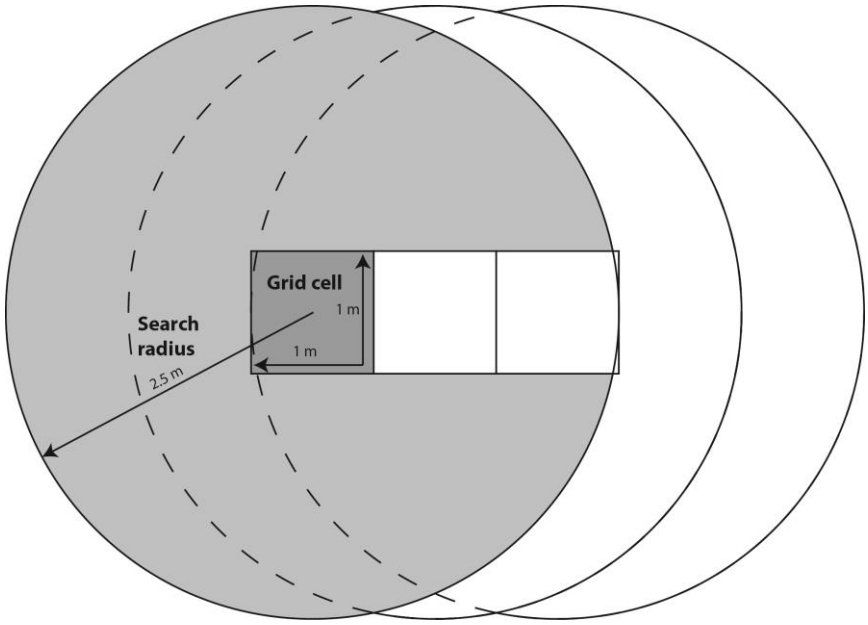


**Figure 4.11:** Spatial heterogeneities in network properties was mapped on a grid with cell size 1 $m^2$. Each grid cell reflects the properties within the search radius of 2.5 m.

### 4.4.3 Joint intensity

Intensity analyses were performed for the analysis regions of different sizes. The 2D intensity (*I*) measures the total trace length (*l*) within an area (*A*), and can be calculated as

$$I = \frac{\sum l}{A} \qquad \textbf{Equation 4.3}$$

The intensity analysis was performed both for the individual sets and the cumulative network stages (Fig. 4.10), in order to illustrate the development and to detect spatial heterogeneities.

### 4.4.4 Topological measures of connectivity

Various topological analyses were performed on the trace maps during different stages of development (i.e. the "cumulative networks", Fig. 4.10).

NetworkGT provides a means to automatically detect the nodes, and classify them as I, Y or X, allowing for a visualization of the spatial variability of node frequency for the different node types (Nyberg *et al.*, 2018). Where $N_I$, $N_Y$ and $N_X$ are the number of I-nodes, Y-nodes and X-nodes (respectively) within an area, the node frequencies can be obtained by dividing the numbers by the area, yielding the node frequencies with the unit $m^{-2}$. As Y- and X nodes are characterized as connecting nodes, the connecting node frequency can be calculated as

$$\text{Conncting node frequency} = \frac{N_Y + N_X}{A} \qquad \textbf{Equation 4.4}$$

providing a measure of network connectivity (Sanderson & Nixon, 2018). The average node degree, i.e. the average number of connections per node can be calculated as

$$\text{Average node degree} = \frac{N_I + 3N_Y + 4N_X}{N_I + N_Y + N_X} \qquad \textbf{Equation 4.5}$$

and provides a measure of the connectedness of the network. Likewise, the proportion of I-nodes ($P_I$) can be calculated as

$$P_I = \frac{N_I}{N_I + N_Y + N_X} \qquad \textbf{Equation 4.6}$$

and similarly for the other node types. Based on this, the node proportions for different stages of network development can be plotted in a ternary diagram. The same can be done for the proportion of branch types, i.e. II-branches, IC-branches and CC-branches. If $N_{II}$, $N_{IC}$ and $N_{CC}$ denotes the numbers of II-, IC and CC branches, respectively, the proportion ($P_{II}$) can be calculated as

$$P_{II} = \frac{N_{II}}{N_{II} + N_{IC} + N_{CC}} \qquad \textbf{Equation 4.7}$$

for the I-I branches, and similarly for the other branch types within an area. The development of branch characteristics is also indicative of network connectivity (Sanderson & Nixon, 2015).

### 4.4.5 Block development

Another aspect of network development is the way progressive jointing leads to formation of blocks, with each "step" of network formation, i.e. the cumulative analysis (Fig. 4.10; Nyberg *et al.*, 2018). The style of block break-up is hard to quantify, and the analysis of this aspect is largely confined to qualitative analysis of block break up styles in different parts of the network. Various block properties can, however, be quantified with topological measures, based on the numbers of branches, nodes and clusters. For a defined search area, the number of blocks can be calculated as the sum of whole blocks and half the half blocks, where each half block counts as ½. This allows for a calculation of the number of blocks and mean block size within an interpretation region (Nyberg *et al.*, 2018).

## 4.5 Sources of error

### 4.5.1 Limitations in network digitization

Even though the fracture network at Lilstock Beach is a good exposed example of a polyphase joint network and UAV imagery generally yields high resolution, a joint trace map resulting

from digitalization is not an absolutely precise rendering of the actual joint network (Andrews *et al*., 2019). The resolution of the UAV imagery is a limitation, and joints which have an aperture below the spatial resolution of the imagery will not be detected. If certain sets of joints have smaller apertures than others, these sets will have a larger probability of being overlooked, which may result in undersampling. Likewise, joints which are short (<5 cm) are more likely to be undersampled. Because the studied exposure is situated in the tidal zone, erosion may have played a role in shaping the outcrop. The joints that trend perpendicular to the coastline will experience wave erosion in the length direction. Because water runoff is controlled by topography, the joints that trend down-dip are prone to a higher degree of weathering than the others. These two effects may result in a relative undersampling of the joint populations that trend parallel to the coastline.

Andrews *et al.* (2019) show that fracture interpretation can be subjective. Certain joint styles are particularly difficult to digitize correctly. When joints intersect on low angles it is hard to determine which joint abuts the other. Furthermore, it is difficult to distinguish between joint traces and minor fault zones on UAV imagery, which introduces subjectiveness in the characterization of the fracture types. Digitization of the entire fracture trace map by one person does not eliminate the subjectiveness but is believed to make the subjevtiveness consistent.

Another possible limitation of the joint trace map is the size of the digitized area. For example Engelder & Peacock (2001) and Procter & Sanderson (2018) demonstrate that the jointing style in the Lilstock area displays high spatial variability, and a larger area of digitalization could therefore have detected a higher number of joint sets. The trace map is still, however, comprehensive enough to detect local joint sets, and allows for a quantification of various network properties in the proximity of the fault zone.

Despite the potential for subjective bias and other limitations of the data set, the joint trace map is more extensive than the ones made in the context of previous studies in the same area (e.g. by Loosveld & Franssen, 1991; Rawnsley *et al.*, 1998; Engelder & Peacock, 2001). Because the number of joint traces in the digitized area is high (>50 000), the relative source of error posed by misinterpretation is believed to be low.

### 4.5.2 Sources of error in identification and division of joint sets

The process of categorizing each joint as either fanning or non-fanning is susceptible to subjective bias. Even though the existence of the fan is undebatable, the characterization of

each joint is qualitative, based on the strike of each joint and the local orientation of the joint fan. Misinterpretations in this process may result in errors in the length-distribution analysis.

The process of dividing the non-fanning joint traces into different sets consists of many steps that are susceptible to uncertainty. The study by Engelder & Peacock (2001), performed in the same area, recognizes the possible subjective aspect of assigning set boundaries, and acknowledges the fact that overlapping clusters of data points in the stereo-net and orientation vs length scatter plots exist. If we think of joint set formation as a consequence of discrete episodes of stress, the distribution of strike and length of the joints within a set can be compared to a stochastic process (Whitaker & Engelder, 2005). The probability distribution of data points ($x$) for a single joint set can then, if we assume a normal distribution in strike and length, be expressed as

$$f(x|\mu,\sigma^2) = \frac{1}{\sigma\sqrt{2\pi}} e^{-\frac{(x-\mu)^2}{2\sigma^2}} \qquad \textbf{Equation 4.8}$$

where μ is the mean, σ is the standard deviation, and $\sigma^2$ is the variance (Moore & McCabe, 2005, pp. 71). Normal distribution of strike and length will result in rounded "clouds" of points in a strike vs length scatter plot (Fig. 4.12 a), whereas other length distributions will result in elongated clusters of data points if plotted in the same diagram.

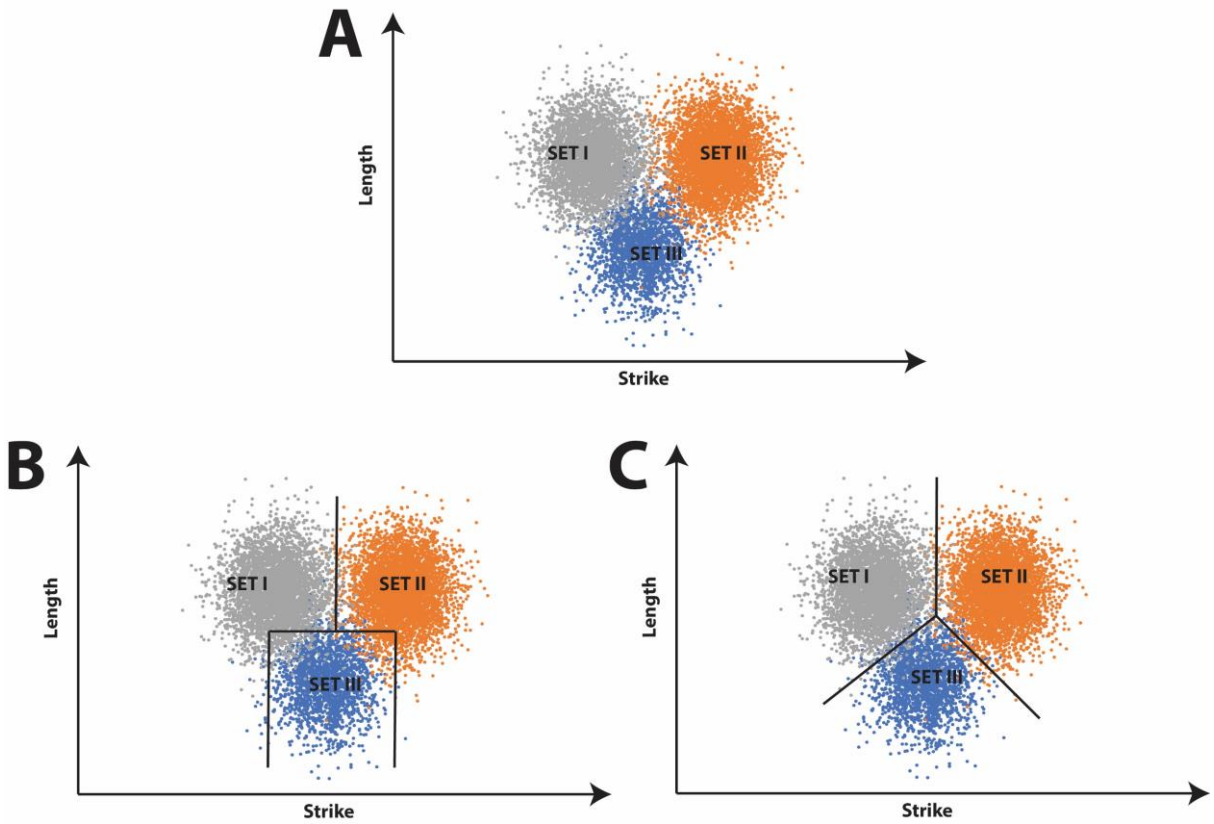

**Figure 4.12**: **a**) Example of three stochastic processes which may resemble joint set formation, each represented as 1000 data points. The strike and length of each set are normally distributed (based on arbitrary values of μ and σ). **b**) Best fit length and strike cut-off values for the tree populations will categorize numerous data points in the wrong group. **c**) Best fit oblique set boundaries will still categorize data points in the wrong set, because the "clouds" of data points overlap.

Categorizing joints into the wrong set, which inevitably happens to some extent (Fig. 4.12 b and c) due to overlapping length and strike intervals, results in less concise results in the chronology analysis, and may disturb the length distribution analysis. In the final set division, certain set boundaries can be classified as more certain than others. In general, the strike boundaries are associated with higher certainty, as the trend in strike is easier to detect (on rose diagrams and cumulative strike diagrams), than the length cut-off values.

# 5. Results

This chapter summarizes observation from field work, and key results from the spatio-temporal network analysis of UAV imagery.

## 5.1 The geology of the study area

### 5.1.1 Bedding attitude

The study area consists of a well exposed wave-cut platform, with extensive outcrops of several limestone beds interbedded with shales. The stratigraphic log reveals that the sequence consists of ~80% shale and ~20% limestone (Appendix I). The layers in the area are sub-horizontal, very gently folded and cut by faults at various places. The studied limestone bedding plane (bed 109, as described by Whittaker and Palmer, 1983) is the most extensively exposed bedding surface in the study area, at about 12.000 $m^2$. Loosveld & Franssen (1992) and Engelder & Peacock (2001) refer to this particular exposure to as "The Bench", and the same name is used here. Multiple measurements show that the limestone bed which constitutes the Bench has a consistent thickness, at ~17 cm. In the studied area, the bedding surface constitutes an open anticline, with an interlimb angle of ~175$^o$. The hinge line of this anticline plunges shallowly towards NE, at ~2$^o$ (Fig. 5.1).

### 5.1.2 Structural overview

The stratigraphy is offset by a north-down-throwing normal fault (~60$^o$ dip) that can be traced for ~450 m through the studied area. This fault is referred to as "Fault 5" by Rawnsley *et al.* (1998) and Engelder & Peacock (2001), and has a change in trend from ~E-W, in the western area, to ~ENE-WSW in the eastern area. The Bench is juxtaposed against bed 85, suggesting a stratigraphic separation of ~15 m (Fig. 5.1). The fault core of the main fault ranges between 0.5 and 1.5 m in thickness. This main fault is surrounded by smaller faults, which can be observed both in the field and on drone imagery. Two faults, trending ~E-W, abut the main fault in the eastern part of the area, in the footwall of the main fault. Other faults, with offsets on the cm-scale, are particularly abundant in the area where these two minor fault traces splay from the main fault. Some of the minor faults that strike parallel to the main fault are synthetic to it and others are antithetic. Many of the minor faults have red/brown secondary minerals along the fault planes. The Bench is situated in the hanging wall of the main fault, north and west of the fault trace, in the fault block referred to as "Block 5" by Rawnsley *et al.* (1998) and Engelder & Peacock (2001). Locally, the limestone beds in the hanging wall show normal fault drag

near Fault 5, forming a hanging wall syncline along the trace of the main fault. In the studied area, however, there is little or no normal fault drag.

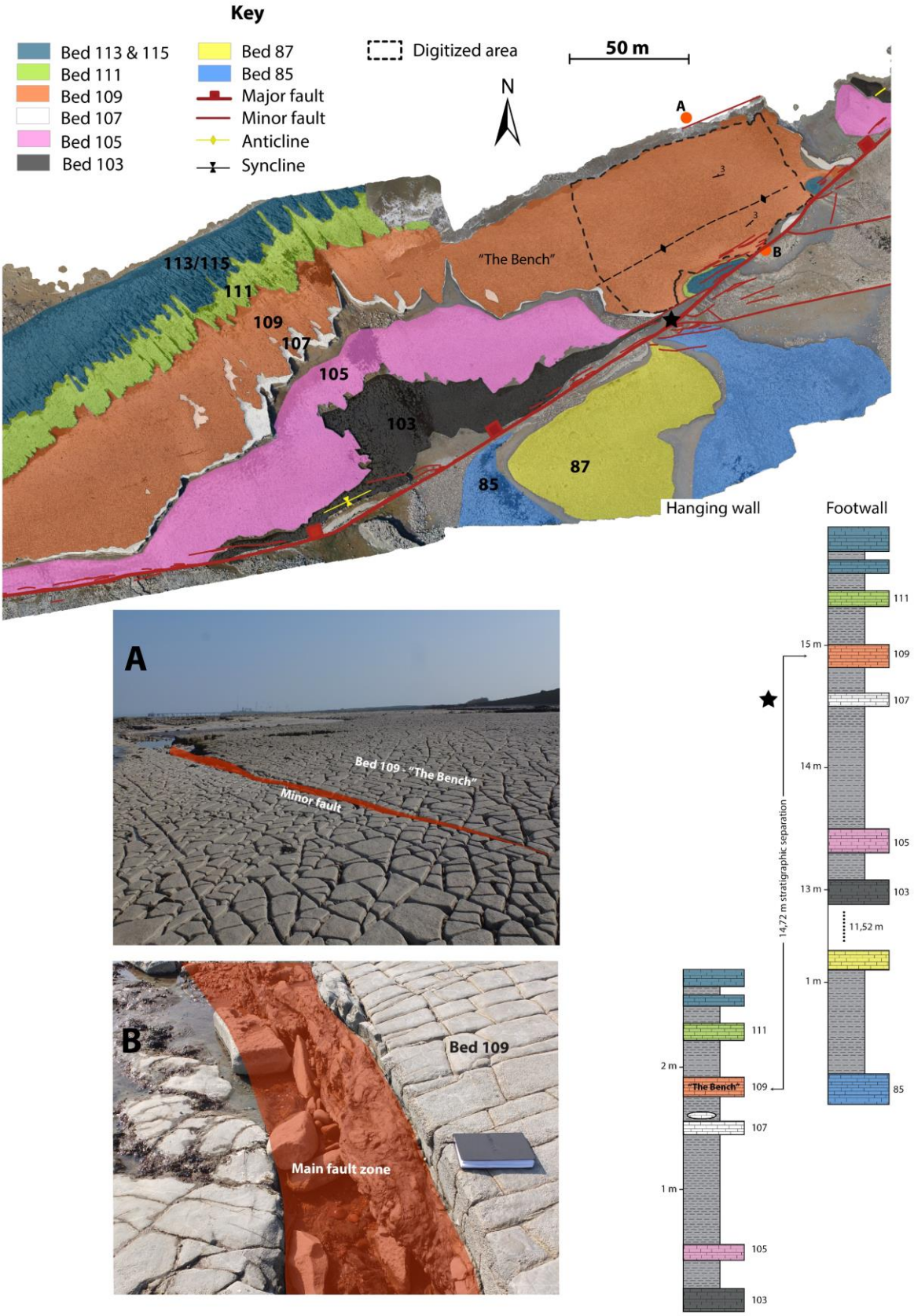

**Figure 5.1**: Structural and stratigraphic map of the field area. The orange dots indicate the locations where the field photographs (**a** and **b**) are taken. The black star indicates the location where the stratigraphic separation is measured. The main study area, where the joint analysis is performed, is marked with a dashed line. The stratigraphic log shows the stratigraphic separation between the footwall and the hanging wall of the main fault, and the bed numbers refer to Whittaker and Green (1983). **a**) Looking east, shows a minor fault with displacement on the dm scale. **b**) Looking west, shows the fault core of the main fault.

The Bench contains one set of calcite veins trending ~ENE-WSW, sub-parallel to the fault trace and the hinge line of the hanging-wall anticline. These veins are approximately perpendicular to the bedding surface (Fig. 5.2 a). The veins are particularly abundant around the minor faults and in the hinge area of the fold, but appear throughout the extent of the study area, with spacing on the decimeter to the meter scale.

Another set of veins, trending E-W, occur on the Bench, intersecting the bedding surface perpendicularly. These veins have spacing on the millimeter to the centimeter scale and are classified as HDVs (Rawnsley *et al.*, 1998). In most cases, this set of veins is only visible along the edges of joints, where weathering has enhanced the contrast between the HDVs and the limestone beds (Fig. 5.2 b).

All of the limestone beds contain polydisperse joint networks, which are mainly bed-bound, although some longer joints can be traced in the neighboring limestone beds (Fig. 5.2 c). Some of the joints are apparently more eroded than others, with the apertures of the joints ranging between about 1 mm and 2 cm (Fig. 5.2 d). One set of joints in the studied layer reactivate the set of veins that is parallel to the fault trace, i.e. trending ~ENE-WSW.

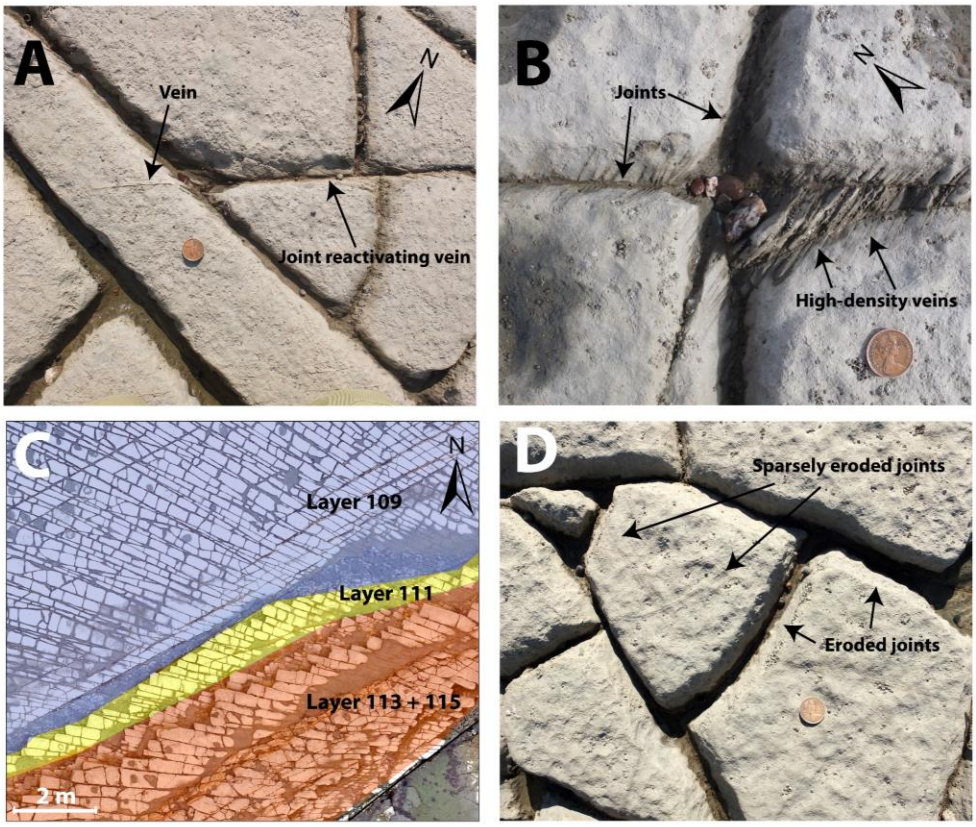


**Figure 5.2:** Characteristics of joints and veins in the study area. **a)** Joints reactivating the set of veins parallel to the fault main. **b**) Array HDVs, visible along weathered joint edges. **c)** Drone image; a few joints can be traced in adjacent limestone beds. The dominating joint orientation is similar in the exposed beds. **d)** Different joint sets on the Bench where some of the joints are significantly more eroded than others.

In proximity of the main fault, one set of joints deflects and converges towards certain areas along the main fault trace. At these places, the joint traces curve towards the fault plane and intersect it perpendicularly. At least three areas of joint convergence can be observed on the Bench, creating three fan-like structures. One fan of joints dominates the studied area, which also covers the interference zones with the two neighboring fans (Fig. 5.3).

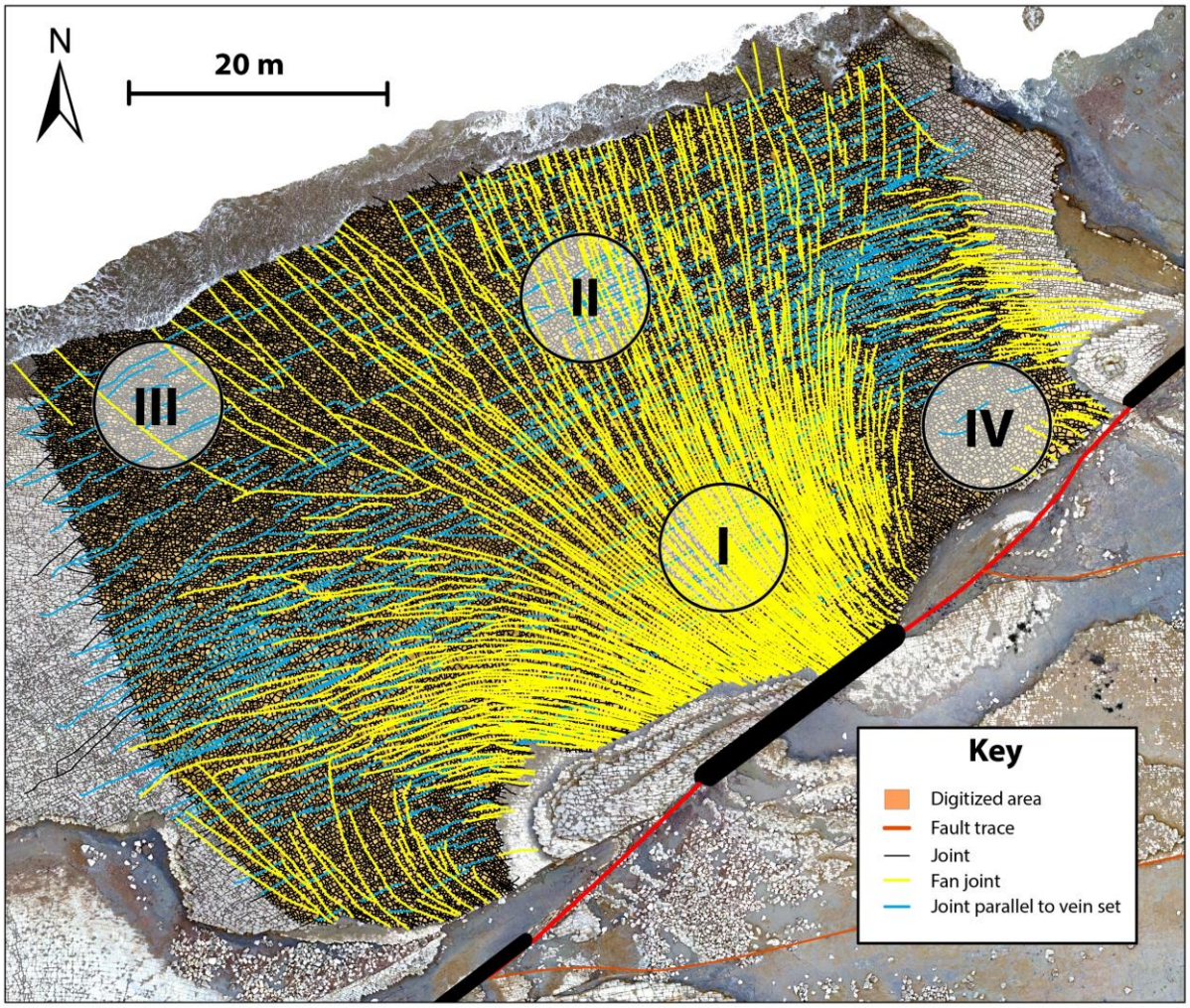


**Figure 5.3**: One fan structure and parts of two neighboring ones occur within the studied section of the Bench. These, and the set of joints which follows the set of veins, are highlighted. The black bars indicate the segments against which the fanning joints converge.

In addition to the curved set of joints, and the ones that have reactivated veins, the bed is pervasively jointed by numerous sets of joints. The rest of this chapter focuses on these joint sets, their chronology and the evolution of network properties.

## 5.2 Joint sets

### 5.2.1 Orientation- and length characteristics of the main sets

In total, the area of digitalization contains 52 850 individual joint traces, with some extending outside the area. 701 of these joint traces belong to the fan structures; 23 in the westernmost fan, 697 in the central fan, and 74 in the easternmost fan. These joints, which are here referred to as the fan-joints, are characterized by being long, with the longest traces exceeding 40 m, as well as being curved. Many of these joint traces extend outside the digitizing area and intersect

the boundary of the exposure. The set of fan-joints was excluded from the rest of the orientation-length analysis, as the strike of this set varies significantly (Fig. 5.4).

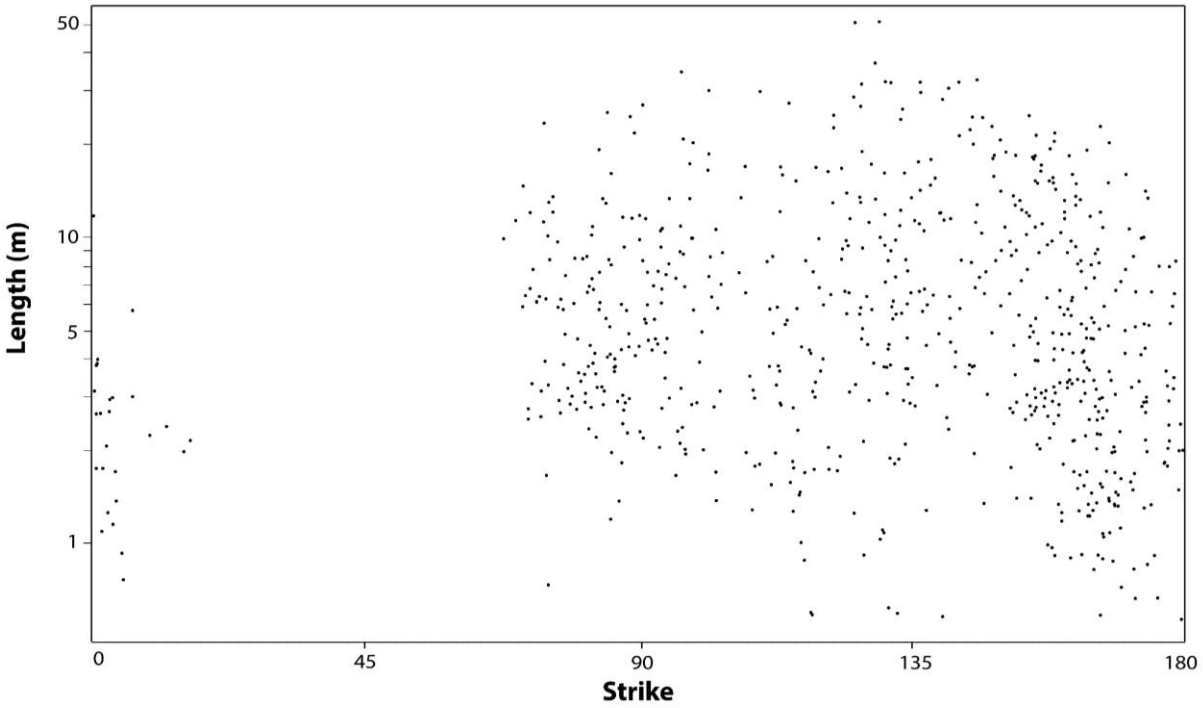


**Figure 5.4**: Length-orientation distribution of the fan-joints ($n$ = 701), which show a range of strike of ~140°.

The 52 149 non-fanning joints can be grouped into three overall set groups, based primarily on length characteristics; A-sets, B-sets and C-sets. This grouping is the basis for further subdivision.

***A-sets***

The A-sets is the longest group of sets, and have characteristic lengths >1 m, with the longest joints in this set exceeding 10 m. Three different A-set orientations can be identified visually on drone images and in the field, as they stand out from the joint trace map and the outcrop because of their length and straightness. The most dominating among the A-joints is the set of joints that follow the ~060° striking veins.

***B-sets***

The B-sets have characteristic lengths around 1 m. Prevailing strike directions within the B-set group are not as easy to identify visually on drone images or in the field as the A-sets, but appear on the rose diagram plots and on cumulative strike distribution plots (Fig. 5.5).

***C-sets***

The C-sets are the shortest of the joint sets, with characteristic lengths ranging from 25 to 50 cm. Due to their shortness, prevailing strike directions among the C-joints are not as visually

striking as for the other two set groups. Their prevailing strike directions do, however, dominate the rose diagram plots and the cumulative strike distribution plots (Fig. 5.5), as C-joints dominate number-vise (Table 5.1). The C-joint traces are characterized by higher relative curvature than the other joint sets.

### 5.2.2 Subdivision of the main set groups

Rose diagram plots and cumulative frequency plots show different prevailing strike values for different length intervals (Fig. 5.5).

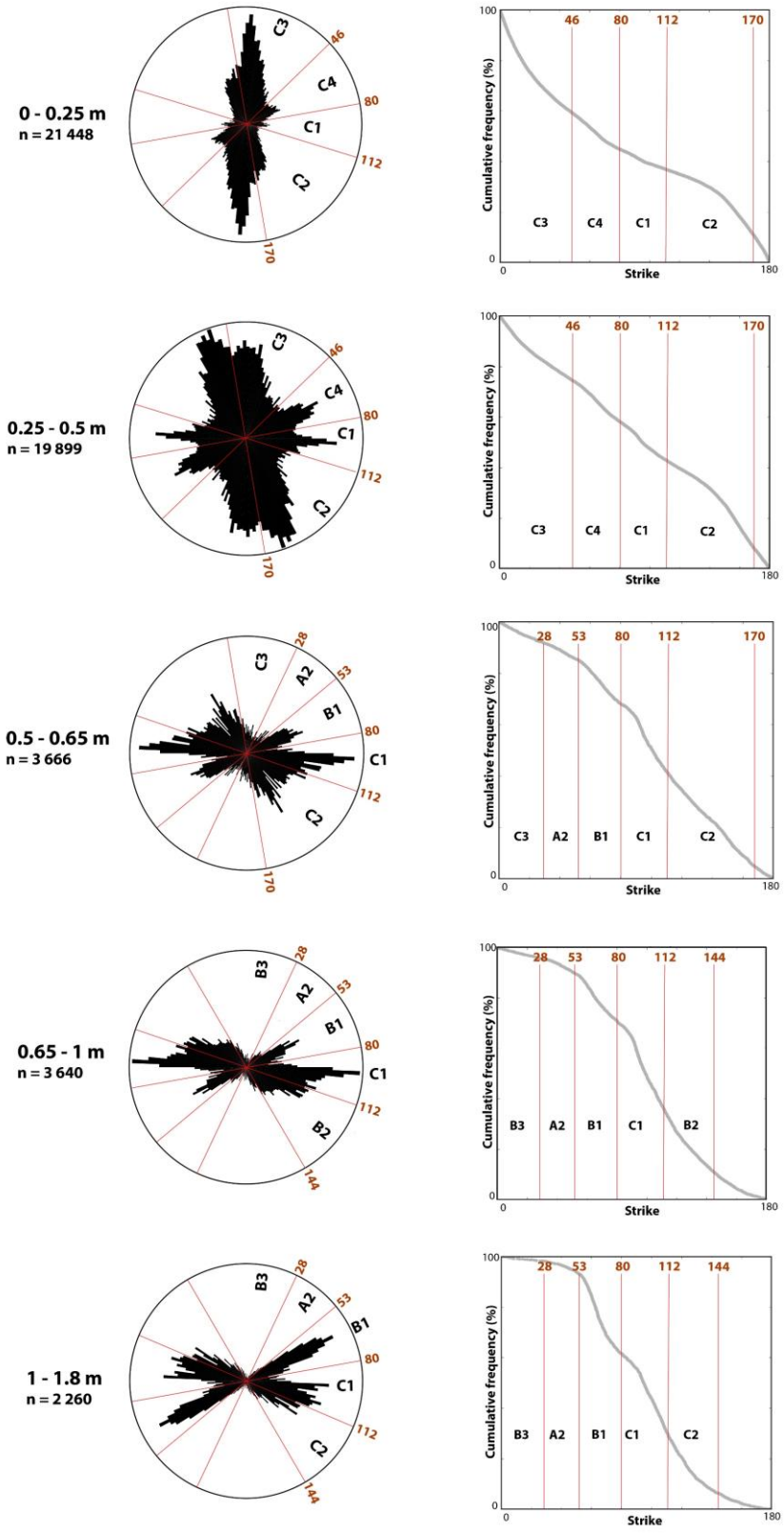


**Figure 5.5**: Corresponding rose diagram plots and cumulative strike distribution plots for joint traces grouped in different length bins. For each length bin, there are different prevailing strike directions, creating a basis for the sub-division of the set groups.

The A-set group consists of three sub-sets, A1, A2 and A3. Notably, A1 is parallel to the set of veins. The B-set group is subdivided into three sub-sets, whereas the C-set group is divided into four sub-sets based on orientation. The C-sets are by far the most numerous, and thus dominate on the scatter plot and on the contour plot (Fig. 5.6).

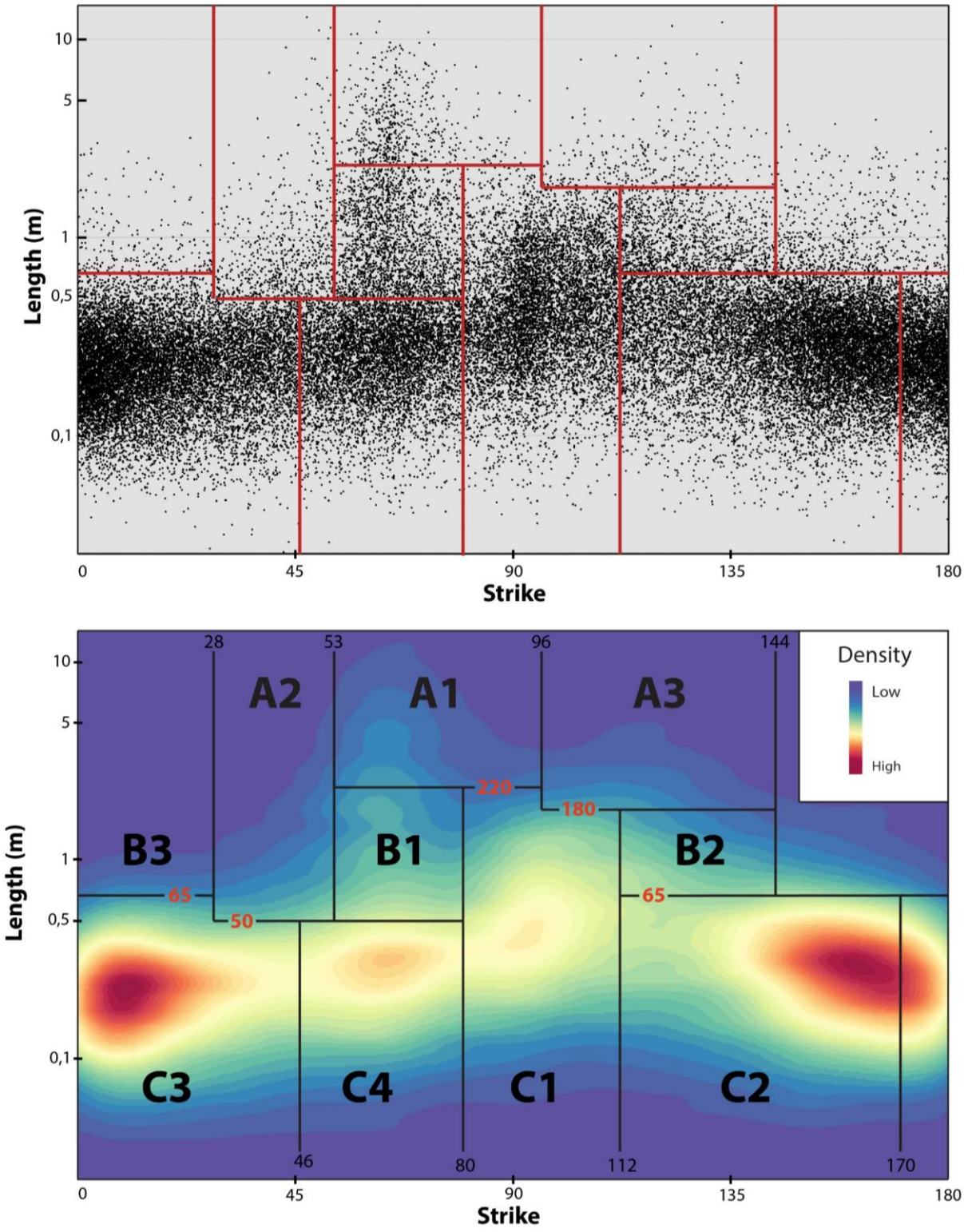

**Figure 5.6**: **a**) Length vs orientation scatter plot of the non-fanning joints ($n$ = 52 149). For some of the sets, one can see the elevated density of points in a certain area. **b**) Contour plot displaying the density of data points from Fig. 5.6 a. The C-sets are represented as the areas with the highest densities. The boundary between sets C2 and C3 seems arbitrary due to the cut-off in the diagram, but is shown to represent an actual strike cut-off (Fig. 5.5).

There are different numbers of joints in the 11 sets. There is a tendency for the B-sets to be more numerous than the A-sets, and the C-sets are more numerous than the B-sets by about one order of magnitude (Table 5.1).

**Table 5.1**: The number of data points (joint traces) in each of the 11 sets, and their characteristic lengths and trends. The coefficient variance (CV) refers to the length distribution.

| Sub-set | *n* | | Mean length (m) | Total length (m) | CV | Mean trend |
|---|---|---|---|---|---|---|
| **FAN** | 701 | | 7.05 | 4 942.1 | 0.98 | 155.2 |
| **A1** | 595 | A-joints: $n$ = 1 593 | 3.86 | 2 296.7 | 0.46 | 66.0 |
| **A2** | 706 | | 1.09 | 769.5 | 1.12 | 42.8 |
| **A3** | 292 | | 2.77 | 808.8 | 0.48 | 117.9 |
| **B1** | 2 150 | B-joints: $n$ = 4 309 | 1.01 | 2 171.5 | 0.45 | 65.7 |
| **B2** | 1 354 | | 0.98 | 1 326.9 | 0.29 | 125.3 |
| **B3** | 805 | | 1.00 | 805.0 | 0.53 | 166.8 |
| **C1** | 8 006 | C-joints: $n$ = 46 247 | 0.51 | 4 083.1 | 0.68 | 107.7 |
| **C2** | 13 876 | | 0.30 | 4 162.8 | 0.45 | 147.2 |
| **C3** | 17 609 | | 0.24 | 4 226.2 | 0.46 | 12.9 |
| **C4** | 6 756 | | 0.26 | 1 756.6 | 0.41 | 62.7 |
| **Total** | 52 850 | | | 27 349.1 | | |

### 5.2.3 Length scaling properties of the joint sets

The joint sets display different length scaling distributions. The joints that belong to the fan-structure follow a negative exponential or log-normal length distribution. The A-sets are variable in terms of their scaling properties; set A1 follows an apparent negative exponential distribution, whereas A2 and A3 display power-law distributions, though with different scaling exponents. Sets B1 and B2 may follow negative exponential distributions but are difficult to interpret. Set B3, on the other hand, seems to follow a power-law distribution. The C-sets all seem to follow log-normal or negative exponential length distributions. In the distribution plots (Fig. 5.7), it is in many cases hard to distinguish between log-normal and negative exponential length distributions.

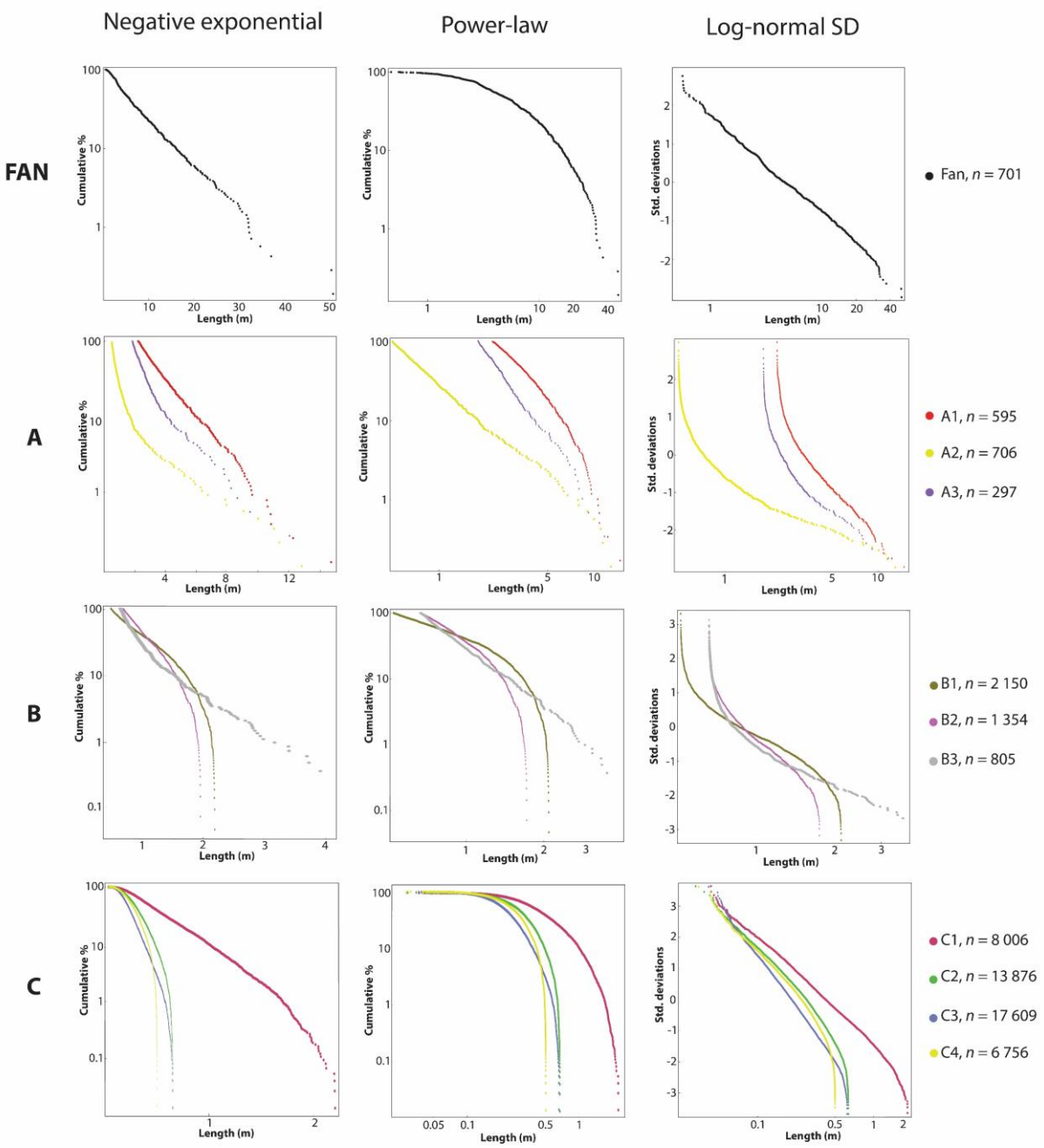


**Figure 5.7**: Cumulative frequency plots for the individual sub-sets, plotted in diagrams with negative exponential (length vs cumulative %), power-law (log length vs cumulative %) and log-normal (log length vs standard deviations).

## 5.3 Chronology

### 5.3.1 Node counting

The four window sampling regions (Fig. 5.3) contain a total of 7 689 Y-nodes. Areas I, II and III display particularly consistent abutting relationships, and were used in the node analysis to infer the chronology. Set groups A, B and C tend to abut the fan-joints. Likewise, the node

counting table (Table 5.2) shows that B- and C-joints tend to abut the A-joints, and that the C-joints tend to abut the B-joints.

**Table 5.2**: Node counting table for the A-, B- and C-joints, stacked from window sampling areas I, II and III. Fan-joints abut A-set joints 20 times, whereas A-set joints abut fan-joints 99 times etc.

| | **FAN** | **A** | **B** | **C** |
|---|---|---|---|---|
| **FAN** | | 20 | 5 | 9 |
| **A** | 99 | | 22 | 13 |
| **B** | 100 | 225 | | 45 |
| **C** | 991 | 1 209 | 1 076 | |

A similar node counting analysis for all the 11 sub-sets classifies 5 510 Y-nodes from regions I, II and III, stacked in Table 5.3. A full description of abutting relationships in the window sampling regions are given in Appendix II. The analysis shows that most of the pairs of sub-sets have significantly larger proportion of nodes abutting one way than the other, i.e. most entries $x_{\beta\alpha}$ are larger than their counterparts $x_{\beta\alpha}$.

**Table 5.3**: Values of node counting stacked from circle sample areas I, II and III. Fan-joints abut set A1 joints 14 times, whereas set A joints abut fan-joints 14 times etc.

| | **FAN** | **A1** | **A2** | **A3** | **B1** | **B2** | **B3** | **C1** | **C2** | **C3** | **C4** |
|---|---|---|---|---|---|---|---|---|---|---|---|
| **FAN** | | 14 | 1 | 5 | 4 | 0 | 1 | 4 | 1 | 2 | 2 |
| **A1** | 37 | | 0 | 6 | 0 | 9 | 3 | 1 | 2 | 4 | 0 |
| **A2** | 47 | 7 | | 9 | 0 | 5 | 2 | 4 | 0 | 1 | 0 |
| **A3** | 15 | 15 | 13 | | 0 | 2 | 1 | 0 | 0 | 1 | 0 |
| **B1** | 60 | 5 | 1 | 27 | | 22 | 5 | 9 | 5 | 5 | 0 |
| **B2** | 30 | 62 | 67 | 11 | 42 | | 2 | 9 | 3 | 3 | 2 |
| **B3** | 10 | 21 | 6 | 25 | 16 | 6 | | 5 | 0 | 1 | 3 |
| **C1** | 197 | 131 | 188 | 78 | 63 | 134 | 112 | | 112 | 234 | 8 |
| **C2** | 24 | 285 | 103 | 12 | 188 | 32 | 17 | 135 | | 42 | 56 |
| **C3** | 256 | 80 | 30 | 228 | 76 | 277 | 16 | 773 | 53 | | 25 |
| **C4** | 514 | 26 | 3 | 45 | 0 | 68 | 48 | 26 | 99 | 35 | |

### 5.3.2 Chronology sequence

The proportion between the corresponding node types (i.e. each coupled pair of entries $x_{\beta\alpha}$ and $x_{\alpha\beta}$) suggests that the fan-joints post-date the other set groups. Likewise, it is apparent that the C sets are younger than the B sets, which again are younger than the A-sets (Table 5.4).

**Table 5.4**: Values calculated from each coupled pair in Table 5.2. The lower left half of the table denotes the total number of nodes between each two sets (e.g. the total number of Y-nodes produced by fan joints and A joints is 119). The upper right half of the diagram shows the percentage of nodes suggesting that the set group of the row is older than the set group of the column (e.g. at 83% of the Y-nodes between fan- and A-joints, A-joints abut fan-joints).

| | **FAN** | **A** | **B** | **C** |
|---|---|---|---|---|
| **FAN** | | 83% | 95% | 99% |
| **A** | 119 | | 91% | 99% |
| **B** | 105 | 247 | | 96% |
| **C** | 1 000 | 1 222 | 1 121 | |

Table 5.4 suggests that fan-A-B-C is the overall sequence of network formation. Based on this assumption, we can map the network at different time stages of network formation. Trace maps of the window sampling regions at the four "time steps" suggested from table 5.4 reveals a significant variability in jointing intensities and geometries at the four different stages of network evolution (Fig. 5.8).

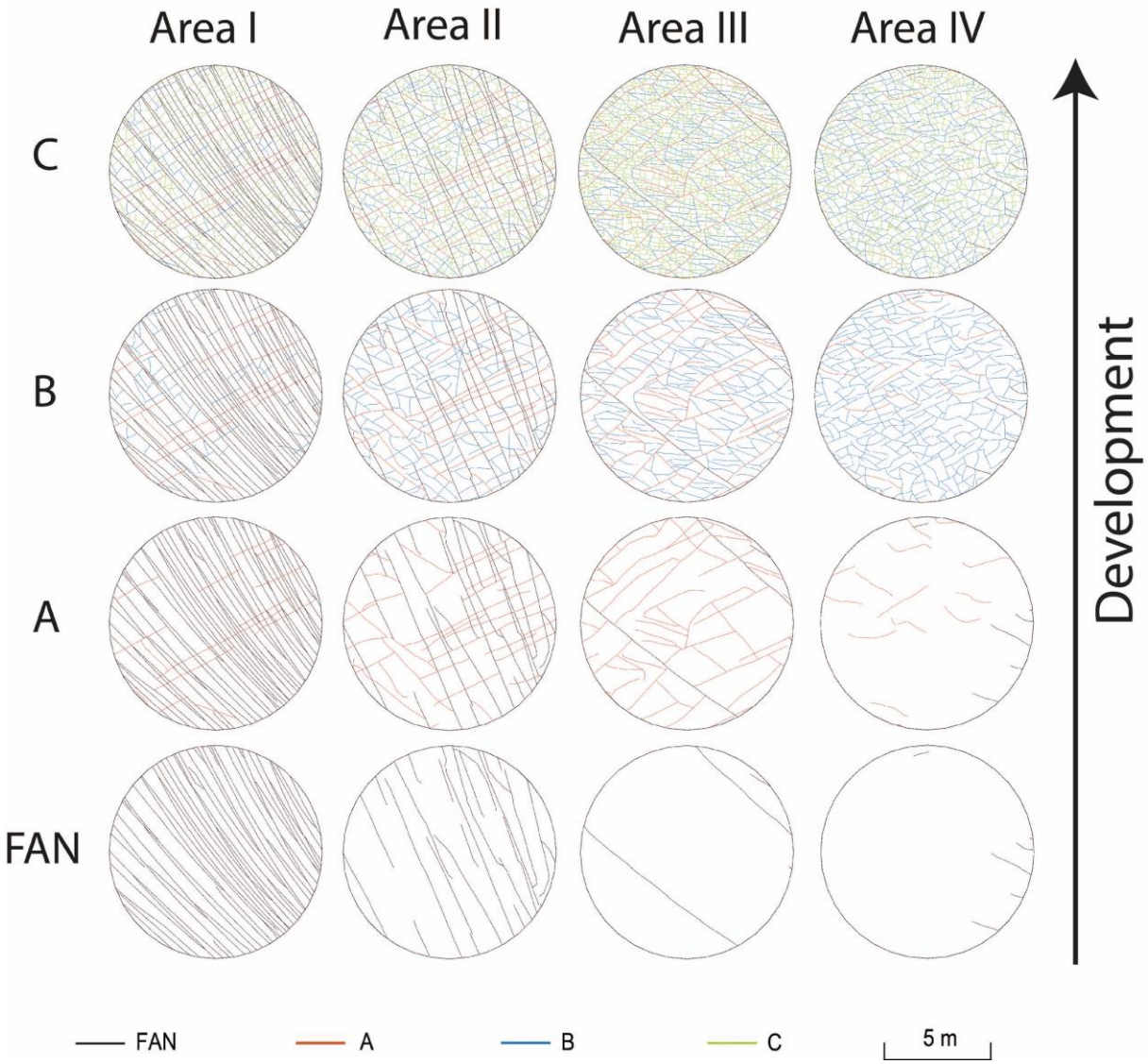


**Figure 5.8**: Development of the joint network within the window sampling areas, given the overall chronology fan-A-B-C. The location of the window samples can be seen on Fig. 5.3.

The proportions between corresponding node types (i.e. each coupled pair of entries $x_{\beta\alpha}$ and $x_{\alpha\beta}$) indicate good constraints on the relative age relationships between the 11 individual joint sets (Table 5.5). The *p*-values are calculated for each pair of joint sets, based on the proportions and total number of nodes (Table 5.5). For each two joint sets, the *p*-value indicates the probability that the sets have the same age or formed in the other order than the inferred from the abutting relationships. The *p*-values are generally found to be low, especially those between the C-sets and the joint sets belonging to the other main set groups (Table 5.6).

**Table 5.5**: Values calculated for each coupled pair in Table 5.3. The lower left half of the table denotes the total number of nodes between each two sets (e.g. the total number of Y-nodes produced by fan- and A1 joints is 51). The upper right corner of the table shows the percentage of nodes suggesting that the set of the row is older than

the set of the column (e.g. at 73% of the Y-nodes produced by fan-joints and A1-joints, A-joints abut fan-joints). The color coding refers to the *p*-values, where green squares denote *p*-values < 0.5%, yellow squares denote *p*-values between 0.5 and 5 %, whereas orange squares denote *p*-values > 5%.

| | FAN | A1 | A2 | A3 | B1 | B2 | B3 | C1 | C2 | C3 | C4 |
|---|---|---|---|---|---|---|---|---|---|---|---|
| **FAN** | | 73% | 98% | 75% | 94% | 100% | 91% | 98% | 96% | 99% | 100% |
| **A1** | 51 | | 100% | 71% | 100% | 87% | 88% | 99% | 99 | 95% | 100% |
| **A2** | 48 | 7 | | 59% | 100% | 93% | 75% | 98% | 100% | 97% | 100% |
| **A3** | 20 | 21 | 22 | | 100% | 85% | 96% | 100% | 100% | 100% | 100% |
| **B1** | 64 | 5 | 1 | 27 | | 66% | 76% | 88% | 97% | 94% | - |
| **B2** | 30 | 71 | 72 | 13 | 64 | | 75% | 94% | 91% | 99% | 97% |
| **B3** | 11 | 24 | 8 | 26 | 21 | 8 | | 96% | 100% | 94% | 94% |
| **C1** | 201 | 132 | 192 | 78 | 72 | 143 | 117 | | 55% | 77% | 76% |
| **C2** | 25 | 287 | 103 | 12 | 193 | 35 | 17 | 247 | | 56% | 64% |
| **C3** | 258 | 84 | 31 | 229 | 81 | 280 | 17 | 1007 | 95 | | 58% |
| **C4** | 516 | 26 | 3 | 45 | 0 | 70 | 51 | 34 | 155 | 60 | |

Most of the sub-sets within each set group have significantly different age than all the member sets of the other set groups (e.g. the abutting relationships indicate that set A1 is older than all the B- and C-sets). Within each of the set groups, the age relationships inferred from abutting relationships are less solid, and abutting is more prone to occur both ways (Fig. 5.9).

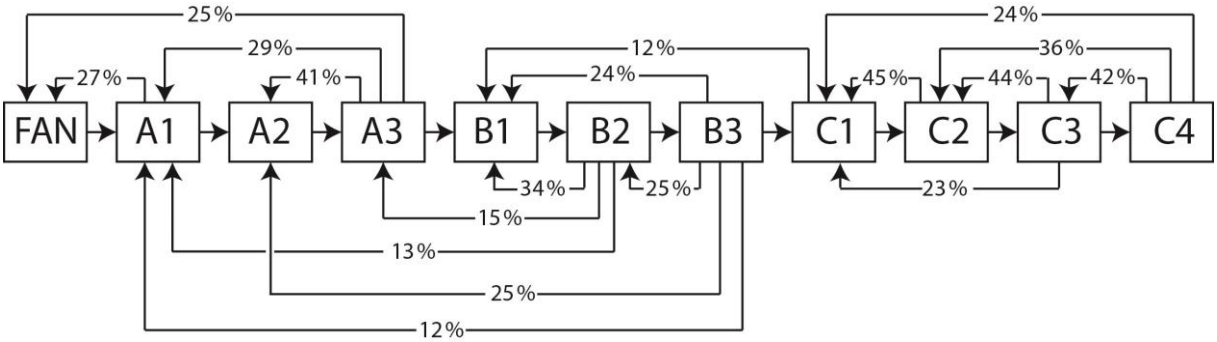


**Figure 5.9**: The overall chronology between the joint sets, and the degree of "backcycling" between them. Arrows and numbers indicate the proportion of the Y-nodes (>10%) that abut the other way than what we expect from the inferred chronology.

## 5.4 Spatio-temporal development of joint intensity

### 5.4.1 Spatial distribution of joint intensity

Intensity maps of the joint sets, where the intensities are mapped on a 1x1 m grid, show that the joint intensities are not evenly distributed throughout the digitized area, but display

considerable spatial variability (Fig. 5.10). The intensity map for the fan-joints highlights that this set experiences the highest intensity in the area where the joints converge, near the fault trace. Set A1 displays highest intensity in the interference zone between the fan structures, whereas sets A2 and A3 are largely confined to the rim of the digitized area. The B-sets are more evenly distributed throughout the area, but seem to have somewhat higher intensities in the zone with polygonal jointing between the fan structures. The C-sets generally have high intensities throughout the network; set C1 has intensities exceeding $4\frac{m}{m^2}$ in the NW corner of the digitized area, where set C3 also experiences high intensity. Set C4 is mostly confined to the fan area, whereas set C2 has intensity peaks either sides of the main fan structure.

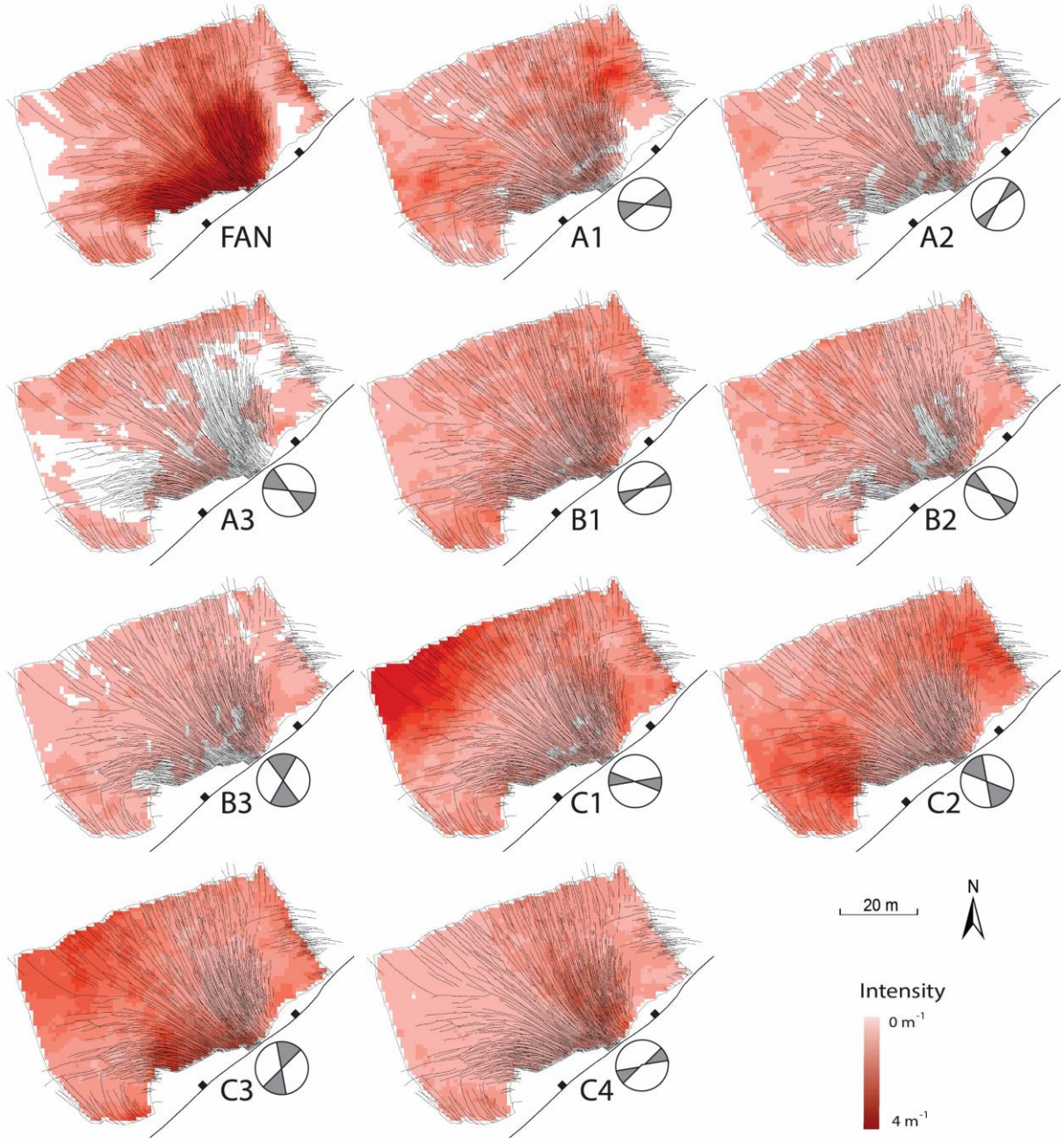

**Figure 5.10**: Intensity map of the separate joint sets. The set of fan-joints is drawn on all maps for orientation. The circle below each intensity map shows the strike range of the corresponding set.

The intensity mapping of the overall set groups (Fig. 5.11) highlights certain trends from the separate set intensity maps (Fig. 5.10); the A-group is dominated by set A1 and has the highest intensities in the zones of interference between the fan structures. The B-sets are concentrated in the areas between the fan structures, close to the fault trace. The C-sets experience the highest intensities in the distal parts of the fan-structure.

When only the set of curving joints has developed, the spatial variability is high. The formation of set groups A and B contributes to a more equal distribution of joint intensity, whereas the formation set group C apparently induces an increase in spatial intensity variation. The area that displays the lowest intensities after the formation of the A-sets, end up with the highest final intensity when all the joint sets have formed. This is especially true for the NW corner of the mapped area. The map of the present joint intensity shows that there are two areas with particularly high intensities; the area where the curving joints intersect the fault plane (i.e. the apex of the fan structure), and in the area farthest away from the fault plane, in the NW corner of the digitized area.

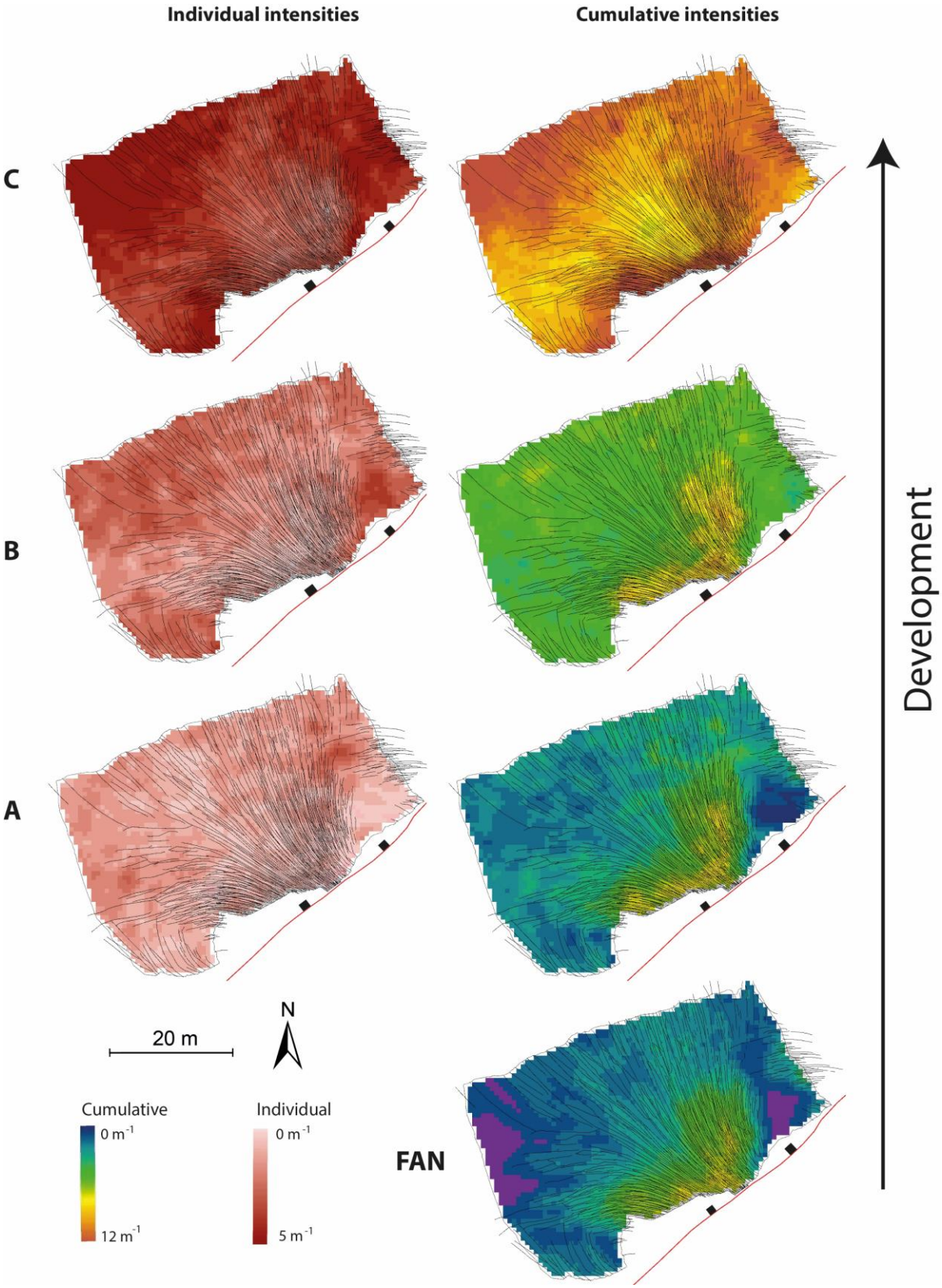


**Figure 5.11**: Cumulative and individual intensities of the major set groups A, B and C. The set of fan-joints is drawn on all maps for orientation.

### 5.4.2 Development of joint intensity

The fact that the fracture intensity gradually increases with formation of the different sets, can be seen from plots of fractures intensity for the different stages of development for the window sampling regions and for the whole network. The intensity increases gradually during the formation of the A- and B-sets, but experiences a more rapid increase resulting from the formation of the C-sets. This trend can be seen for the entire network, and within each of the four window sampling regions (Fig. 5.12).

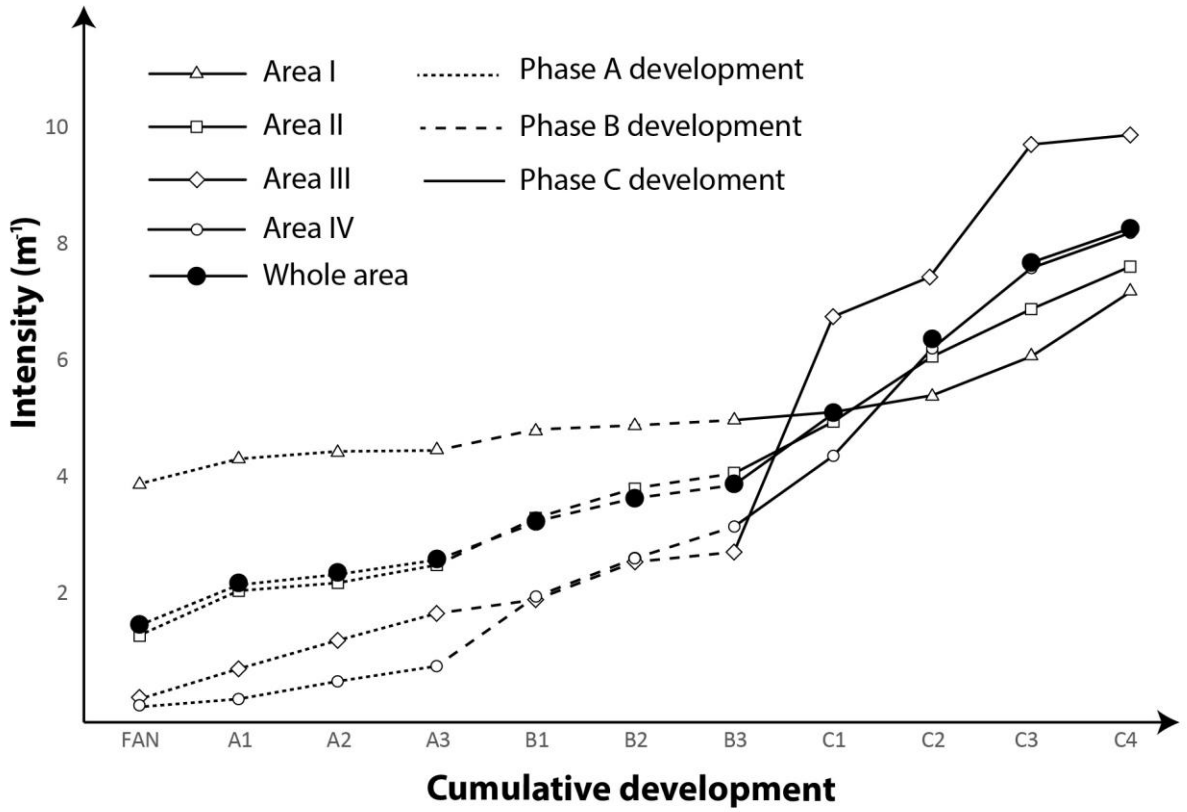


**Figure 5.12**: Development of joint intensity in the four window sampling areas, as well as for the entire digitized area.

## 5.5 Network topology and connectivity

### 5.5.1 Development of topological measures

Values of node- and branch types at different stages of joint development (Table 5.7) shows that the numbers of node and branches are sparse at early stages of network development (full overview of node- and branch- development in the circular window sampling areas, see Appendix III). However, the number of Y-nodes and CC-branches increases in a near exponential manner with the formation of progressively more joint sets. The number of X-nodes experiences a significant increase with the formation of set A1, before increasing more

moderately during the formation of the other joint sets. The number of I-nodes apparently increases step-wise, before going almost extinct after the last step of joint formation (set C4).

**Table 5.7**: Absolute values (#) and proportions (%) of node and branch types at different stages of network development within the whole area.

| | **I-nodes** | | **Y-nodes** | | **X-nodes** | | **II-branches** | | **IC-branches** | | **CC-branches** | |
|---|---|---|---|---|---|---|---|---|---|---|---|---|
| | # | % | # | % | # | % | # | % | # | % | # | % |
| **FAN** | 919 | 75 | 256 | 21 | 52 | 4 | 225 | 27 | 342 | 41 | 268 | 32 |
| **A1** | 1 227 | 30 | 1 080 | 27 | 1 758 | 43 | 99 | 2 | 924 | 16 | 4 586 | 82 |
| **A2** | 1 854 | 33 | 1 831 | 33 | 1 870 | 34 | 240 | 3 | 1 275 | 18 | 5 743 | 79 |
| **A3** | 1 733 | 28 | 2 456 | 39 | 2 094 | 33 | 179 | 2 | 1 293 | 15 | 7 075 | 83 |
| **B1** | 3 197 | 28 | 5 141 | 44 | 3 269 | 28 | 544 | 4 | 2 010 | 13 | 13 032 | 84 |
| **B2** | 2 809 | 20 | 8 099 | 57 | 3 425 | 24 | 265 | 1 | 2 208 | 11 | 17 607 | 88 |
| **B3** | 2 323 | 14 | 10 129 | 63 | 3 694 | 23 | 139 | 1 | 1 987 | 9 | 21 272 | 91 |
| **C1** | 5 917 | 19 | 21 992 | 69 | 3 843 | 12 | 1 046 | 2 | 3 691 | 9 | 38 319 | 89 |
| **C2** | 6 403 | 11 | 48 423 | 82 | 3 943 | 7 | 733 | 1 | 4 796 | 6 | 77 342 | 93 |
| **C3** | 2 250 | 2 | 87 116 | 93 | 4 060 | 4 | 106 | 0 | 2 015 | 1 | 136 978 | 99 |
| **C4** | 209 | 0 | 102 527 | 96 | 4 224 | 4 | 0 | 0 | 208 | 0 | 161 500 | 100 |

Triangular plots of topological measures (Fig. 5.13 a) indicate considerable spatial variability in the development of node types; three of the four circle sample areas are dominated by I-nodes during the formation of the set of converging joints. The formation of set A1 pushes two of the four circle sample region towards the X-node corner of the diagram, a trend that can also be observed for the development of the whole region. From the formation of set A2 and onwards, the network gets progressively more dominated by Y-nodes, a tendency which is apparent in all the circle sample areas. The branch type plot (B.13 b) reveals that the network converges rapidly towards the CC end member.

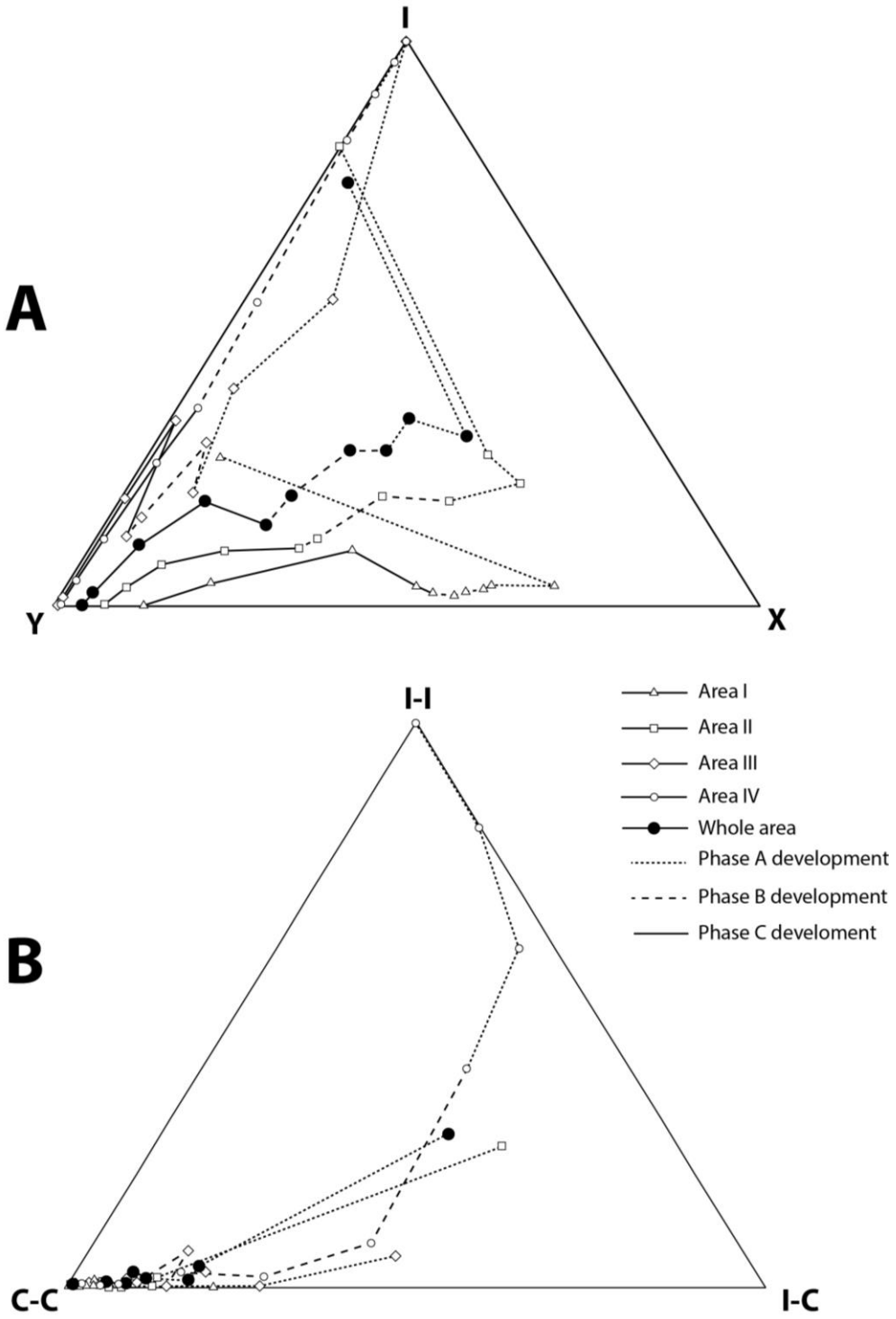


**Figure 5.13**: Ternary diagrams showing the proportions of node types (**a**) and branch types (**b**) in the different window sampling areas at different stages of joint development.

The network has a low average node degree after the formation of the fan-joints. Though the average node degree varies throughout the network, all the circle sample areas sees the lowest average node degree at this stage (Fig. 5.14). Because set A1 has the tendency to cross-cut the fan-joints (i.e. creating X-nodes), the formation of this set leads to a sudden increase in average

node degree manifested in three of the four window sampling areas. After the formation of this set, the plots of the regional node degrees converge asymptotically towards 3, as the sampling areas gets increasingly dominated by Y-nodes. Sampling area IV also converges towards an average node degree of 3, though significantly slower than the other areas.

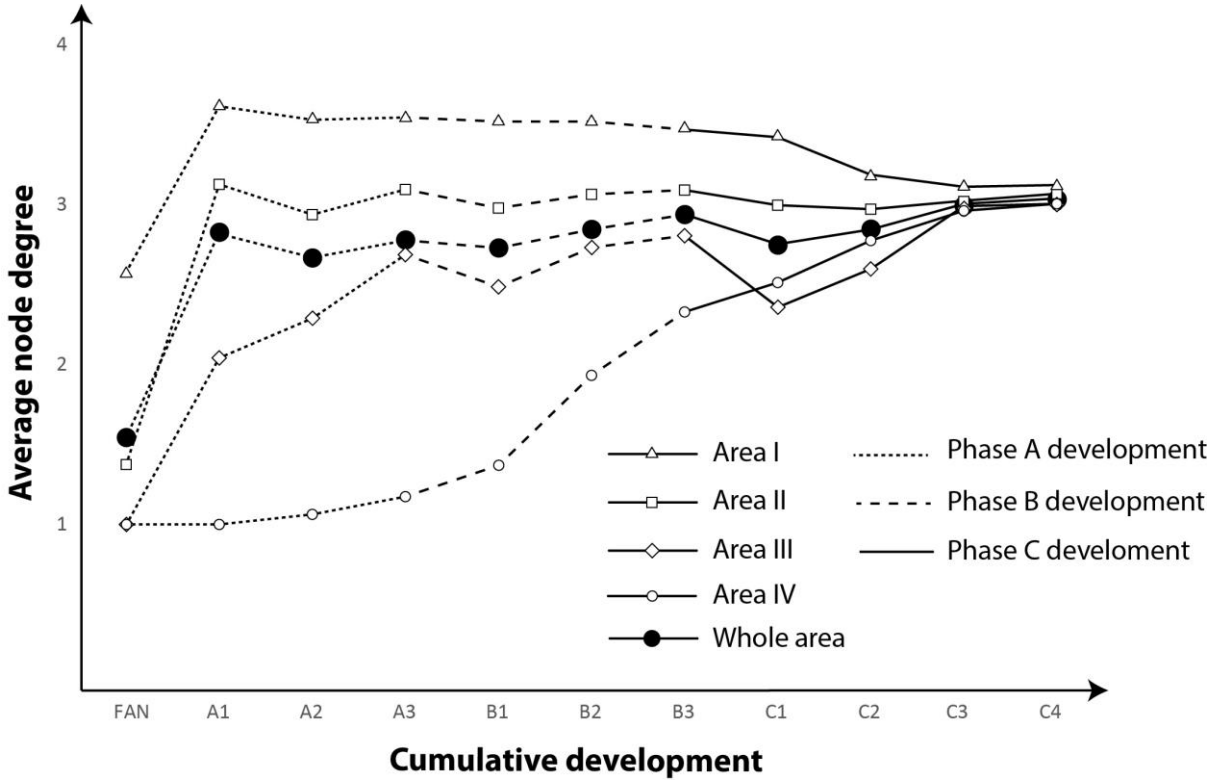


**Figure 5.14**: The average node degree in different parts of the network at different stages of network development.

### 5.5.2 Connectivity development

Grid maps of node frequencies at different time steps in network evolution (Fig. 5.15), shows that I-nodes dominate the network after the formation of the set of converging joints, and that these nodes are primarily found in distal parts of the fan-structure. The connecting node frequency is at this stage mainly contributed by Y-nodes, which can be found in the zone of convergence. The formation of the A-sets leads to higher X-node density, which is largely confined to central parts of the fan-structure, where it remains high throughout the last two phases of development. Stages B and C makes the network progressively more Y-node dominated, with particularly high Y-node density developing in the NW part of the area after the formation of the C-sets. I-nodes appear scattered after the formation of A-sets and B-sets, but are almost non-existent after the formation of the C-sets.

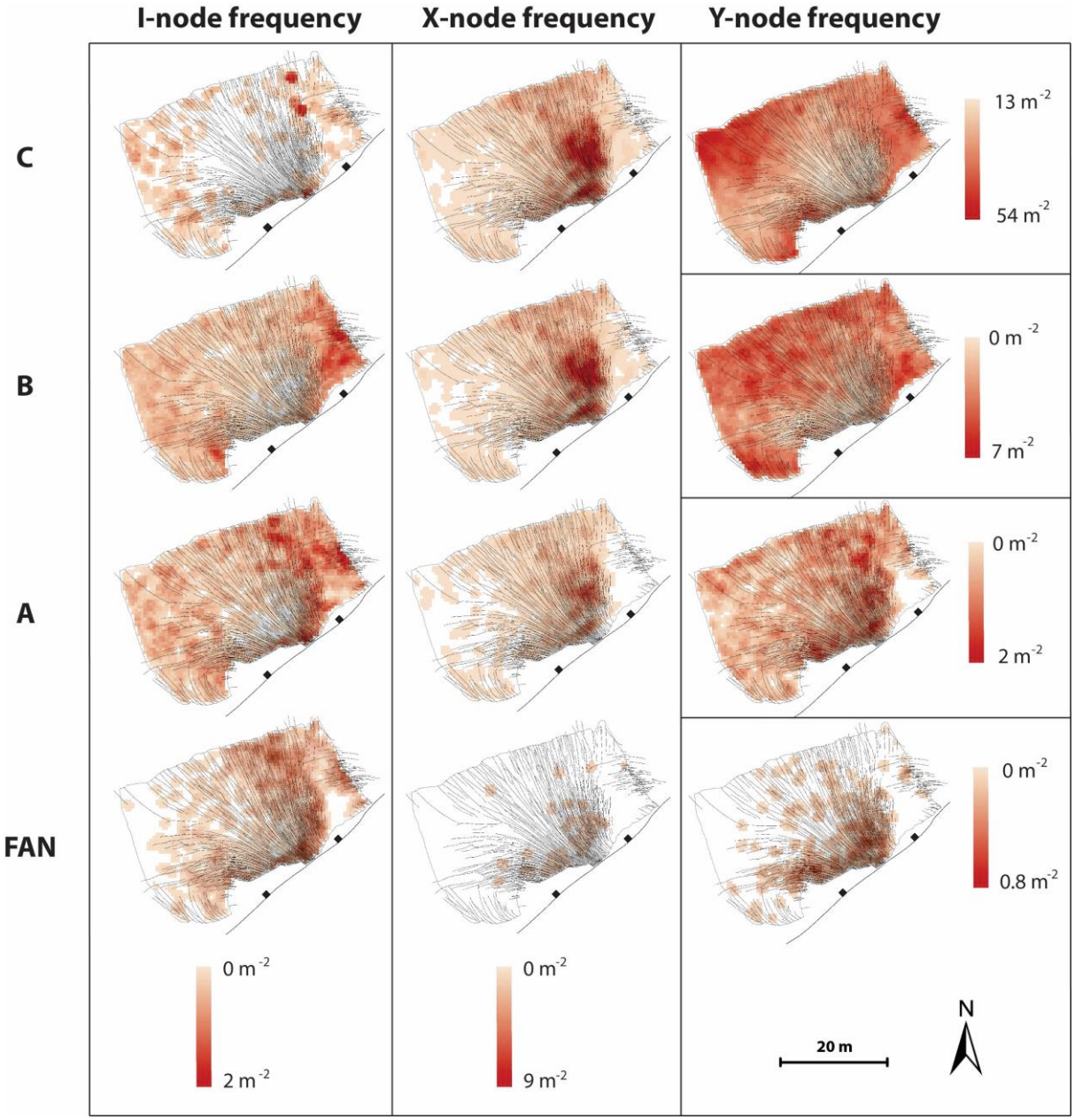


**Figure 5.15:** Cumulative development of the I-, X- and Y-node density after the formation of the set groups. The set of fan-joints is drawn on all maps for orientation.

The connectivity is low (connecting node frequency < 0.1 $m^{-2}$) after the formation of the fan-joints, for the entire network as well as for each of the window sampling regions. The connecting node frequency experiences a gradual increase during the formation of the A-sets and B-sets, to a value of around 4 $m^{-2}$ for the whole network (Fig. 5.16). Set C1 marks a change of pace in the formation of connecting nodes, and the connecting node frequency rises rapidly during the formation of the C-sets to about 33 $m^{-2}$.

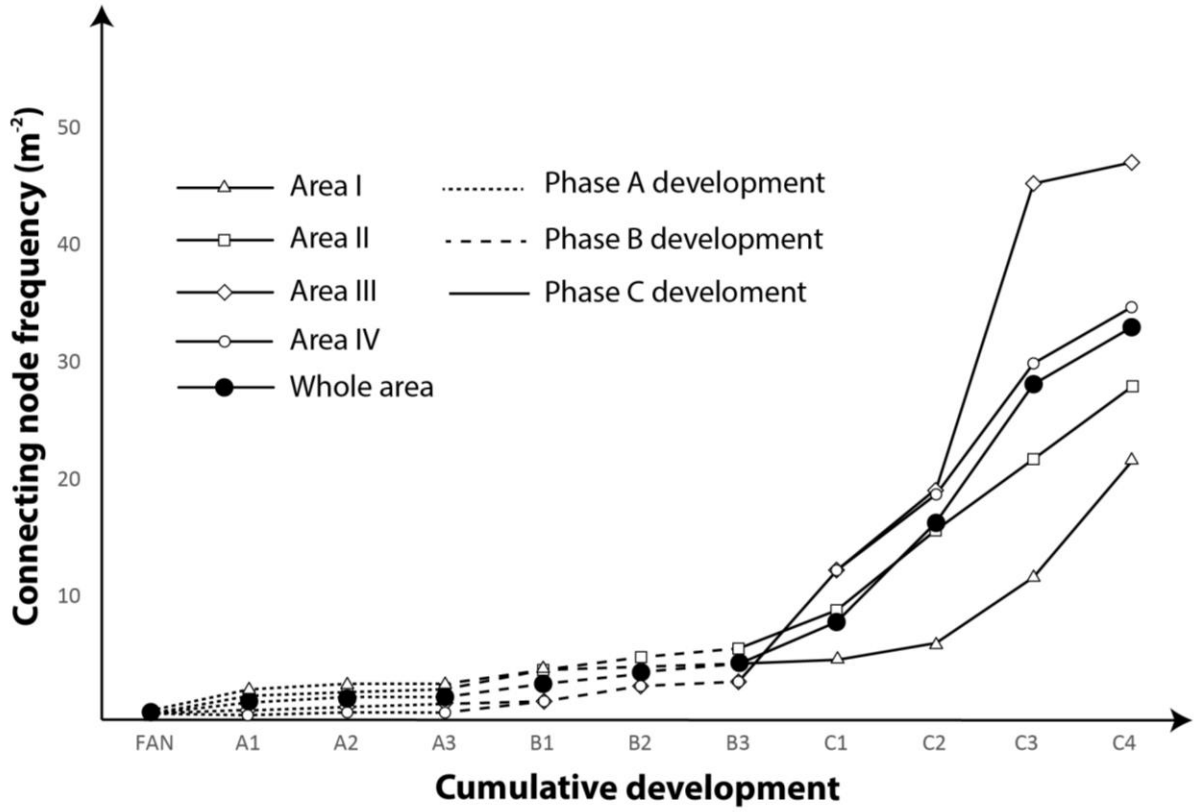


**Figure 5.16**: Connectivity (connecting node frequency) evolution as response to network development in each of the window regions and within the whole analyzed area.

## 5.6 Styles of block break-up and block size distribution

### 5.6.1 Spatial distribution of block break-up

The block map shows that few blocks are confined (i.e. surrounded by joints) after the formation of the fan structure. The 33 blocks that exist at this point of development are confined to the fan-area, which is also apparent on grid maps of block sizes and block numbers (Fig. 5.17). The formation of the A-sets increases the number of confined blocks to 2 606, which are distributed in larger parts of the studied area. The area between the fan structures do, however, not contain confined blocks. The block size map shows that small blocks dominate in central parts of the fan-structure. The formation of the B-sets increases the number of blocks to 7 626; small blocks are still primarily associated with the fan-structure, but most of the study area is now intersected by blocks. After the formation of the C-sets, the study area contains 55 167 blocks, and small blocks are no longer confined to the fan area. On the contrary, small block sizes are also found in the NW corner of the study area, whereas the central area of the fan has larger blocks. This pattern closely resembles the pattern of joint intensity. The inversely proportional relationship between number of blocks (per grid cell) and block size is also apparent.

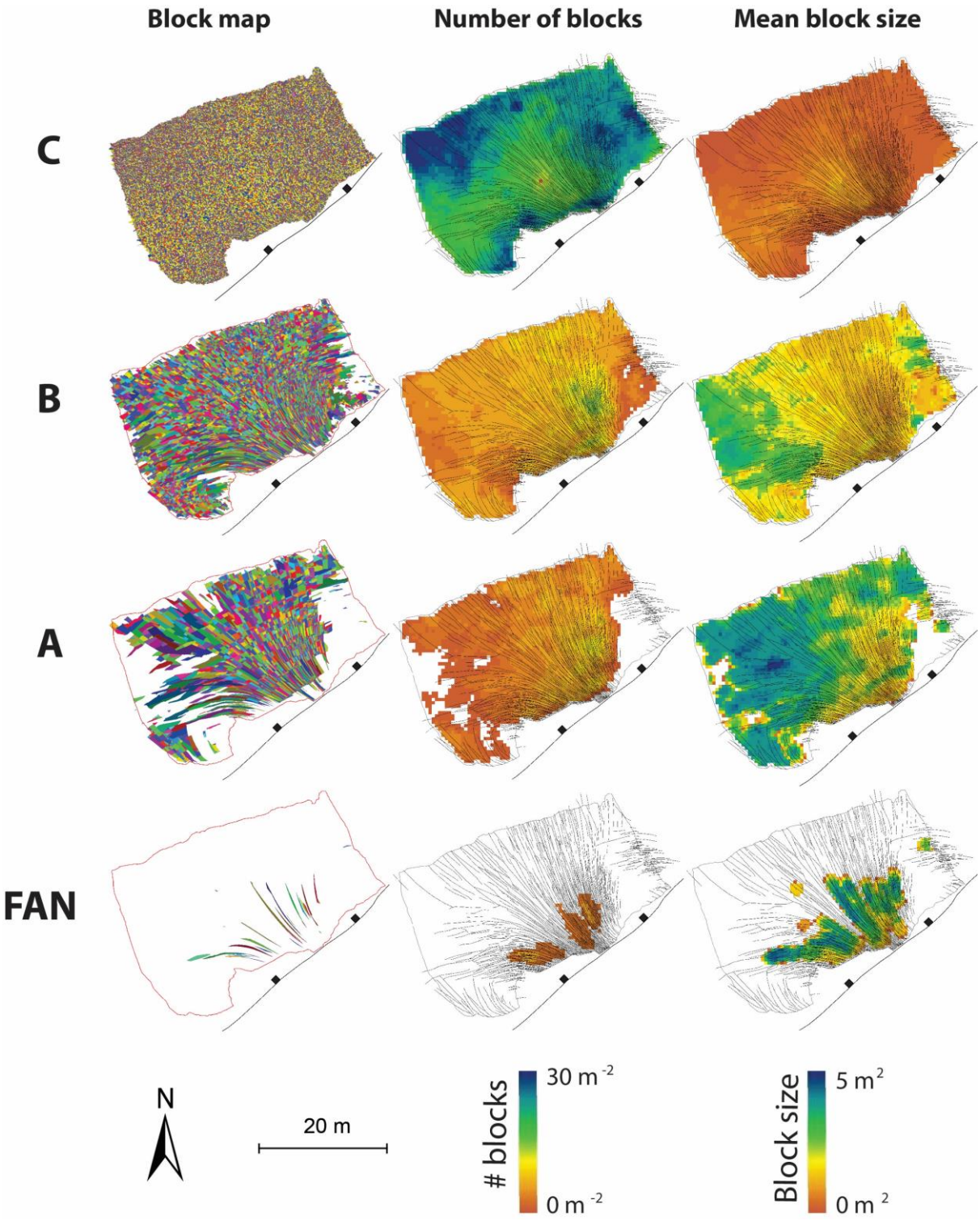


**Figure 5.17**: Development of block break-up characteristics after the four major steps of network development, i.e. the formation of the fan-joints and the A-, B- and C-sets.

### 5.6.2 Block break-up styles

A visual interpretation of joint set interaction in the field and on drone images, displays different styles of interference between the joint sets, and consequently different styles of block break-

up. This is not readily quantifiable, but examples from joint trace maps illustrate important differences qualitatively.

Set A1, unlike the other joint sets, has the tendency to cross-cut the fan-joints, despite the fact that set A1 is found to post-date the fan structure (Fig. 5.18 a). In other cases, the joints which are found to be younger deflect in the proximity of older joints and show a tendency to abut them at an angle close to 90º (Fig. 5.18 b). In central parts of the fan-structure, fan joints are found to converge, creating horse tailing geometries and X-nodes with acute angles, which results in elongated and wedge-shaped block geometries (Fig. 5.18 c). In the same areas, C-joints have the tendency to form orthogonal ladder patterns which creates rectangular blocks. When the spacing between long joints is wider, the C-joints tend to form tangentially around X- and Y-nodes created by the longer joints. This phenomenon is responsible for blocks with one or two straight edges, and other ones which are curved (Fig. 5.18 d). In the zone between the two fan structures, where it is difficult to identify joint sets with prevailing orientation (Fig. 5.18 e), the jointing has resulted in a network of polygonal blocks, some of which with one or more curved edges. Reactivation occurs between different joint sets but is particularly pronounced between fan-joints and A2-joints (Fig. 5.18 f).

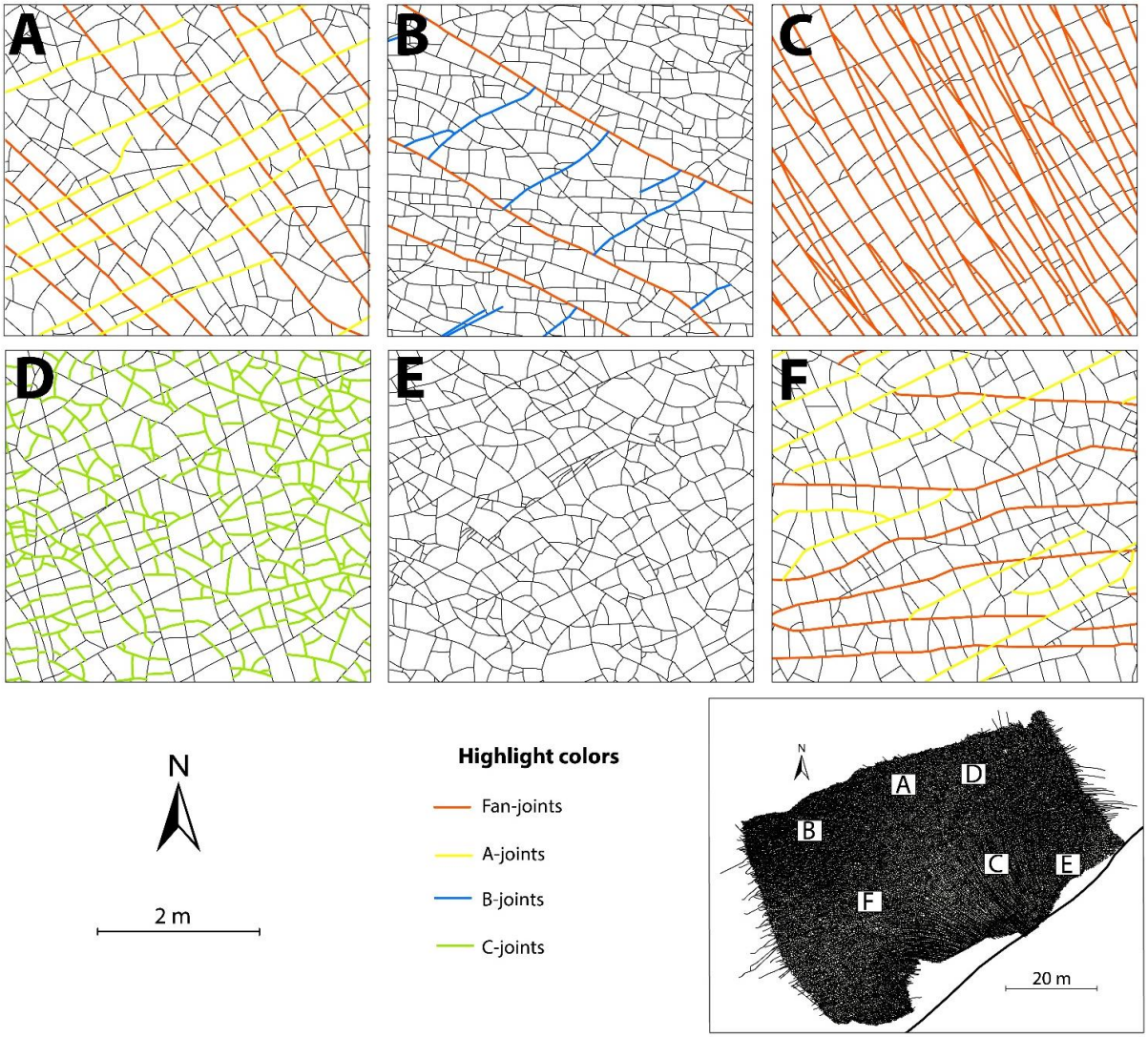


**Figure 5.18**: a) Fan- and A1-joints; the A1-joints have a tendency to cross-cut the fan-joints, but abut them at other places. b) B3-joints with curved tips abut fan-joints, creating an oblique ladder pattern. c) Horse-tailing within the set of fan-joints. Orthogonal cross joints form a ladder pattern, resulting in a rectangular block break-up style. d) Short, curved joints form tangentially around nodes created by longer joints. e) Area with less pronounced strike trends; joint sets are difficult to identify, and jointing results in a polygonal block break-up pattern. f) Tip reactivation between fan-joints and A2-joints.

# 6. Discussion

This chapter summarizes key observations from the spatio-temporal network analysis and compares the results to previous research on joint network evolution. The overall aim of the section is to address the causes of spatio-temporal variability of network properties within the studied network.

## 6.1 Spatial variability in joint development

### 6.1.1 Notes on network development

The spatio-temporal development analysis gives important clues about the evolution of various network properties. The 2D joint intensity rises significantly within the study area from early to late stages of network development, from $<2$ $m^{-1}$ to $>8$ $m^{-1}$ (Fig. 5.12). The network connectivity (measured as connecting node frequency) increases with about two orders of magnitude over the same time span (Fig. 5.16), yielding an average connecting node frequency $>30$ $m^{-2}$. This displays that network intensity and connectivity are not directly proportional (Sævik & Nixon, 2017). This increase in connectivity can largely be ascribed to the formation of Y-nodes, which number-wise dominate the network in later stages of development (Table 5.7; Fig. 5.13 a; 5.14). The topological pathways of branch proportions converge even more rapidly towards the CC-branch end member, than what is the case for the node proportions (Table 5.7; Fig. 5.13 b). The analysis shows that network geometries are spatially variable (Fig. 5.8; Fig. 5.18), and that network properties display major differences on the meter scale (Fig. 5.11). These observations of general trends in the evolution of joint network properties are in accordance with previous studies investigating topological and geometrical aspects of natural fracture networks (Manzocchi, 2002; Morley & Nixon, 2016; Procter & Sanderson, 2018). The rest of this discussion will mainly focus on various network-controlling factors, and their contribution to the evolution of the joint network.

### 6.1.2 Regional significance

Previous studies analyze joint sets, joint set properties, chronology and jointing style in outcrops near the study area analyzed in this thesis. A comparison with the findings in these studies give indications of the regional significance of the results from this study.

The exposure analyzed by Loosveld & Franssen (1992) is located about 260 m away from the study area, but on the same limestone bedding surface, the Bench. This study identifies five,

possibly six joint sets in the exposure, defined by their orientation, and find them to follow negative exponential length scaling distributions. Despite the short distance between the study areas, it is difficult to recognize the joint sets described by Loosveld and Franssen (1992). Nonetheless, the jointing style, i.e. strata-bound joints forming networks with high connectivity dominated by Y-nodes, fits with the observations of the outcrop investigated in this analysis. Some of the joint sets that this study identifies can apparently be described with negative-exponential length distribution (Fig. 5.7), and these may accordingly correspond to the ones identified by Loosveld & Franssen (1992).

Rawnsley *et al.* (1998) also documents the joint patterns in and around the area analyzed in this study. In the 1998 paper, Rawnsley *et al.* remark the existence of numerous fan structures in the area and point out the fact that one joint set deflects in proximity of the fault trace. The deflecting joints, Rawnsley *et al*. (1998) continue, is probably the oldest joint set in the area, an assumption based on length and abutting relationships. This observation is very much in line with the results from this study. Rawnsley *et al.* (1998) also describe different fracture patterns and block break-up patterns which resemble the ones identified in this study, and ascribe the development to different phases of jointing, which corresponds to discrete tectonic stress events that affected large parts of the BCB. Phase 3 of jointing described by Rawnsley *et al*. (1998) may correspond to set referred to as A3 in this study, suggested by similar orientation and chronology. Rawnsley *et al.* (1998) ascribe this phase of jointing to the relaxation of Alpine compressional stresses and describe an apparent anticlockwise rotation of $\sigma_H$ during this stage. This study finds no evidence for anticlockwise rotation of the stress field in the studied section of the Blue Lias exposed in the Lilstock Beach outcrops.

Engelder & Peacock (2001) document the joint sets and jointing styles in the limestone beds that constitute the Lilstock buttress anticline, located in the footwall of the main fault in the study area, but also analyze joint sets within the Bench. This study, which is based on more thorough mapping of the local fracture patterns, identifies six joint sets and tries to correlate them with the ones described by Loosveld & Franssen (1992) and Rawnsley *et al*. (1998). Engelder & Peacock (2001) describe the set of joints that curve towards the fault trace, but also document considerable variability in jointing style within and between limestone beds. Apart from the set of fan-joints, correlation between joint sets described by Engelder & Peacock (2001) and the ones identified in this study is not apparent.

In conclusion, the spatial variability of joint sets is generally high in the Lilstock Beach exposures, and it is difficult to correlate joint sets over distances as small as a few hundred

meters (Procter & Sanderson, 2018). This contradicts the findings of Rawnsley *et al.* (1998), which identifies joint sets that are persistent throughout the Bristol Channel Area. The most likely reason why this study does not match with these regional trends, is that this study focuses on a smaller area than Rawnsley *et al.* (1998) and is more likely to detect joint sets controlled by local stresses, rather than regional ones. Another reason why it is difficult to make a meaningful comparison between the sets constituting the studied fracture network and the fractures a few hundred meters away, can be a higher structural complexity in the studied area (Peacock & Sanderson, 1999). This structural complexity can be ascribed to the anomalous trend of the fault trace (Kelly *et al.*, 1999) and the minor faults which are splaying from the main fault, which may affect the deformational style in the study area (Engelder & Peacock, 2001).

The joint trace map made in this study, which is more complete than the ones made in previous studies of the Lilstock Beach outcrops, is a good starting point for elucidating local controls on fracture network development in structurally complex settings, even if it is not possible to draw conclusions concerning the deformation history of the Somerset Coast or even the rest of the Lilstock area.

## 6.2 The role of structural inheritance for joint network development

This study shows that jointing is affected by various pre-existing structures at all stages of joint network evolution. The effect of structural inheritance on joint network geometries is demonstrated by e.g. Peacock *et al.*, 2018, and may account for much of the spatial variability of network properties. This section investigates how different pre-existing structures influence joint formation.

### 6.2.1 The role of faults for jointing style

Quantification of joint network properties from this study shows that faults can play a major role in the formation of joint networks and heterogeneities in network properties. The most striking examples of fault-controlled jointing are the fan structures, where joint traces intersect the fault trace perpendicularly and radiate away from it (Fig. 5.3), a geometry which has previously been described by e.g. Rawnsley *et al.* (1992), Kattenhorn *et al.* (2000) and Bourne & Willemse (2001). The fault controls the spacing of the set of fanning joints, which increases with distance from the fault trace. This phenomenon is responsible for heterogeneities in network properties in the wall damage zone at all stages of joint development (Gabrielsen & Braaten, 2014; Peacock *et al.*, 2016a). Throughout the episodes of joint formation, the network

experiences high intensity and connectivity in the area around the apex of the fan structure (Fig. 5.11).

Some of the minor faults evidently also assert control on the jointing style, as joint traces are shown to deflect in their proximity (Fig. 6.1). These geometries can largely be explained by fault-controlled stress patterns, which are discussed in section 6.3.1.

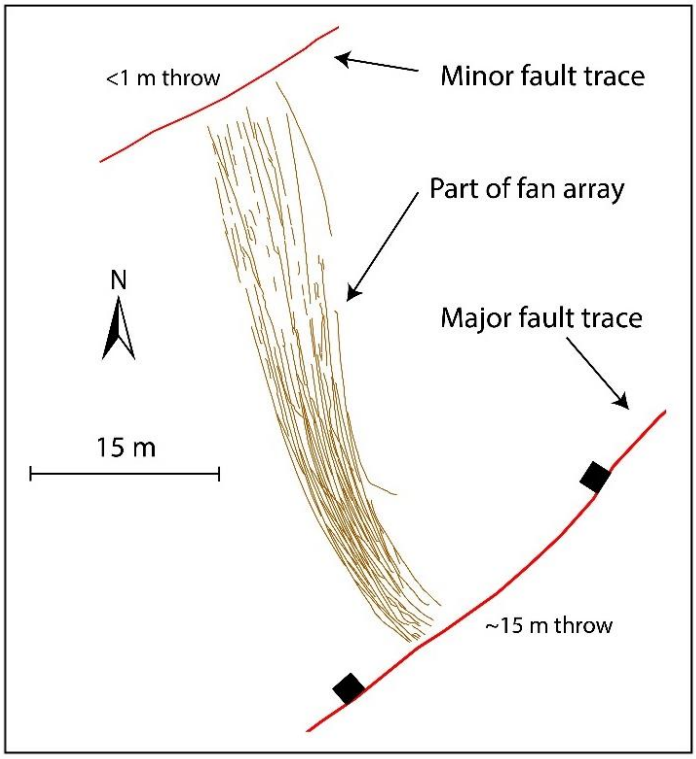


**Figure 6.1:** Sub-set of the fan structure; the joints seem to curve near a minor fault trace, as well as in proximity of the main fault.

### 6.2.2 The role of veins for jointing style

This study shows that the presence of veins controls jointing style and the evolution of joint network properties in the studied limestone bed. The parallelism between joint set A1 and the array of veins, combined with field observations of veins reactivating as joints (Fig. 5.2 a) justifies the assumption that all or most of the joints belonging to set A1 originated as veins (Fig. 6.2; Peacock, 2004).

The behavior of set A1-joints is anomalous, as they are commonly found to cross-cut the fan-joints, despite the fact set A1 is believed to be the youngest of the two. This trend significantly alters the topological properties and certainly affects the topological pathway of the network. The formation of set A1 induces a rapid increase in the proportion of X-nodes, especially in the area close to the apex of the fan structure (Fig. 5.8; Fig. 5.13). The same trend can be seen on

the plot of average node degree (Fig. 5.14), which increases as a result of set A1s tendency to produce X-nodes. The fact that this set apparently exploits pre-existing discontinuities with the layer, i.e. veins, explains the anomalous joint behavior, and provides an example of vein-asserted control on joint geometry and the implications for network properties. Gudmundsson & Brenner (2001) conclude that veins is one of the discontinuities within layers that may lead to joint arrest, which may explain the degree of "backcycling" between fan-joints and set A1 (Fig. 5.9).

The array of HDVs, which also constitute horizons with different mechanical properties within the limestone beds, may also be prone to reactivate as joints (Roberts, 1974; Caputo & Hancock, 1998; Peacock, 2004). Set C1 is sub-parallel to the HDVs, and it is therefore reasonable to assume that this set originated as HDVs, before reactivating as joints. The fact that the formation of set C1 does not seem to induce the formation of X-nodes, may suggest a smaller mechanical anisotropy posed by the HDVs, compared to that of the other set of veins (Peacock *et al*., 2018).

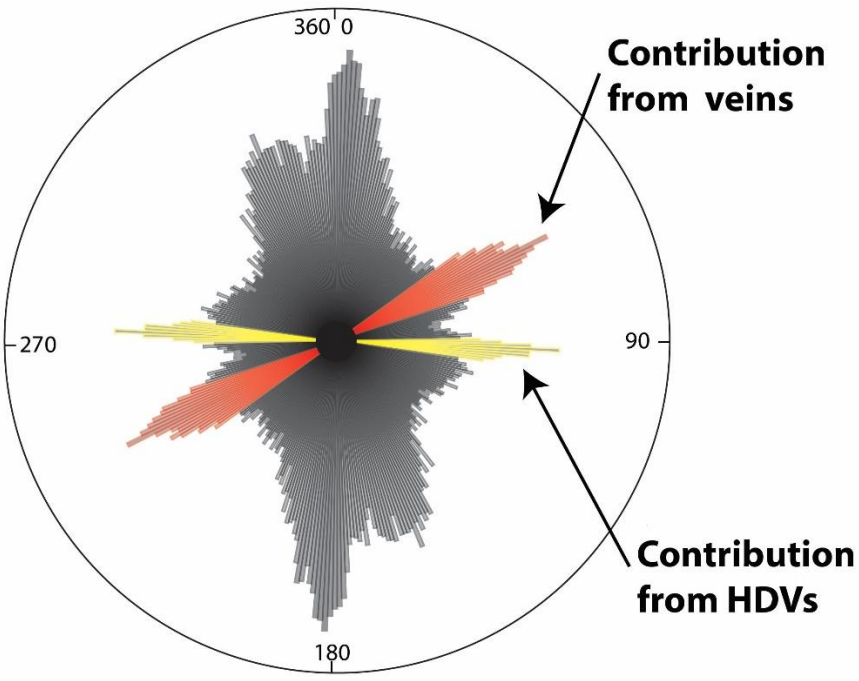


**Figure 6.2**: Non-weighted rose diagram of the non-fanning joints. The ESE-WSW peak sector (highlighted red) may result from reactivation of the set of long veins, whereas the E-W peak sector (highlighted yellow) may be related to the array of HDVs.

### 6.2.3 The role of previous joints for jointing style

Apart from set A1, which probably reactivates veins, new joints tend to abut older joint sets, rather than arresting as free tips or cross-cutting (Fig. 5.18). Consequently, the network gets

exceedingly dominated by Y-nodes (Fig. 5.13), a trend that is recognized in most natural fracture networks (Manzocchi, 2002; Nixon *et* al., 2012; Morley & Nixon, 2016; Peacock *et al*., 2018). Resulting from this resistance to cross-cutting, the length scaling distributions of younger joint sets are largely controlled by the spacing of older joint sets (Dershowitz & Einstein, 1988; Narr & Suppe, 1991; Rives *et al.*, 1992; Bonnet *et al.*, 2001). This fact makes the interpretation of length scaling distributions difficult, as the scaling properties of one set may both reflect the stress field related to its formation, but also the spacing of numerous older joint sets (Gross, 1993). The fact that joint spacing in the fan structure is a function of proximity to the fault plane (Fig. 5.3) may therefore result in spatial variation of scaling properties of the younger joint sets and exemplifies spatial variability of network properties that can be ascribed to control from previous joints.

## 6.3 Stress patterns

### 6.3.1 Controls on local stresses

Heterogeneities in joint geometries and network properties can be ascribed to local stress patterns (Dyer, 1988; Olson & Pollard, 1989; Peacock & Sanderson, 2018) as the stress field within limestone beds can be perturbed by existing structures (Engelder & Geiser, 1980; Kim et al., 2004; Peacock *et al*., 2017). The results from this study allow for a discussion about stress field perturbations, as joints generally follow stress trajectories (Engelder & Geiser, 1980; Whitaker & Engelder, 2005).

The fan of joints, which intersects the main fault trace perpendicularly, is a clear indication of stress perturbation in proximity of the fault (Kattenhorn *et al.*, 2000; Bourne & Willemse, 2001). Syn-deformational stress perturbations are found to impose fault-parallel and fault-perpendicular principal stresses up to several km away from fault zones (Maerten *et al.*, 2002; Tavani & Muños, 2012). The fan geometry indicates that $\sigma_3$ was locally oriented parallel to the fault trace in the fault damage zone at the time of joint propagation, in certain areas with elevated differential stress (Rawnsley *et al.*, 1992; Faulkner *et al*., 2006). Fault-controlled joint deflection is apparent up to ~50 m from the main fault trace, providing a minimum extent of the perturbed stress field imposed by the fault at this stage of joint propagation.

The mechanism behind localized fault-related stress build-up is a matter of discussion within the scientific community. Rawnsley *et al.* (1992) and Bourne & Willemse (2001) postulate that stress concentration primarily results from irregularities along the fault plane (i.e. fault bends etc.), based on numerical modelling experiments of stress field development around faults. This

is, however, not coherent with the findings in this study, as the most prominent fan structure abuts a section of the fault trace which is relatively straight, not in the area where the fault trace bends (Fig. 5.1). Engelder & Peacock (2001) speculate that stress concentrations in the Lilstock beds result from friction along limestone-limestone contacts during reverse reactivation of high-angle normal faults related to Alpine reactivation of the BCB. The fact that the fanning structure prevails in adjacent limestone layers (Fig. 5.2 c) contradicts this proposition. If the stress build-up is related to limestone-limestone contacts, one would not expect this stress pattern to affect the entire sequence. The results in this study may indicate, however, that the arrangement of the minor faults in the footwall is responsible for the stress concentrations that result in fan structures in the hanging wall, as the intersections between the minor faults and the major faults seem to coincide with the apexes of the fan structures (Fig. 5.3). This indicates major differences in stress orientation and magnitude along the fault trace, a factor that complicates network predictability.

The abutting relationship indicates that the joints post-date fault nucleation, and e.g. Procter & Sanderson (2018) conclude that the fan-joints propagated at a much later stage than the normal fault movement, possibly as a result of post-inversion uplift and exhumation. In this case, the joint curvature must be a result of residual stresses accommodated in the rock over time, resulting in elevates differential stress in certain areas, as suggested by the > 50 m joint traces of the fan structures (Rawnsley *et al.*, 1992). The area between the fans are characterized by jointing with little or no preferred orientation, resulting in a polygonal block break-up pattern (Fig. 5.18 e), which is associated with horizontally isotropic effective tension (Rawnsley *et al.*, 1998; Weinberger, 1999).

The existence of joints also asserts control on the local stress field, though in a narrower zone than the faults (Dyer, 1988). The fact that joints tend to abut other joints at ~90$^{o}$ indicates a local reorientation of stress field, where $\sigma_3$ lies in the joint plane (Dershowitz & Einstein, 1988). Judging by joint deflection geometries, joint-induced stress perturbations affect a zone up to ~0.5 m on each side of joint traces. When the spacing of a joint set is small enough, the area between the joints is completely dominated by stress release associated with the joints, resulting in ladder patterns of orthogonal cross joints (Fig. 5.18 c; Rives *et al.*, 1994; Caputo, 1995; Bai *et al.*, 2002). Oblique ladder patterns (Fig. 5.18 b) form when the joint spacing of the pre-existing joint set is bigger, and the stress field rotation does not dominate the entire spacing (Fig. 6.3; Engelder & Gross, 1993). Formation of curving joints responsible for break-up of rectangular blocks (Fig. 5.18 d) happens when decrease in confining pressure makes large

blocks unstable, and the block break-up is affected by the release zones and stress rotation around multiple older joint sets, producing curved stress trajectories in a near-isotropic stress field (Rawnsley *et al.*, 1998). Tip reactivation (Fig. 5.18 f) indicates that $\sigma_3$ was rotated orthogonal to the older joint trace in a crack-tip stress field, allowing the new joint to coincide with (i.er reactivate) the older one (Olson & Pollard, 1989).

The above-mentioned geometries elucidate the fact that stress field is affected by various brittle structures and shows great spatial variability as a result of interplay between local and regional stresses (Whitaker & Engelder, 2005).

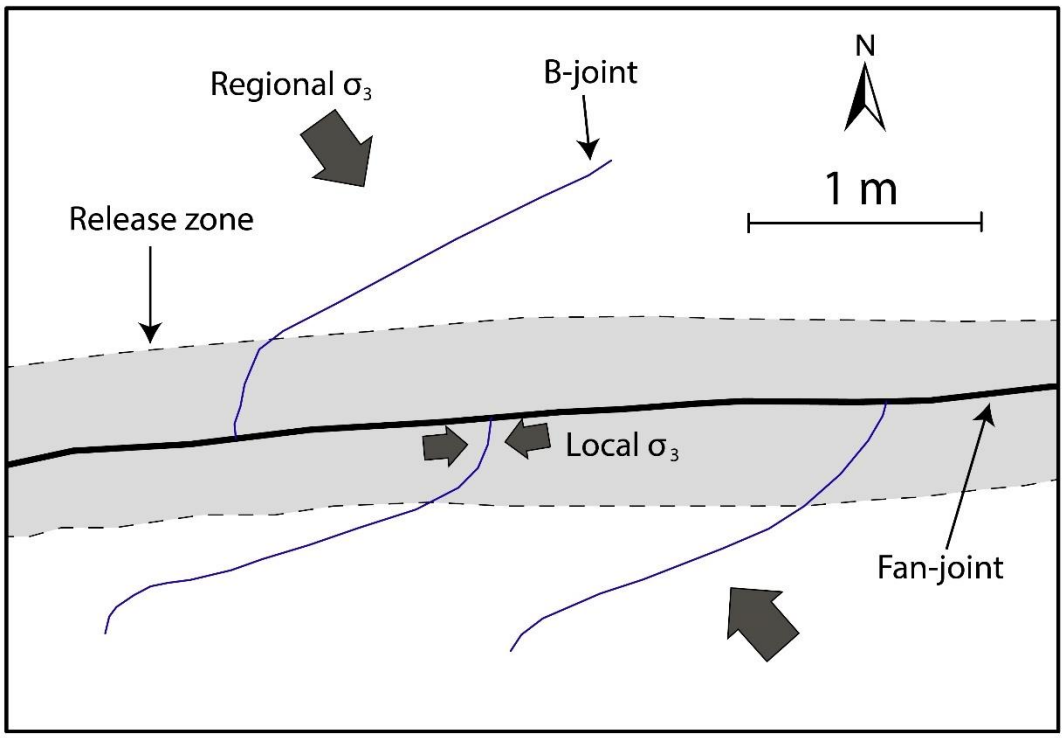


**Figure 6.3**: Trace map of joint geometries. The curvature of shorter joints can be used to analyze the size of the release zone around older joints.

### 6.3.2 Limitations in mechanical interpretation

In fracture analysis over large areas, it is common to think of joint sets as corresponding to discrete stress events (Engelder & Geiser, 1980; Rawnsley *et al.*, 1998). Because the studied joint network has formed in a structurally complex setting, it is not necessarily possible to ascribe the different generations of joint formation to regional tectonic events. Different fracture patterns in adjacent limestone beds suggests a strong mechanical contrast between shale- and limestone beds, indicating that stratigraphic properties of the sequence (e.g. layer thicknesses) affects the jointing style, to an extent that occludes the analysis of joint sets in a regional perspective (Helgesen & Aydin, 1991; Procter & Sanderson, 2018). Fluid pressure may

potentially play an important role for the geometry and distribution of joints (Secor, 1965; Olson & Pollard, 1989; Taylor *et al.*, 1999; Cosgrove, 2001), though further speculation about this and other stress-controlling factors are outside the scope of this study. Nevertheless, some of the 11 identified joint sets may partially reflect discrete, regional stress events. The C-sets seem to suggest a clockwise rotation of the stress field during later stages of network formation, which may reflect regional tectonic events. This trend is, however, not coherent with the anticlockwise stress field reorientations suggested by Rawnsley *et al*. (1998) and Engelder & Peacock (2001).

This study shows that older structures assert considerable control on the style of jointing and the corresponding joint network properties, both resulting from stress perturbations and from pre-existing mechanical anisotropies that joints may reactivate. The formation of new fracture sets induces a progressively more complex stress distribution within the limestone bed, and jointing style is controlled by an interplay between layer properties, local stresses and stresses associated with regional tectonic events (Peacock *et al*., 2018). Without a more thorough overview of regional fracture patterns, it is hard to quantify the degree to which each of the above-mentioned factors contribute to network development, and further speculation about the mechanical processes behind the formation of joint sets should therefore be supported by numerical modelling experiments.

## 6.4 Implications for understanding post-basin deformation

### 6.4.1 Model for development of joint networks

Based on the findings in this study, a model for joint network formation in the immediate hanging-wall of a fault in later stages of basin deformation has been developed. This model divides the deformation into five phases (Fig. 6.3), where each phase is associated with characteristic joint network properties and length scaling distributions.

***Phase 1***

This phase represents the basin formation. Normal faulting occurs on several fault planes: a main fault has the largest displacement (a fem meters to tens of meters), and several minor faults (<1 m displacement) are also active. The minor faults abut the main fault, producing localized stress concentrations in the linkage zone. The formation of a roll-over anticline produces localized extension in the hinge zone (Engelder & Peacock, 2001), inducing the formation of a layer-bound array of veins that strike parallel to the hinge line of the fold. Little

or no jointing happens at this stage of deformation, though the spatial arrangement of faults and veins have implications for jointing in later phases.

***Phase 2***

Concentrations of residual stress along certain sections of the main fault plane affect the propagation of fan-joints, which curve and intersect the main fault perpendicularly. These joints are also affected by residual stress perturbations associated with the minor faults and deflect in their proximity. Occasionally, the fan-joints arrest on the edge of veins from phase 1, though the veins are more frequently cross-cut by the fan-joints. The set of joints forming at this stage follows a negative exponential or log-normal length scaling distribution, which can be ascribed to physical properties of the limestone bed. The joint network is dominated by I-nodes, and is characterized by large blocks and low network connectivity.

***Phase 3***

Joints reactivate the set of veins from phase 1, possibly a result of decrease in confining pressure due to uplift, and/or preferentially oriented differential stress ($\sigma_3$ orthogonal to the veins). The set of joints that forms at this stage exhibit negative exponential length scaling properties. This length distribution may be controlled by the scaling distribution of the veins which are being reactivated, physical properties of the limestone bed and/or the spacing of the joint set that formed during phase 2. The terminations of phase 3-joints coincide with fan-joints from phase 2, creating Y-nodes, but phase 3-joints are also prone to cross-cut fan-joints. This phenomenon, which is a consequence of mechanical anisotropies, is responsible for X-node formation. This phase leads to considerably higher connectivity within the network, and a more homogenous distribution of fracture intensity.

In this study, this phase corresponds to the formation of set A1.

***Phase 4***

Episodes of increased differential stress in the entire or parts of the area, combined with the effect of decreasing confining pressure, produces sets of layer-bound joints on the meter scale. The formation of these joints is strongly affected by faults and older joints, which they tend to abut. Consequently, the network gets exceedingly Y-node dominated. Power-law length scaling properties characterize the joints from this phase, and the scaling is mainly controlled by the spacing of the joint sets from phases 2 and 3. Jointing during phase 4 leads to a more even distribution of joint intensity and connectivity, as joints are more likely to propagate in areas with low intensity in advance.

In this study, phase 4 corresponds to the formation of joint sets A2 and A3, possibly also the B-sets.

***Phase 5***

Decrease in confining pressure combined with episodes of increased differential stress results in pervasive bed-bound jointing throughout the network. Large blocks are no longer stable at this stress state, and areas consisting of large blocks after phase 4 get broken up by curving joints that follow stress trajectories within the blocks. The formation of these joints is strongly affected by the local stress field induced by adjacent structures, but the remote stress component contributes to formation of dominant strike trends. The joint tips continue to be arrested by edges of pre-existing joints, creating a well-connected network dominated by Y-nodes and CC-branches. This stage also leads to a more equal distribution of network properties throughout the network. The joint sets from this phase of network formation follow log-normal length scaling distributions, and the scaling properties are strongly affected by the spacing of the numerous pre-existing joint sets.

In this study, phase 5 corresponds to the formation of the C-sets.

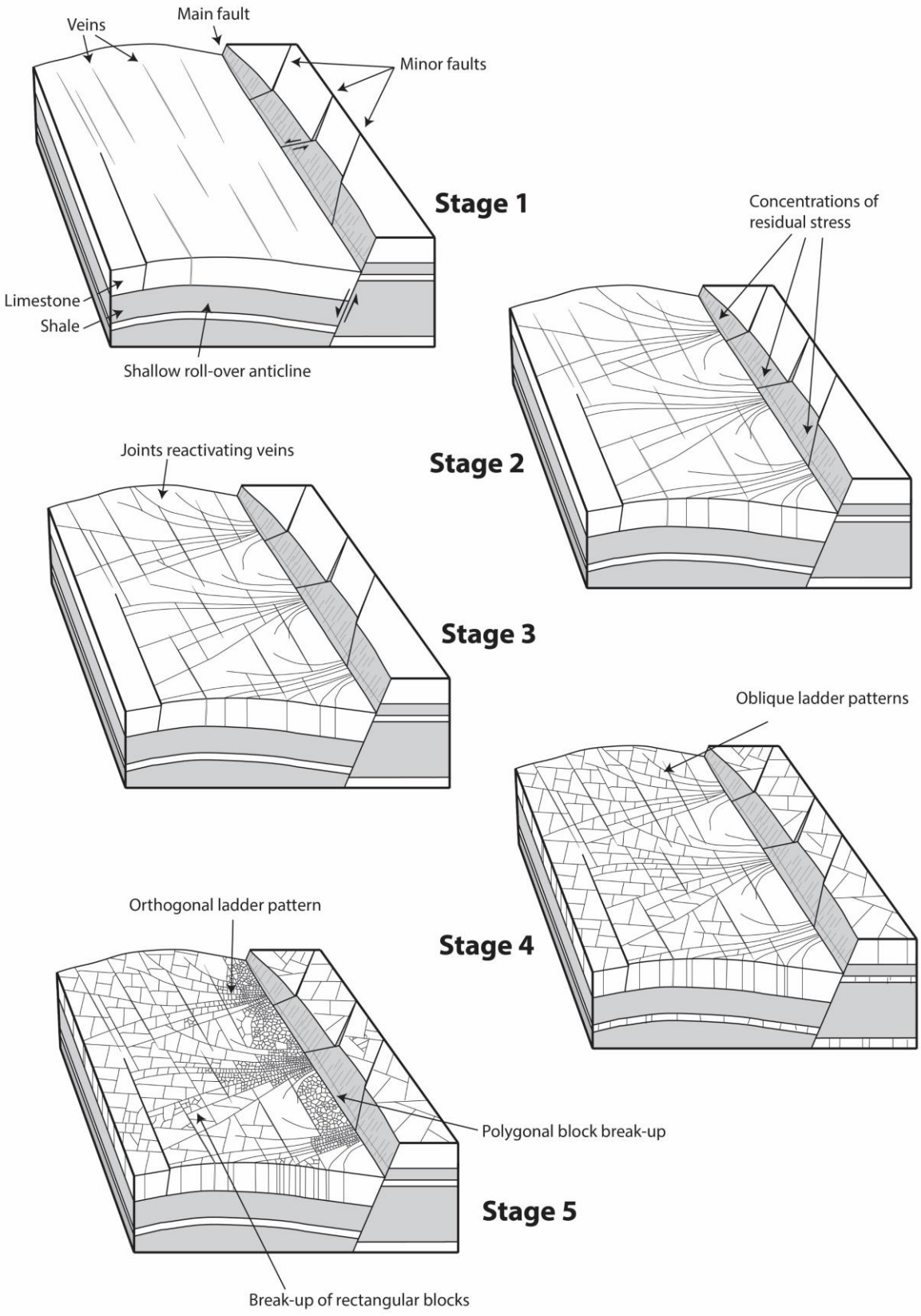


**Figure 6.4**: Stages of hanging-wall deformation during later stages of basin development.

This simplified model can to a certain degree explain the heterogeneities in network properties which are identified in this study. It resembles the model proposed by Rawnsley *et al.*, 1998, which also ascribes jointing in the Mesozoic sediments of the BCB to five distinct phases. Rawnsley *et al.*, (1998) ascribe the joints that curve towards the fault plane to what they term phase 2, which is the earliest phase in which jointing happens at Lilstock Beach. This is coherent with observations from this study, which indicate that the set of fanning joints is the oldest joint population in the Lilstock Beach exposure. The later stages in the model by Rawnsley *et al.* (1998) induce the formation of cross-joints and polygonal joint patterns, which also fits well with the observed chronology and the model presented here. The most important deviation between the two models is that Rawnsley *et al.* (1998) ascribe less control to the set of veins which are sub-parallel to the fault trace and the hanging-wall anticline. This structural inheritance is of great importance for the model proposed in this study. The structural complexity posed by the anomalous orientation of the fault through the study area may explain this deviation from previous models of deformational style in the region.

The results of the set analysis indicate that the array of HDVs may also affect the later phases of jointing, though this is not included in the simplified model for joint formation. The same can be said about the Alpine reactivation of the BCB, which might have been responsible for tightening of the roll-over anticline and may thus have contributed to formation of veins in phase 1 (Engelder & Peacock, 2001). Despite the potential over-simplification, this model may contribute to a more general understanding of controls on joint network formation in the hanging wall of large faults with complex geometries during later stages of basin development.

## 6.5 Implications and limitations

### 6.5.1 Improvement of methodology within set division

In previous studies, geologists have mainly based their set divisions on strike boundaries and used increasingly sophisticated statistical methods to detect prevailing strike directions (e.g. Odling, 1997). This study shows, however, that set division cannot purely be based on strike, but also on length. The set division proposed in this project is based on an integrated assessment of orientation, length distribution and topological properties of joint traces.

The node counting analysis, which for most of the sets resulted in a statistically significant chronological sequence, provides an indication about the correctness of the set division, given

that the joints in each set have the same age and based on the fact that most of the joint traces are arrested on previously formed nodes (Helgeson & Aydin, 1991; Peacock *et al.*, 2018). The topological analysis may thus be indicative of the correctness of the set division. A sudden increase in the proportion of I-nodes may be a result of error, either in the set definition or in the chronology, as I-nodes are rare in later stages of polyphase fracture network development (Peacock *et al.*, 2018). The fact that the development analysis suggests low proportions of I-nodes throughout later stages of network development indicates that the new methodology yields good results and can be adapted in studies of other poly-phase fracture networks. However, as showed in section 4.5.2, it can be impossible to assign strike- and length cut-off values that include all the joints corresponding to a discrete stress event (Whitaker & Engelder, 2005).

For future studies, I therefore suggest assessment of more sophisticated analysis techniques in the definition of sets, including topological aspects of each joint trace, i.e. not only strike- and length boundaries. Machine learning algorithms could potentially aid the assessment of these properties in set definition.

### 6.5.2 Structural controls on fluid-rock interaction

Joints are known to act as conduits for fluid flow in geological media, and the distribution of fractures controls the hydraulic properties of layered sequences (Caine *et al*., 1996; Aydin, 2000; Faulkner *et al*., 2010). If we look away from the possibility that different generations of joints may exhibit different hydraulic conductivity caused by stages of mineral precipitation, the analysis of joint intensity and connectivity provides a good impression about the development of fluid-flow properties of the rock (Odling *et al.*, 1999; Bourne *et al.*, 2001).

The spatio-temporal development analysis shows that the network has low connectivity during early phases of joint formation (i.e. phase 2). At this stage, the fracture intensity is confined to limited areas close to the fault trace, at the apex of the fan structure. The jointing style analysis (e.g. Fig. 5.8) suggests that the flow properties of the rock may be anisotropic, as most of the joints are parallel within each area (Odling *et al.*, 1999). The large average block size at this stage of network development implies poor fluid flow properties in most of the rock mass.

The next phase of jointing (phase 3) greatly contributes to permeability within the network, due to the large increase in connecting node frequency, notably elevated X-node frequency. The limestone bed gets compartmentalized by block break-up processes. In certain areas, the fluid flow properties may still be anisotropic, due to elongated blocks in parts of the network (Fig.

5.17; Odling *et al*., 1999; Taylor *et al.*, 1999). The subsequent stages of deformation (phases 4 and 5) are characterized by a great increase in network connectivity, e.g. an increase in connecting node frequency which exceeds one order of magnitude (Fig. 5.16). This increase in connectivity can largely be ascribed to the formation of Y-nodes (Fig. 5.15), caused by blunting of joint tips (Loosveld & Franssen, 1992; Zhang & Sanderson, 1995; Sævik & Nixon, 2017). Pervasive jointing also implies extensive block break-up throughout the network (Fig. 5.17), resulting in less anisotropic flow properties in the fracture network. Joint formation at this stage results in more evenly distributed joint intensity and connectivity throughout the network (Odling *et al*., 1999; Bai & Pollard, 2000 Sanderson & Nixon, 2018).

The analysis shows that the potential for fluid-rock interaction within the studied joint network is greatly controlled by pre-existing structures. This has important implications for the reservoir potential of layered carbonate sequences, which greatly depends on the hydraulic properties of fractures (Taylor *et al.*, 1999; Aydin, 2000).

### 6.5.3 Considerations for joint network predictability

As joints are sub-seismic structures, the study of joints in the subsurface often relies heavily on data from wells and analogue outcrop-scale joint networks (Ghosh & Mitra, 2014; Sanderson & Nixon, 2015; Sanderson, 2016). Core analysis provides limited information about the spatial variability of various joint network properties (Laubach *et al.*, 2009; Sanderson & Nixon, 2015). Though Odling *et al.* (1999) point out that the extent to which exposed rocks can provide meaningful reservoir analogues is limited, the geometries within the studied fracture network display key factors controlling tensile fracturing during later stages of basin deformation. Especially the distribution of network properties in relation to the fault zone is of interest, in order to predict network properties in subsurface fracture networks.

The model for joint development at Lilstock Beach (Fig. 6.4) suggests that knowledge about the orientation of dominant fault sets and vein sets, combined with good constraints on the stress and uplift history, allows a certain prediction of the network properties of joint networks in the subsurface. However, large spatial variability makes prediction of fracture network properties notoriously difficult, as network properties largely depend on the presence of other sub-seismic features like sub-seismic faults, vein arrays and previous joints.

# 7. Conclusions and further work

## 7.1 Conclusions

This study has attempted to elucidate the development of a polyphase joint network in a structurally complex setting, in order to study the evolution of corresponding network properties. This was done based on geometrical and topological analysis of fracture maps made from UAV imagery.

- The studied part of the exposed bedding surface at Lilstock Beach contains one set of curving joints that radiate from certain segments along the fault trace, forming fan-structures. The curvature of the joints is interpreted to result from concentrations of residual stress along the fault plane, controlled by fault intersections in the footwall. The size of the fan structure represents the extent of the wall damage zone of the fault.
- In addition to the set of fanning joints, a minimum of ten sets of sub-vertical, bed-bound joints are present in the studied outcrop, and can be distinguished based on length, orientation and topological aspects. These are interpreted to result from a sequence of episodes of differential stress.
- Abutting relationships provide a relative chronology between the joint sets. Notably, the curving joints that constitute the fan structures is the oldest of the identified sets.
- The joint sets exhibit different length scaling properties. The set of curving joints follows a log-normal or negative exponential length scaling distribution. Apart from this, the long joint sets tend to have power-law length scaling properties, whereas short joint sets follow log-normal or negative exponential length scaling distributions. Length scaling of later joints is controlled by the spacing of older joint sets, as abutting relationships outnumber cross-cutting relationships.
- The fan structures control the spatial distribution of heterogeneities in network properties through all stages of network formation, with high intensity and connectivity being associated with the apex of fan structures. The spacing between the fan-joints is variable and controls the styles of block break-up, which include orthogonal ladder patterns, oblique ladder patterns and polygonal jointing. This, combined with the tendency for joints to abut at ~90$^{o}$, indicate that local stress perturbations exist in the proximity of joints.
- Veins represent structural inheritance which controls joint formation. Veins that pre-date joint formation enhances cross-cutting relationships (X-nodes), which is important

for network connectivity during early stages of network development. HDVs also represent mechanical horizons that are prone to reactivate as joints.

- The network develops from being dominated by I-nodes to becoming Y-node dominated. Central parts of the fan structure are dominated by X-nodes at certain stages of network evolution, so the topological pathways of network development show spatial variability. Prevailing fracture orientations may have enhanced directional permeability in early stages of network development but is unlikely to characterize the network at the present stage.
- The jointing style is variable within and between limestone beds. It is difficult to identify joint sets which are described in other studies from the same are, indicating that local stress is a more important factor than remote stress for controlling joint formation in this area.
- A five-stage model for joint formation is proposed as an interpretation of the observed joint geometries. This model combines thermal-elastic contraction, stress perturbations and structural inheritance as driving mechanisms for joint network formation during uplift and erosion in later stages of basin development.

## 7.2 Further work

This study suggests different venues for further research. One such is to investigate the physical properties controlling length scaling properties of the joint populations. Though length scaling properties of fractures sets has been subject to considerable debate in the scientific community, few studies have analyzed fracture networks with many different joint populations in one outcrop. Results from this project suggests that the outcrops at Lilstock Beach provide a good data source for further investigation of scaling properties of joint sets in structurally complex settings, as well as their spatial distribution and physical controls.

The extent to which numerical modelling is used to reconstruct joint patterns in structurally complex settings is limited. This could, however, be used in order to decipher mechanical and chronological aspects of the formation of fracture patterns observed at Lilstock beach. The high level of exposure and the detailed trace map provides a good means to compare the actual outcrop to the result of a model. Numerical modelling could also be used to calculate and map the potential for percolation in the network at different stages of network development.

Fracture network mapping aided by UAV technology is still in an early phase but could potentially provide near unlimited outcrop data of high quality. This, combined with the use of

machine learning algorithms in fracture digitization, could result in exceedingly detailed and extensive fracture maps. Machine learning algorithms could also be applied to identify joint sets, assessing numerous criteria. This project has been utilizing certain recent technological advances, but the potential for development of analysis methods during the advent of UAV and machine learning technologies is practically unlimited.

# 8. References


Andrews, B. J., Roberts, J. J., Shipton, Z. K., Bigi, S., Tartarello, M. C. & Johnson, G. (2019). How do we see fractures? Quantifying subjective bias in fracture data collection. *Solid Earth*, **10**, 487-516.

Aydin, A. (2000). Fractures, faults, and hydrocarbon entrapment, migration and flow. *Marine and petroleum geology*, **17**, 797-814.

Bai, T. & Pollard, D. D. (2000). Fracture spacing in layered rocks: a new explanation based on the stress transition. *Journal of Structural Geology*, **22,** 43-57.

Bai, T., Maerten, L., Gross, M. R. & Aydin, A. (2002). Orthogonal cross joints: do they imply a regional stress rotation? *Journal of Structural Geology*, **24**, 77-88.

Barton, N., Bandis, S. & Bakhtar, K. (1985). Strength, deformation and conductivity coupling of rock joints. *International journal of rock mechanics and mining sciences & geomechanics abstracts*, **22**, 121-140.

Berkowitz, B. (2002). Characterizing flow and transport in fractured geological media: A review. *Advances in water resources*, ***25***, 861-884.

Bhattacharyya, P. & Czeck, D. M. (2008). Using network analyses within geographic information system technologies to quantify geometries of shear zone networks. *Geosphere*, **4**, 640-656.

Billi, A. & Salvini, F. (2003). Development of systematic joints in response to flexure-related fibre stress in flexed foreland plates: the Apulian forebulge case history, Italy. *Journal of Geodynamics*, **36**, 523-536.

Billi, A., Salvini, F. & Storti, F. (2003). The damage zone-fault core transition in carbonate rocks: implications for fault growth, structure and permeability. *Journal of Structural geology*, **25**, 1779-1794.

Bonnet, E., Bour, O., Odling, N. E., Davy, P., Main, I., Cowie, P. & Berkowitz, B. (2001). Scaling of fracture systems in geological media. *Reviews of geophysics*, **39**, 347-383.

Bons, P. D., Elburg, M. A. & Gomez-Rivas, E. (2012). A review of the formation of tectonic veins and their microstructures. *Journal of Structural Geology*, **43**, 33-62.

Bourne, S. J. & Willemse, E. J. (2001). Elastic stress control on the pattern of tensile fracturing around a small fault network at Nash Point, UK. *Journal of Structural Geology*, **23**, 1753-1770.

Bourne, S. J., Rijkels, L., Stephenson, B. J. & Willemse, E. J. (2001). Predictive modelling of naturally fractured reservoirs using geomechanics and flow simulation. *GeoArabia*, **6**, 27-42.

Brooks, M., Trayner, P. M. & Trimble, T. J. (1988). Mesozoic reactivation of Variscan thrusting in the Bristol Channel area, UK. *Journal of the Geological Society*, **145**, 439-444.

Bucher, W. H. (1921). The mechanical interpretation of joints. *The Journal of Geology*, **29**, 1-28.

Caine, J. S., Evans, J. P. & Forster, C. B. (1996). Fault zone architecture and permeability structure. *Geology*, **24**, 1025-1028.

Caputo, R. (1995). Evolution of orthogonal sets of coeval extension joints. *Terra nova*, **7**, 479-490.

Caputo, R. & Hancock, P. L. (1998). Crack-jump mechanism of microvein formation and its implications for stress cyclicity during extension fracturing. *Journal of Geodynamics*, **27**, 45-60.

Cortés, A. L., Soriano, M. A., Maestro, A. & Casas, A. M. (2003). The role of tectonic inheritance in the development of recent fracture systems, Duero Basin, Spain. *International Journal of Remote Sensing*, **24**, 4325-4345.

Cosgrove, J. W. (2001). Hydraulic fracturing during the formation and deformation of a basin: A factor in the dewatering of low-permeability sediments. *AAPG bulletin*, **85**, 737-748.

Currie, J. B., Patnode, H. W. & Trump, R. P. (1962). Development of folds in sedimentary strata. *Geological Society of America Bulletin*, **73**, 655-673.

Dart, C. J., McClay, K. & Hollings, P. N. (1995). 3D analysis of inverted extensional fault systems, southern Bristol Channel basin, UK. *Geological Society, London, Special Publications*, **88**, 393-413.

Davy, P., Le Goc, R. & Darcel, C. (2013). A model of fracture nucleation, growth and arrest, and consequences for fracture density and scaling. *Journal of Geophysical Research: Solid Earth*, **118**, 1393-1407.

de Joussineau, G., Petit, J. P. & Gauthier, B. D. (2003). Photoelastic and numerical investigation of stress distributions around fault models under biaxial compressive loading conditions. *Tectonophysics*, **363**, 19-43.

DeGraff, J. M. & Aydin, A. (1987). Surface morphology of columnar joints and its significance to mechanics and direction of joint growth. *Geological Society of America Bulletin*, **99**, 605-617.

Dershowitz, W. S. & Einstein, H. H. (1988). Characterizing rock joint geometry with joint system models. *Rock mechanics and rock engineering*, **21**, 21-51.

Duffy, O. B., Nixon, C. W., Bell, R. E., Jackson, C. A. L., Gawthorpe, R. L., Sanderson, D. J. & Whipp, P. S. (2017). The topology of evolving rift fault networks: Single-phase vs multi-phase rifts. *Journal of Structural Geology*, **96**, 192-202.

Dyer, R. (1988). Using joint interactions to estimate paleostress ratios. *Journal of Structural Geology*, **10**, 685-699.

Einstein, H. H. & Baecher, G. B. (1983). Probabilistic and statistical methods in engineering geology. *Rock mechanics and rock engineering*, **16**, 39-72.

Engelder, T. (1985). Loading paths to joint propagation during a tectonic cycle: an example from the Appalachian Plateau, USA. *Journal of Structural Geology*, **7**, 459-476.

Engelder, T. (1987). Joints and shear fractures in rock. In B. K. Atkinson (Red.), *Fracture mechanics of rock* (pp. 27-69). London: Academic press.

Engelder, T. & Geiser, P. (1980). On the use of regional joint sets as trajectories of paleostress fields during the development of the Appalachian Plateau, New York. *Journal of Geophysical Research: Solid Earth*, **85**, 6319-6341.

Engelder, T. & Gross, M. R. (1993). Curving cross joints and the lithospheric stress field in eastern North America. *Geology*, **21**, 817-820.

Engelder, T. & Oertel, G. (1985). Correlation between abnormal pore pressure and tectonic jointing in the Devonian Catskill Delta. *Geology*, **13**, 863-866.

Engelder, T. & Peacock, D. C. (2001). Joint development normal to regional compression during flexural-flow folding: the Lilstock buttress anticline, Somerset, England. *Journal of Structural Geology*, **23**, 259-277.

Faulkner, D. R., Jackson, C. A. L., Lunn, R. J., Schlische, R. W., Shipton, Z. K., Wibberley, C. A. J. & Withjack, M. O. (2010). A review of recent developments concerning the structure, mechanics and fluid flow properties of fault zones. *Journal of Structural Geology*, **32**, 1557-1575.

Faulkner, D. R., Mitchell, T. M., Healy, D. & Heap, M. J. (2006). Slip on 'weak' faults by the rotation of regional stress in the fracture damage zone. *Nature*, **444**, 922-925.

Fischer, M. P. & Wilkerson, M. S. (2000). Predicting the orientation of joints from fold shape: Results of pseudo–three-dimensional modeling and curvature analysis. *Geology*, **28**, 15-18.

Fossen, H. (2010). *Structural geology*. Cambridge: Cambridge University Press.

Gabrielsen, R. H. & Braathen, A. (2014). Models of fracture lineaments – Joint swarms, fracture corridors and faults in crystalline rocks, and their genetic relations. *Tectonophysics*, **628**, 26-44.

Ghosh, K. & Mitra, S. (2009). Structural controls of fracture orientations, intensity, and connectivity, Teton anticline, Sawtooth Range, Montana. *AAPG bulletin*, **93**, 995-1014.

Gillespie, P. A., Howard, C. B., Walsh, J. J. & Watterson, J. (1993). Measurement and characterisation of spatial distributions of fractures. *Tectonophysics*, **226**, 113-141.

Gillespie, P. A., Walsh, J. J., Watterson, J., Bonson, C. G. & Manzocchi, T. (2001). Scaling relationships of joint and vein arrays from The Burren, Co. Clare, Ireland. *Journal of Structural Geology*, **23**, 183-201.

Glen, R. A., Hancock, P. L. & Whittaker, A. (2005). Basin inversion by distributed deformation: the southern margin of the Bristol Channel Basin, England. *Journal of Structural Geology*, **27**, 2113-2134.

Gross, M. R. (1993). The origin and spacing of cross joints: examples from the Monterey Formation, Santa Barbara Coastline, California. *Journal of Structural Geology*, **15**, 737-751.

Gudmundsson, A. & Brenner, S. L. (2001). How hydrofractures become arrested. *Terra Nova*, **13**, 456-462.

Hancock, P. L. (1985). Brittle microtectonics: principles and practice. *Journal of structural geology*, **7**, 437-457.

Helgeson, D. E. & Aydin, A. (1991). Characteristics of joint propagation across layer interfaces in sedimentary rocks. *Journal of Structural Geology*, **13**, 897-911.

Hodgson, R. A. (1961). Classification of structures on joint surfaces. *American journal of science*, **259**, 493-502.

Jing, L. & Stephansson, O. (1997). Network topology and homogenization of fractured rocks. In *Fluid flow and transport in rocks* (pp. 191-202). Dordrecht: Springer.

Kamerling, P. (1979). The geology and hydrocarbon habitat of the Bristol Channel Basin. *Journal of Petroleum Geology*, **2**, 75-93.

Kattenhorn, S. A., Aydin, A. & Pollard, D. D. (2000). Joints at high angles to normal fault strike: an explanation using 3-D numerical models of fault-perturbed stress fields. *Journal of structural Geology*, **22**, 1-23.

Kelly, P. G., Peacock, D. C. P., Sanderson, D. J. & McGurk, A. C. (1999). Selective reverse-reactivation of normal faults, and deformation around reverse-reactivated faults in the Mesozoic of the Somerset coast. *Journal of Structural Geology*, **21**, 493-509.

Kim, Y. S., Peacock, D. C. & Sanderson, D. J. (2004). Fault damage zones. *Journal of structural geology*, **26**, 503-517.

Ladeira, F. L. & Price, N. J. (1981). Relationship between fracture spacing and bed thickness. *Journal of Structural Geology*, **3**, 179-183.

Lamarche, J., Lavenu, A. P., Gauthier, B. D., Guglielmi, Y. & Jayet, O. (2012). Relationships between fracture patterns, geodynamics and mechanical stratigraphy in Carbonates (South-East Basin, France). *Tectonophysics*, **581**, 231-245.

Laubach, S. E., Olson, J. E. & Gross, M. R. (2009). Mechanical and fracture stratigraphy. *AAPG bulletin*, **93**, 1413-1426.

Leckenby, R. J., Sanderson, D. J. & Lonergan, L. (2005). Estimating flow heterogeneity in natural fracture systems. *Journal of Volcanology and Geothermal Research*, ***148***, 116-129.

Loosveld, R. J. H. & Franssen, R. C. M. W. (1992). Extensional vs. Shear Fractures: Implications for Reservoir Characterisation. Society of Petroleum Engineers. doi:10.2118/25017-MS

Maerten, L., Gillespie, P. & Pollard, D. D. (2002). Effects of local stress perturbation on secondary fault development. *Journal of Structural Geology*, **24**, 145-153.

Manzocchi, T. (2002). The connectivity of two-dimensional networks of spatially correlated fractures. *Water Resources Research*, **38**, 1-20.

McGrath, A. G. & Davison, I. (1995). Damage zone geometry around fault tips. *Journal of Structural Geology*, **17**, 1011-1024.

Moore, D. S. & McCabe, G. P. (2005). *Introduction to the Practice of Statistics*. New York: Freeman & Company.

Morley, C. K. & Nixon, C. W. (2016). Topological characteristics of simple and complex normal fault networks. *Journal of Structural Geology*, **84**, 68-84.

Mourzenko, V. V., Thovert, J. F. & Adler, P. M. (1999). Percolation and conductivity of self-affine fractures. *Physical Review E*, **59**, 4265.

Mourzenko, V. V., Thovert, J. F. & Adler, P. M. (2005). Percolation of three-dimensional fracture networks with power-law size distribution. *Physical Review E*, **72**, 036103.

Narr, W. & Suppe, J. (1991). Joint spacing in sedimentary rocks. *Journal of Structural Geology*, **13**, 1037-1048.

Nemčok, M., Gayer, R. & Miliorizos, M. (1995). Structural analysis of the inverted Bristol Channel Basin: implications for the geometry and timing of fracture porosity. *Geological Society, London, Special Publications*, **88**, 355-392.

Nixon, C. W., Sanderson, D. J. & Bull, J. M. (2012). Analysis of a strike-slip fault network using high resolution multibeam bathymetry, offshore NW Devon UK. *Tectonophysics*, ***541***, 69-80.

Nyberg, B., Nixon, C. W. & Sanderson, D. J. (2018). NetworkGT: A GIS tool for geometric and topological analysis of two-dimensional fracture networks. *Geosphere*, **14**, 1618-1634.

Odling, N. E. (1997). Scaling and connectivity of joint systems in sandstones from western Norway. *Journal of Structural Geology*, **19**, 1257-1271.

Odling, N. E., Gillespie, P., Bourgine, B., Castaing, C., Chiles, J. P., Christensen, N. P., E. Fillion, A. Genter, C. Olsen, L. Thrane, R. Trice, E. Aarseth, J. J. Walshand J. Watterson & Trice, R. (1999). Variations in fracture system geometry and their implications for fluid flow in fractures hydrocarbon reservoirs. *Petroleum Geoscience*, **5**, 373-384.

Olson, J., & Pollard, D. D. (1989). Inferring paleostresses from natural fracture patterns: A new method. *Geology*, **17**, 345-348.

Palmer, C. P. (1972). The Lower Lias (Lower Jurassic) between Watchet and Lilstock in North Somerset (United Kingdom). *Newsletters on Stratigraphy*, **2**, 1-30.

Palmström, A. & Singh, R. (2001). The deformation modulus of rock masses – comparisons between in situ tests and indirect estimates. *Tunnelling and Underground Space Technology*, **16**, 115-131.

Peacock, D. C. P. (2001). The temporal relationship between joints and faults. *Journal of Structural Geology*, **23**, 329-341.

Peacock, D. C. P. (2004). Differences between veins and joints using the example of the Jurassic limestones of Somerset. *Geological Society, London, Special Publications*, **231**, 209-221.

Peacock, D. C. P. & Sanderson, D. J. (1992). Effects of layering and anisotropy on fault geometry. *Journal of the Geological Society*, **149**, 793-802.

Peacock, D. C. P., & Sanderson, D. J. (1995). Pull-aparts, shear fractures and pressure solution. *Tectonophysics*, **241**, 1-13.

Peacock, D. C. P. & Sanderson, D. J. (1999). Deformation history and basin-controlling faults in the Mesozoic sedimentary rocks of the Somerset coast. *Proceedings of the Geologists' Association*, **110**, 41-52.

Peacock, D. C. P. & Sanderson, D. J. (2018). Structural analyses and fracture network characterisation: Seven pillars of wisdom. *Earth-Science Reviews*, **184**, 13-28.

Peacock, D. C. P., Nixon, C. W., Rotevatn, A., Sanderson, D. J. & Zuluaga, L. F. (2017). Interacting faults. *Journal of Structural Geology*, **97**, 1-22.

Peacock, D. C. P., Nixon, C. W., Rotevatn, A., Sanderson, D. J. & Zuluaga, L. F. (2016a). Glossary of fault and other fracture networks. *Journal of Structural Geology*, **92**, 12-29.

Peacock, D. C. P., Sanderson, D. J. & Rotevatn, A. (2018). Relationships between fractures. *Journal of Structural Geology*, **106**, 41-53.

Peacock, D. C. P. & Mann, A. (2005). Controls on fracturing in carbonate rocks. Society of Petroleum Engineers. doi:10.2118/92980-MS

Peacock, D. C., Tavarnelli, E. & Anderson, M. W. (2016b). Interplay between stress permutations and overpressure to cause strike-slip faulting during tectonic inversion. *Terra Nova*, **29**, 61-70.

Pollard, D. D. & Aydin, A. (1988). Progress in understanding jointing over the past century. *Geological Society of America Bulletin*, **100**, 1181-1204.

Procter, A., & Sanderson, D. J. (2018). Spatial and layer-controlled variability in fracture networks. *Journal of Structural Geology*, **108**, 52-65.

Ramsay, J. G. (1962). The geometry and mechanics of formation of "similar" type folds. *The Journal of Geology*, **70**, 309-327.

Rawnsley, K. D., Peacock, D. C. P., Rives, T. & Petit, J. P. (1998). Joints in the Mesozoic sediments around the Bristol Channel Basin. *Journal of Structural Geology*, **20**, 1641-1661.

Rawnsley, K. D., Rives, T., Petti, J. P., Hencher, S. R., & Lumsden, A. C. (1992). Joint development in perturbed stress fields near faults. *Journal of Structural Geology*, **14**, 939-951.

Rives, T., Rawnsley, K. D. & Petit, J. P. (1994). Analogue simulation of natural orthogonal joint set formation in brittle varnish. *Journal of Structural Geology*, **16**, 419-429.

Rives, T., Razack, M., Petit, J. P. & Rawnsley, K. D. (1992). Joint spacing: analogue and numerical simulations. *Journal of Structural Geology*, **14**, 925-937.

Roberts, J. C. (1974). Jointing and minor tectonics of the Vale of Glamorgan between Ogmore-By-Sea and Lavernock Point, South Wales. *Geological Journal*, **9**, 97-114.

Rotevatn, A. & Peacock, D. C. (2018). Strike-slip reactivation of segmented normal faults: Implications for basin structure and fluid flow. *Basin Research*, **30**, 1264-1279.

Rustichelli, A., Agosta, F., Tondi, E. & Spina, V. (2013). Spacing and distribution of bed-perpendicular joints throughout layered, shallow-marine carbonates (Granada Basin, southern Spain). *Tectonophysics*, **582**, 188-204.

Sagy, A. & Reches, Z. E. (2006). Joint intensity in layered rocks: The unsaturated, saturated, supersaturated, and clustered classes. *Israel Journal of Earth Sciences*, **55**, 33-42.

Salvini, R., Mastrorocco, G., Seddaiu, M., Rossi, D. & Vanneschi, C. (2017). The use of an unmanned aerial vehicle for fracture mapping within a marble quarry (Carrara, Italy): photogrammetry and discrete fracture network modelling. *Geomatics, Natural Hazards and Risk*, **8**, 34-52.

Sanderson, D. J. (2016). Field-based structural studies as analogues to sub-surface reservoirs. *Geological Society, London, Special Publications*, **436**, 207-217.

Sanderson, D. J. & Nixon, C. W. (2015). The use of topology in fracture network characterization. *Journal of Structural Geology*, **72**, 55-66.

Sanderson, D. J. & Nixon, C. W. (2018). Topology, connectivity and percolation in fracture networks. *Journal of Structural Geology*, **115**, 167-177.

Sanderson, D. J., Peacock, D. C., Nixon, C. W. & Rotevatn, A. (2018). Graph theory and the analysis of fracture networks. *Journal of Structural Geology.* In press.

Secor, D. T. (1965). Role of fluid pressure in jointing. *American Journal of Science*, **263**, 633-646.

Segall, P. & Pollard, D. D. (1983). Joint formation in granitic rock of the Sierra Nevada. *Geological Society of America Bulletin*, **94**, 563-575.

Simon, J. L., Seron, F. J. & Casas, A. M. (1988). Stress deflection and fracture development in a multidirectional extension regime. Mathematical and experimental approach with field examples. *Annales Tectonicae*, **2**, 21-32.

Sævik, P. N. & Nixon, C. W. (2017). Inclusion of topological measurements into analytic estimates of effective permeability in fractured media. *Water Resources Research*, **53**, 9424-9443.

Tavani, S. & Muñoz, J. A. (2012). Mesozoic rifting in the Basque–Cantabrian Basin (Spain): Inherited faults, transversal structures and stress perturbation. *Terra Nova*, **24**, 70-76.

Taylor, W., Pollard, D. D. & Aydin, A. (1999). Fluid flow in discrete joint sets: Field observations and numerical simulations. *Journal of Geophysical Research: Solid Earth*, **104**, 28983-29006.

Underhill, J. R. & Stoneley, R. (1998). Introduction to the development, evolution and petroleum geology of the Wessex Basin. *Geological Society, London, Special Publications*, **133**, 1-18.

Van Hoorn, B. (1987). The south Celtic Sea/Bristol Channel Basin: origin, deformation and inversion history. *Tectonophysics*, **137**, 309-334.

Watkins, H., Bond, C. E., Healy, D. & Butler, R. W. (2015). Appraisal of fracture sampling methods and a new workflow to characterise heterogeneous fracture networks at outcrop. *Journal of Structural Geology*, **72**, 67-82.

Weinberger, R. (1999). Initiation and growth of cracks during desiccation of stratified muddy sediments. *Journal of Structural Geology*, **21**, 379-386.

Welch, M. J., Souque, C., Davies, R. K. & Knipe, R. J. (2015). Using mechanical models to investigate the controls on fracture geometry and distribution in chalk. *Geological Society, London, Special Publications*, **406**, 281-309.

Wheeler, R. L. & Dixon, J. M. (1980). Intensity of systematic joints: methods and application. *Geology*, **8**, 230-233.

Whitaker, A. E. & Engelder, T. (2005). Characterizing stress fields in the upper crust using joint orientation distributions. *Journal of Structural Geology*, **27**, 1778-1787.

Whittaker, A. & Green., W., 1983. Geology of the Country Around Weston-super-Mare, memoir for 1:50,000 geological sheet 279 new series, with parts of sheet 263 and 295. *Geological Survey of Great Britain*.

Wu, H. & Pollard, D. D. (1995). An experimental study of the relationship between joint spacing and layer thickness. *Journal of Structural Geology*, **17**, 887-905.

Zhang, X. & Sanderson, D. J., 1995. Anisotropic features of geometry and permeability in fractured rock masses. *Engineering Geology*, **40**, 65-75.

Zoback, M. D. & Pollard, D. D. (1978). Hydraulic Fracture Propagation and the interpretation of pressure-time records for in-situ stress determinations. American Rock Mechanics Association.

# Appendix I – Stratigraphic logs

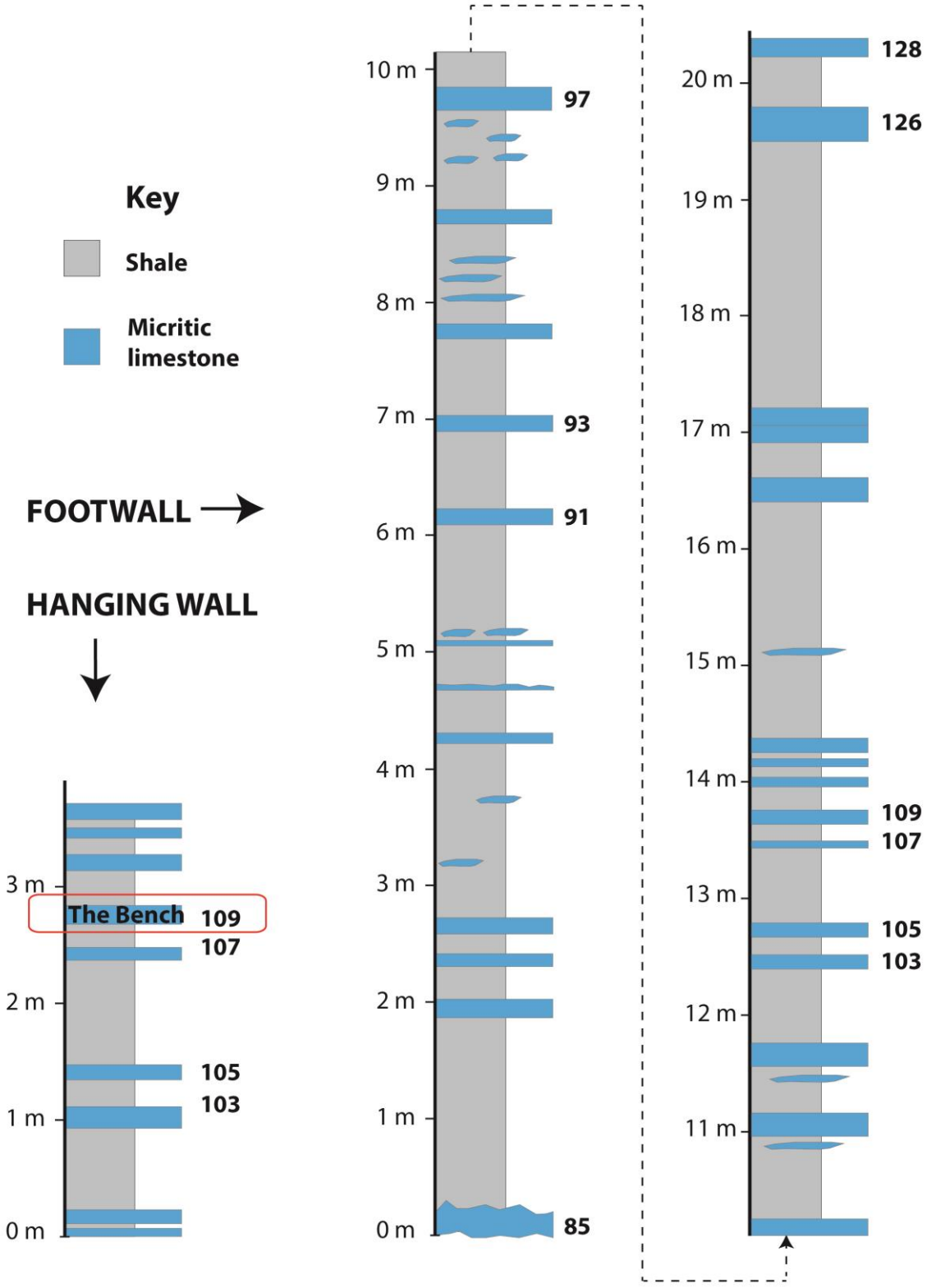


**Figure AI.1**: Simplified stratigraphic log of the hanging wall and footwall. The numbers refer to Whittaker & Green (1983).

# Appendix II – Node counting tables

**Table AII.1**: Node counting table from circle area I.

| | FAN | A1 | A2 | A3 | B1 | B2 | B3 | C1 | C2 | C3 | C4 |
|---|---|---|---|---|---|---|---|---|---|---|---|
| **FAN** | | 5 | 0 | 2 | 1 | 0 | 0 | 0 | 0 | 1 | 1 |
| **A1** | 17 | | 0 | 0 | 0 | 1 | 0 | 0 | 0 | 0 | 0 |
| **A2** | 27 | 0 | | 0 | 0 | 0 | 1 | 0 | 0 | 0 | 0 |
| **A3** | 2 | 2 | 0 | | 0 | 0 | 0 | 0 | 0 | 0 | 0 |
| **B1** | 4 | 0 | 0 | 0 | | 1 | 0 | 0 | 0 | 2 | 0 |
| **B2** | 0 | 1 | 4 | 1 | 0 | | 0 | 0 | 0 | 1 | 0 |
| **B3** | 5 | 1 | 3 | 0 | 7 | 1 | | 0 | 0 | 1 | 2 |
| **C1** | 16 | 3 | 3 | 0 | 0 | 0 | 2 | | 2 | 4 | 0 |
| **C2** | 10 | 32 | 10 | 1 | 20 | 1 | 4 | 5 | | 7 | 29 |
| **C3** | 194 | 8 | 1 | 10 | 7 | 3 | 5 | 14 | 4 | | 5 |
| **C4** | 397 | 0 | 0 | 3 | 0 | 6 | 12 | 1 | 15 | 4 | |

**Table AII.2**: Node counting table from circle area II.

| | FAN | A1 | A2 | A3 | B1 | B2 | B3 | C1 | C2 | C3 | C4 |
|---|---|---|---|---|---|---|---|---|---|---|---|
| **FAN** | | 8 | 0 | 3 | 3 | 0 | 1 | 4 | 1 | 1 | 1 |
| **A1** | 13 | | 0 | 3 | 0 | 5 | 2 | 1 | 0 | 3 | 0 |
| **A2** | 10 | 0 | | 6 | 0 | 4 | 1 | 4 | 0 | 0 | 0 |
| **A3** | 9 | 6 | 0 | | 0 | 0 | 0 | 0 | 0 | 1 | 0 |
| **B1** | 52 | 2 | 0 | 21 | | 17 | 5 | 4 | 3 | 1 | 0 |
| **B2** | 25 | 14 | 4 | 5 | 22 | | 1 | 4 | 2 | 2 | 1 |
| **B3** | 4 | 14 | 0 | 20 | 8 | 3 | | 4 | 0 | 0 | 1 |
| **C1** | 122 | 26 | 10 | 4 | 26 | 6 | 44 | | 11 | 22 | 4 |
| **C2** | 12 | 161 | 15 | 4 | 125 | 13 | 7 | 33 | | 11 | 20 |
| **C3** | 22 | 23 | 2 | 57 | 49 | 98 | 3 | 79 | 18 | | 15 |
| **C4** | 110 | 26 | 0 | 27 | 0 | 46 | 29 | 11 | 67 | 11 | |

**Table AII.3**: Node counting table from circle area III.

| | FAN | A1 | A2 | A3 | B1 | B2 | B3 | C1 | C2 | C3 | C4 |
|---|---|---|---|---|---|---|---|---|---|---|---|
| **FAN** | | 1 | 1 | 0 | 0 | 0 | 0 | 0 | 0 | 0 | 0 |
| **A1** | 7 | | 0 | 3 | 0 | 3 | 1 | 0 | 2 | 1 | 0 |
| **A2** | 10 | 7 | | 3 | 0 | 1 | 0 | 0 | 0 | 1 | 0 |
| **A3** | 4 | 7 | 13 | | 0 | 2 | 1 | 0 | 0 | 0 | 0 |
| **B1** | 4 | 3 | 1 | 6 | | 4 | 0 | 5 | 2 | 2 | 0 |
| **B2** | 5 | 47 | 59 | 5 | 20 | | 1 | 5 | 1 | 0 | 1 |
| **B3** | 1 | 6 | 3 | 5 | 1 | 2 | | 1 | 0 | 0 | 0 |
| **C1** | 59 | 102 | 175 | 74 | 37 | 128 | 66 | | 99 | 208 | 4 |
| **C2** | 2 | 92 | 78 | 7 | 43 | 18 | 6 | 97 | | 24 | 7 |
| **C3** | 40 | 49 | 27 | 161 | 20 | 176 | 8 | 680 | 31 | | 5 |
| **C4** | 7 | 0 | 3 | 15 | 0 | 16 | 7 | 14 | 17 | 20 | |

**Table AII.4**: Node counting table from circle area IV.

| | FAN | A1 | A2 | A3 | B1 | B2 | B3 | C1 | C2 | C3 | C4 |
|---|---|---|---|---|---|---|---|---|---|---|---|
| **FAN** | | 0 | 0 | 1 | 2 | 0 | 1 | 0 | 0 | 0 | 0 |
| **A1** | 0 | | 0 | 0 | 4 | 1 | 0 | 1 | 0 | 0 | 0 |
| **A2** | 1 | 1 | | 3 | 3 | 9 | 5 | 7 | 4 | 1 | 0 |
| **A3** | 0 | 0 | 1 | | 4 | 0 | 4 | 2 | 0 | 1 | 1 |
| **B1** | 1 | 1 | 1 | 16 | | 32 | 46 | 13 | 16 | 6 | 0 |
| **B2** | 0 | 4 | 13 | 2 | 37 | | 16 | 11 | 5 | 5 | 3 |
| **B3** | 5 | 3 | 2 | 2 | 16 | 12 | | 17 | 0 | 0 | 0 |
| **C1** | 2 | 10 | 27 | 5 | 56 | 29 | 82 | | 56 | 56 | 10 |
| **C2** | 8 | 30 | 54 | 21 | 252 | 21 | 22 | 128 | | 38 | 28 |
| **C3** | 17 | 13 | 13 | 49 | 93 | 173 | 16 | 176 | 64 | | 12 |
| **C4** | 6 | 2 | 5 | 14 | 2 | 57 | 49 | 27 | 83 | 31 | |

# Appendix III – Classification tables of nodes and branches

**Table AIII.1:** Absolute values (#) and proportions (%) of node and branch types at different stages of network development in circle area I.

| | I-nodes | | Y-nodes | | X-nodes | | II-branches | | IC-branches | | CC-branches | |
|---|---|---|---|---|---|---|---|---|---|---|---|---|
| | # | % | # | % | # | % | # | % | # | % | # | % |
| **FAN** | 10 | 26 | 24 | 63 | 4 | 11 | 0 | 0 | 4 | 21 | 15 | 79 |
| **A1** | 6 | 4 | 45 | 27 | 114 | 69 | 0 | 0 | 4 | 2 | 255 | 98 |
| **A2** | 7 | 4 | 71 | 36 | 118 | 60 | 0 | 0 | 5 | 2 | 301 | 98 |
| **A3** | 6 | 3 | 76 | 38 | 119 | 59 | 0 | 0 | 5 | 2 | 310 | 98 |
| **B1** | 8 | 3 | 125 | 40 | 178 | 57 | 0 | 0 | 7 | 1 | 495 | 99 |
| **B2** | 6 | 2 | 136 | 43 | 178 | 56 | 0 | 0 | 5 | 1 | 512 | 99 |
| **B3** | 8 | 2 | 155 | 45 | 180 | 52 | 1 | 0 | 5 | 1 | 543 | 99 |
| **C1** | 13 | 3 | 178 | 47 | 188 | 50 | 1 | 0 | 10 | 2 | 590 | 98 |
| **C2** | 50 | 10 | 264 | 53 | 188 | 37 | 10 | 1 | 26 | 3 | 710 | 95 |
| **C3** | 38 | 4 | 709 | 76 | 189 | 20 | 6 | 0 | 24 | 2 | 1 370 | 98 |
| **C4** | 0 | 0 | 1 457 | 88 | 207 | 12 | 0 | 0 | 0 | 0 | 2 531 | 100 |

**Table AIII.2:** Absolute values (#) and proportions (%) of node and branch types at different stages of network development in circle area II.

| | I-nodes | | Y-nodes | | X-nodes | | II-branches | | IC-branches | | CC-branches | |
|---|---|---|---|---|---|---|---|---|---|---|---|---|
| | # | % | # | % | # | % | # | % | # | % | # | % |
| **FAN** | 26 | 81 | 6 | 19 | 0 | 0 | 3 | 25 | 6 | 50 | 3 | 25 |
| **A1** | 32 | 21 | 34 | 23 | 83 | 56 | 0 | 0 | 26 | 12 | 189 | 88 |
| **A2** | 48 | 27 | 44 | 25 | 85 | 48 | 5 | 2 | 30 | 13 | 204 | 85 |
| **A3** | 37 | 19 | 69 | 35 | 93 | 47 | 2 | 1 | 29 | 10 | 254 | 89 |
| **B1** | 68 | 19 | 153 | 44 | 129 | 37 | 5 | 1 | 55 | 11 | 433 | 88 |
| **B2** | 54 | 13 | 239 | 56 | 136 | 32 | 0 | 0 | 49 | 8 | 573 | 92 |
| **B3** | 49 | 10 | 288 | 60 | 142 | 30 | 0 | 0 | 44 | 6 | 658 | 94 |
| **C1** | 76 | 10 | 547 | 71 | 150 | 19 | 7 | 1 | 58 | 5 | 1 045 | 94 |
| **C2** | 94 | 7 | 1 060 | 81 | 153 | 12 | 6 | 0 | 79 | 4 | 1 799 | 95 |
| **C3** | 60 | 3 | 1 538 | 88 | 155 | 9 | 6 | 0 | 47 | 2 | 2 525 | 98 |
| **C4** | 3 | 0 | 2 014 | 93 | 156 | 7 | 0 | 0 | 3 | 0 | 3 255 | 100 |

**Table AIII.3:** Absolute values (#) and proportions (%) of node and branch types at different stages of network development in circle area III.

| | I-nodes | | Y-nodes | | X-nodes | | II-branches | | IC-branches | | CC-branches | |
|---|---|---|---|---|---|---|---|---|---|---|---|---|
| | # | % | # | % | # | % | # | % | # | % | # | % |
| **FAN** | 2 | 100 | 0 | 0 | 0 | 0 | 0 | | 0 | | 0 | |
| **A1** | 13 | 54 | 8 | 33 | 3 | 13 | 1 | 6 | 8 | 44 | 9 | 50 |
| **A2** | 18 | 38 | 26 | 55 | 3 | 6 | 0 | 0 | 12 | 28 | 31 | 72 |
| **A3** | 17 | 20 | 60 | 71 | 8 | 9 | 0 | 0 | 14 | 14 | 83 | 86 |
| **B1** | 35 | 29 | 75 | 63 | 9 | 8 | 3 | 2 | 24 | 19 | 100 | 79 |
| **B2** | 34 | 15 | 179 | 80 | 10 | 4 | 1 | 0 | 29 | 10 | 252 | 89 |
| **B3** | 29 | 12 | 203 | 84 | 11 | 5 | 1 | 0 | 25 | 8 | 289 | 92 |
| **C1** | 469 | 33 | 935 | 66 | 13 | 1 | 102 | 6 | 230 | 14 | 1 260 | 79 |
| **C2** | 385 | 21 | 1 472 | 79 | 14 | 1 | 51 | 2 | 257 | 11 | 2 029 | 87 |
| **C3** | 31 | 1 | 3 494 | 99 | 19 | 1 | 1 | 0 | 29 | 1 | 5 166 | 99 |
| **C4** | 7 | 0 | 3 630 | 99 | 19 | 1 | 0 | 0 | 7 | 0 | 5 382 | 100 |

**Table AIII.4:** Absolute values (#) and proportions (%) of node and branch types at different stages of network development in circle area IV.

| | I-nodes | | Y-nodes | | X-nodes | | II-branches | | IC-branches | | CC-branches | |
|---|---|---|---|---|---|---|---|---|---|---|---|---|
| | # | % | # | % | # | % | # | % | # | % | # | % |
| **FAN** | 7 | 100 | 0 | 0 | 0 | 0 | 1 | 100 | 0 | 0 | 0 | 0 |
| **A1** | 14 | 100 | 0 | 0 | 0 | 0 | 3 | 100 | 0 | 0 | 0 | 0 |
| **A2** | 61 | 97 | 2 | 3 | 0 | 0 | 22 | 81 | 5 | 19 | 0 | 0 |
| **A3** | 74 | 91 | 7 | 9 | 0 | 0 | 24 | 60 | 14 | 35 | 2 | 5 |
| **B1** | 223 | 82 | 49 | 18 | 1 | 0 | 63 | 39 | 62 | 38 | 38 | 23 |
| **B2** | 212 | 54 | 170 | 44 | 8 | 2 | 27 | 8 | 137 | 40 | 180 | 52 |
| **B3** | 167 | 35 | 296 | 62 | 14 | 3 | 10 | 2 | 139 | 27 | 364 | 71 |
| **C1** | 209 | 25 | 600 | 73 | 16 | 2 | 25 | 3 | 148 | 15 | 791 | 82 |
| **C2** | 193 | 12 | 1 414 | 87 | 20 | 1 | 16 | 1 | 155 | 7 | 1 987 | 92 |
| **C3** | 63 | 3 | 2 268 | 96 | 21 | 1 | 0 | 0 | 62 | 2 | 3 323 | 98 |
| **C4** | 3 | 0 | 2 645 | 99 | 22 | 1 | 0 | 0 | 3 | 0 | 3 935 | 100 |